VNIVERSITAT DE VALÈNCIA

DEPARTAMENT DE FÍSICA APLICADA I ELECTROMAGNETISME

PROGRAMA DE DOCTORADO EN FÍSICA

VECTOR FWM IN OPTICAL FIBERS: TUNING TECHNIQUES AND APPLICATIONS

DOCTORAL THESIS

ABRAHAM DE JESÚS LOREDO TREJO

Valencia, March 2022

SUPERVISOR:

ANTONIO DÍEZ CREMADES

Dr. Antonio DÍEZ CREMADES, Catedrático del Departamento de Física Aplicada y Electromagnetismo de la Universidad de Valencia.

CERTIFICA que la presente memoria "*Vector FWM in optical fibers: tuning techniques and applications*" resume el trabajo de investigación realizado, bajo su dirección en el departamento de Física Aplicada y Electromagnetismo de la Universitat de València, por D. Abraham de Jesús LOREDO TREJO y constituye su tesis para optar al título de Doctor por la Universitat de València una vez cursados los estudios en el Doctorado en Física. Y para que conste, y en cumplimiento de la legislación vigente, firma el presente certificado en Valencia, a

Fdo. Dr. Antonio Díez Cremades

Abstract

Recently, the nonlinear four-wave mixing (FWM) effect in optical fibers has attracted great interest for the development of new optical fiber light sources due to the multiple light emission produced by this nonlinear effect. In recent years, such FWM-based light sources have demonstrated great utility in areas such as quantum optics and advanced Raman-based microscopy. Additionally, according to the polarization state of the pump light responsible for the FWM effect and the birefringence of the fiber, the light produced by FWM can exhibit different polarization properties given the vector nature of the FWM. Thus, this enables the design and development of polarized light sources with multiple emission which can be of great interest in different studies or applications of photonics. In addition, FWM effect is relatively sensitive to changes in the optical properties of the medium in which it is generated. In the case of an optical fiber, the chromatic dispersion and birefringence of the fiber are the most relevant parameters in the phase-matching condition of FWM. In such a way, certain physical quantities can be measured by means of FWM-based fiber optic sensors taking advantage of the susceptibility of the fiber to changes in the optical properties of the fiber itself. In this thesis we provide the theoretical and experimental study of vector FWM produced in weakly birefringent optical fibers. In particular, we have focused our attention on a specific process of vector FWM known as polarization modulation instability (PMI). In this work we provide simple and practical methods to generate and tune the emission of intense bands of light produced by PMI/FWM over a wide wavelength range.

Given the high efficiency of microstructured optical fibers (MOFs) to generate nonlinear effects such as FWM, most of our experiments were carried out with MOFs with different guiding properties. In this work, we show the generation of

PMI/FWM in fibers with ANDi dispersion profiles, fibers with 1 or 2 zero-dispersion wavelength, and hybrid MOFs infiltrated with optical liquids whose properties enables PMI/FWM generation and tuning.

In this thesis we have demonstrated broadband tuning of intense light bands produced by PMI. Tunability is achieved by exploiting the sensitivity of the PMI phase-matching condition to changes of dispersion and birefringence of the optical fiber. To this end, simple techniques have been employed to control fiber dispersion and birefringence based on either the elasto-optic effect of fused silica or the thermo-optic effect of the liquids infiltrated into the fibers. In addition, simultaneous generation and tuning of FWM and PMI in MOFs has been demonstrated for the first time. This required a fine control of the optical guiding properties of the fibers. In this study we have experimentally demonstrated tunability of the light bands generated by both effects over a wide wavelength range, covering a large part of the near-infrared spectrum. Finally, we show the feasibility of developing fiber optic sensors based on the sensitivity of the spectral response of the PMI/FWM bands to changes in the refractive index of the holes or birefringence of the optical fiber. As an example, a method for the characterization of the thermo-optic properties of water-based liquids is proposed.

Acknowledgments

I would like to thank all those who have contributed to this thesis project. In particular, I would like to thank Dr. Antonio Diez, who has supervised every step of this work. I would like to thank him for the time and dedication he has put into this work and even more for his patience. I consider him a great professor and an excellent researcher. I am glad to have worked with him. I would also like to thank Dr. Miguel Andres for giving me the opportunity to work in this research group and for all the advice he has given me to improve this work. In addition, I would like to thank him for all the support he has offered me since my arrival in Valencia. I also thank Miguel Bello for encouraging me to pursue my doctoral studies abroad. I would also like to thank Dr. José Luis Cruz, Dr. Enrique Silvestre and Dr. Martina Delgado for their help and good advice. I am also grateful to the administrative and service staff of the department of applied physics of the Universtat de Valencia.

Throughout this thesis, I have had the pleasure of meeting and working with many people, Antonio Carrascosa, Xavi, Josu, Beto, Carolina, Luis, Pablo, Tomás, Dani, Manuel, Diego and all those people I have not named but who have been part of it, thank you for making this journey even more fun, rewarding and less stressful. I especially want to thank Martina, Emmanuel, Saúl and Akun for all the good times we had, from having a good tortilla de patatas or a spicy hotpot, running through the mountain (por caminos de cabras), and even better, being on a terrace talking and laughing.

I am grateful to the Generalitat Valenciana and the Santiago Grisolía program for the predoctoral contract CPI-17-197, which has allowed me to carry out this work. I would also like to thank the Ministerio de Ciencia e Innovación and the Fondo Europeo de Desarrollo Regional for funding the projects PID2019-

104276RB-I00 and TEC2016-76664-C2-1-R of which I have been part during my PhD studies.

Por último, me gustaría dar las gracias a todas aquellas personas que no están directamente relacionadas con este trabajo de tesis, pero que, a lo largo de este, han estado ahí brindándome su apoyo cuando lo he necesitado. A mi familia por darme su apoyo incondicional y alentarme a conseguir mis objetivos. A mis amigos y amigas que los considero también parte de mi familia, gracias por estar siempre ahí, para animarme y apoyarme todos estos años. Por último, me gustaría dar las gracias a María por sus sabios consejos, ayuda y paciencia que me ha brindado en estos últimos años.

Contents

Resumen en español

Motivación y objetivos

Las fuentes de luz basadas en la óptica no lineal son de gran interés tanto en aplicaciones de fotónica, así como en diferentes áreas de investigación. Estas fuentes de luz presentan propiedades espectrales y temporales tales que resultan adecuadas para su explotación en diferentes ámbitos, desde investigación básica hasta aplicaciones relacionadas con la biomedicina, la óptica cuántica, la teledetección, las telecomunicaciones y el análisis de materiales, entre otras.

Los efectos ópticos no lineales surgen como resultado de la respuesta del medio material cuando se somete a un campo electromagnético intenso. Como resultado de la interacción no lineal luz-materia, se pueden producir efectos tales como el autoenfoque (o desenfoque) de un haz de luz, la mezcla de ondas a diferentes frecuencias, la modulación de las propiedades ópticas del material (índice de refracción o coeficiente de absorción), la generación de nuevas frecuencias, el ensanchamiento espectral de un pulso óptico estrecho, por mencionar algunos. Entre estos, los efectos relacionados con la mezcla o la generación de nuevas frecuencias son los efectos no lineales más relevantes para el desarrollo de fuentes de luz. En aplicaciones de fotónica, existen materiales cuya respuesta no lineal es más eficiente, dichos materiales se conocen como materiales no lineales.

La tecnología de la fibra óptica permite el desarrollo de fuentes de luz con todas las ventajas de una fibra óptica. Aunque el SiO_2 con el que están fabricadas la mayoría de fibras ópticas no es un material que presente un comportamiento no lineal muy eficiente, esto se ve ampliamente compensado por dos aspectos: (1) el tamaño de haz en una fibra óptica puede ser muy pequeño, del orden de pocas decenas de μm^2,

lo que puede dar lugar a valores de densidad energía muy altas, y (2) en una fibra óptica la longitud de interacción puede ser muy larga (de centenares de metros). Por otro lado, el desarrollo en las últimas décadas de las fibras ópticas microestructuradas, (por sus siglas en inglés, MOFs), también conocidas como fibras de cristal fotónico (por sus siglas en inglés, PCF), ha contribuido a ampliar las posibilidades de las fibras ópticas en el campo de la óptica no lineal. En concreto, las MOFs se pueden diseñar de tal manera que el área modal sea incluso menor que en las fibras convencionales, a la vez que es posible controlar de manera muy flexible la dispersión cromática, lo que resulta fundamental para controlar el tipo de efectos no lineales que se van a generar y su eficiencia. Por ello, consideramos que las MOFs son una plataforma adecuada para desarrollar aplicaciones basadas en interacciones ópticas no lineales.

La mezcla de cuatro ondas (por sus siglas en inglés, FWM) es un efecto no-lineal que puede producirse en una fibra óptica y que es capaz de generar fotones a una frecuencia diferente de la frecuencia de la onda de excitación. La luz generada por FWM permite diseñar fuentes de luz con múltiples bandas espectrales de emisión, relativamente estrechas. La FWM es un efecto no lineal de tipo elástico, en el que, a diferencia de los efectos no lineales inelásticos, la energía de los fotones del haz (o haces) incidente (haz de bombeo) se transfiere a dos nuevos fotones de diferente frecuencia, sin que se produzca transferencia de energía al medio en el que se propaga la onda, en nuestro caso la fibra óptica. La FWM es un efecto no lineal de tipo paramétrico, y como tal requiere del cumplimiento de una condición de ajuste de fase para que se produzca de forma eficiente. El cumplimiento de la condición de ajuste de fase está determinado fundamentalmente por las características de la señal óptica de bombeo y por las propiedades de guiado de la fibra óptica. Concretamente, depende en gran medida de la dispersión cromática de la fibra y de la respuesta no lineal. En determinados casos, también depende de la birrefringencia de la fibra y de la polarización del haz de bombeo. De hecho, la condición de ajuste

de fase se produce cuando las diferentes contribuciones a la fase de la onda se equilibran en las frecuencias de los fotones generados por FWM y de los fotones de excitación. Idealmente, cuando se produce la condición de ajuste de fase, la señal óptica de bombeo se transfiere a dos bandas espectrales, denominadas comúnmente bandas *signal* e *idler*, la primera formada por fotones de mayor energía que el bombeo y la segunda por fotones de menor energía a los fotones del bombeo. Dependiendo de las propiedades de guiado de la fibra, las bandas *signal* e *idler* pueden generarse en diferentes regiones del espectro óptico. Cabe destacar que, dependiendo del estado de polarización de la luz de bombeo, las bandas de FWM pueden mostrar diferentes propiedades, lo que evidencia la naturaleza vectorial de este efecto.

En este trabajo, prestamos especial atención a un caso particular de FWM vectorial conocido como modulación por inestabilidad debido a la polarización (por sus siglas en inglés, PMI). Este caso particular de FWM se puede producir en fibras débilmente birrefringentes. En un marco de referencia de luz linealmente polarizada, las dos bandas generadas por PMI están co-polarizadas, pero su polarización es perpendicular a la polarización de la luz de bombeo. Este caso vectorial de FWM puede producirse efectivamente cuando la luz de bombeo excita uno de los modos propios de polarización de la fibra óptica cuyo campo eléctrico está polarizado a lo largo de un eje principal de la fibra (rápido o lento), y por tanto las bandas de PMI generadas están polarizadas a lo largo del eje ortogonal (lento o rápido).

Las características de la luz generada mediante FWM/PMI permiten diseñar fuentes de luz con una serie de propiedades que resultan interesantes en ciertas aplicaciones, entre las que podemos destacar las técnicas de microscopía avanzada basadas en CARS y SRS, y la fotónica cuántica. En lo que se refiere a la primera aplicación, FWM/PMI proporciona dos (o más) bandas de luz estrechas con una separación espectral controlada, sincronizadas y de intensidad suficiente, lo que se ajusta con las especificaciones que estas técnicas de microscopía requieren a la fuente

de luz con las que se iluminan las muestras. Por otro lado, las propiedades cuánticas de los pares de fotones que se generan mediante este efecto no lineal, también son de interés para el desarrollo de fuentes de luz de pares de fotones para aplicaciones de criptografía cuántica.

Cabe destacar también el interés en los aspectos más fundamentales de este proceso no lineal, en particular del PMI, ya que puede estar presente en diferentes configuraciones no lineales. Por ejemplo, PMI está en el origen de la degradación de la coherencia de la luz emitida en fuentes de supercontinuo coherentes basadas en fibras ópticas con dispersión normal. Por otro lado, PMI también puede darse en procesos de generación de peines de frecuencia en microrresonadores ópticos.

El objetivo central de este trabajo es aportar conocimientos y un conjunto de técnicas que ayuden al desarrollo de fuentes de luz de fibra óptica basadas en el efecto no lineal de FWM vectorial. Por un lado, planteamos realizar un estudio detallado del fenómeno de la generación de PMI y FWM en MOFs con diferentes propiedades de dispersión. Por otro lado, nos proponemos desarrollar técnicas prácticas de sintonización para controlar la posición espectral de las bandas generadas mediante FWM y PMI en un amplio rango espectral. Este aspecto es muy importante ya que añade versatilidad a las fuentes de luz que se puedan desarrollar en base a FWM/PMI y amplía sus capacidades prácticas.

Cabe comentar que, aunque el carácter de esta tesis es fundamentalmente experimental, no deja de lado los aspectos teóricos y de modelización necesarios para comprender y predecir este efecto no lineal en las fibras ópticas.

Fundamentos teóricos de FWM vectorial

El efecto de FWM se considera un efecto no lineal paramétrico, que está relacionado con la modulación del índice de refracción del medio causado por la presencia de un campo electromagnético intenso, lo que se conoce como efecto Kerr. Desde el punto de vista físico, el FWM surge de la respuesta no lineal de los electrones ligados de un material en presencia de un campo electromagnético intenso. En general, la polarización inducida en un medio dieléctrico (en nuestro caso la fibra óptica) por el campo electromagnético contiene términos que no dependen linealmente con el campo eléctrico, cuya magnitud se rige por los elementos de susceptibilidad eléctrica del material de órdenes mayor que uno. En fibras ópticas basadas en SiO_2, los efectos no lineales de segundo orden son despreciables debido a la estructura centro-simétrica de la molécula, de manera que los efectos no lineales de orden más bajo que se pueden producir en este material se deben a los elementos del tensor susceptibilidad de tercer orden. Los procesos paramétricos de tercer orden implican la interacción no lineal entre cuatro ondas ópticas e incluyen fenómenos como FWM y la generación de terceros armónicos.

En esta tesis, se aborda la descripción teórica de FWM en fibras ópticas. Para ello, hemos seguido la descripción clásica de la propagación no lineal de un campo electromagnético dentro de una fibra óptica. En esta descripción hemos considerado una fuente de luz de bombeo en el régimen de onda continua (por sus siglas en inglés, CW) dado que en nuestros experimentos se utilizó una fuente de luz pulsada con una duración de pulso de unos cientos de ps. Aunque ciertamente no se trata de un régimen de CW, se considera como un régimen de cuasi-CW ya que la duración del pulso es varios órdenes de magnitud mayor que la respuesta temporal de los efectos no lineales investigados (del orden de ~fs). Por ello, la formulación derivada para describir el efecto de FWM bajo bombeo CW es adecuada para el régimen de bombeo cuasi-CW.

En primer lugar, a partir de las ecuaciones de Maxwell y considerando una fibra óptica (medio dieléctrico, no magnético y sin cargas ni corrientes libres) como el medio en que se propagan las ondas, se han derivado las ecuaciones de propagación de las cuatro ondas electromagnéticas involucradas en un proceso de FWM con polarizaciones arbitrarias. Bajo este tratamiento se ha considerado la contribución lineal y no lineal de la polarización eléctrica inducida. En esta última, el término no lineal de la polarización se evalúa en función del campo eléctrico y de la susceptibilidad de tercer orden de la sílice. Las ecuaciones de propagación de las cuatro ondas involucradas en un proceso de FWM pueden ser evaluadas asumiendo que los vectores de campo eléctrico se encuentran en el plano transversal respecto a la dirección de propagación de los campos. Dicha suposición es aplicable a los modos de la fibra óptica, dado que la amplitud de las componentes de los campos axiales es generalmente mucho menor que las componentes de los campos en el plano transversal. Como resultado, se obtienen un conjunto de cuatro ecuaciones diferenciales acopladas, las cuales describen la evolución de las amplitudes de los campos involucrados en un proceso de FWM con polarizaciones arbitrarias. Estas ecuaciones diferenciales representan el caso más general de FWM vectorial que puede ocurrir en una fibra óptica débilmente birrefringente.

De acuerdo con cada proceso de FWM vectorial, existen una serie condiciones que dictaminan las frecuencias y la eficacia con la que este proceso puede producirse en una fibra óptica. Se trata de la conservación de energía y de la conservación del momento de los fotones involucrados en un proceso de FWM. La conservación de energía dictamina las frecuencias de los fotones de FWM en función de la frecuencia de los fotones de bombeo. Por otra parte, la conservación del momento relaciona cuan eficiente puede ser un proceso de FWM por medio de la condición de ajuste de fase. Esta última se deriva a partir de las ecuaciones que describen la evolución de los campos a las frecuencias de los fotones *signal* e *idler*. La condición de ajuste de fase involucra la birrefringencia de la fibra y sus propiedades dispersivas por medio

de los factores de propagación del modo guiado a las frecuencias de la luz bombeo y la frecuencia de los nuevos fotones generados (contribución de fase lineal). A su vez, la condición de ajuste fase involucra la contribución no lineal de la fibra óptica por medio del parámetro no lineal de la misma (contribución de fase no lineal). En particular, el efecto de FWM se vuelve eficiente cuando ambas contribuciones lineal y no lineal están en equilibrio, y una compensa a la otra.

De acuerdo con los objetivos enmarcados para esta tesis, hemos descrito teóricamente el efecto de FWM en fibras ópticas débilmente birrefringentes teniendo en cuenta el carácter vectorial del FWM. En ambos casos se han derivado las ecuaciones que describen la condición de ajuste de fase y ganancia paramétrica. En particular, hemos centrado la descripción vectorial de FWM considerando luz de bombeo linealmente polarizada y prestando especial atención a los procesos vectoriales producidos cuando la luz de bombeo excita uno de los modos de polarización propios de la fibra óptica, cuyo campo eléctrico está polarizado a lo largo del eje rápido (o lento de la fibra). Como resultado, se obtiene que se pueden dar cuatro procesos de FWM. En todos ellos, las bandas espectrales generadas presentan la misma polarización entre ellas. Cuando la polarización del bombeo coincide con el eje rápido de la fibra, se pueden dar dos procesos de FWM. En el primero, las bandas *signal* e *idler* se generan con idéntica polarización a la polarización de la señal de bombeo, mientras que el segundo proceso da lugar a bandas con polarización perpendicular al bombeo, es decir los fotones *signal* e *idler* se generan en el modo lento de la fibra óptica. Por otro lado, cuando la polarización del bombeo está orientada con el eje lento de la fibra, un primer proceso de FWM puede dar lugar a bandas con la misma polarización que los fotones de bombeo, mientras que el segundo proceso puede dar lugar a fotones con polarización ortogonal a la del bombeo, es decir, con la polarización del eje rápido de la fibra.

A los procesos de FWM en el que la polarización de los fotones *signal* e *idler* es ortogonal con respecto a la polarización de los fotones de bombeo se les denomina PMI, y no es más que un proceso de FWM que se puede dar en fibras ópticas birrefringentes. Gran parte del trabajo de esta tesis se basa en dicho efecto no lineal. Por lo cual, los principales aspectos teóricos del efecto de PMI se abordan en el marco teórico de esta tesis.

Por último, en la parte teórica, investigamos numéricamente cómo depende la frecuencia de las bandas generadas por FWM/PMI con los diferentes parámetros de la fibra óptica que intervienen en el proceso. Este estudio tiene como objetivo, proporcionar los conocimientos teóricos en los que se basan la mayoría de los resultados experimentales incluidos en esta tesis. En particular, investigamos el impacto en la condición de ajuste de fase del parámetro no lineal de la fibra, de la birrefringencia y de su dispersión cromática. Todos estos cálculos requieren del conocimiento previo de las propiedades lineales de la fibra óptica en la que se estudia el proceso de FWM. Las propiedades lineales de las MOFs, en concreto, el factor de propagación, el área efectiva y la birrefringencia fueron calculados utilizando un software desarrollado en el LFO denominado *"Itera"*.

Procedimientos experimentales

Gran parte de los experimentos realizados a lo largo de esta tesis fueron realizados con fibras microestructuradas, que fueron diseñadas y fabricadas de acuerdo con cada aplicación o experimento concreto. Las MOFs utilizadas durante los experimentos fueron fabricadas en las instalaciones de la Universidad de Valencia, concretamente en los laboratorios de fabricación de fibra óptica del Laboratorio de Fibra Óptica (LFO). El método que se ha seguido para la fabricación de las MOFs se denomina con el término *stack and draw,* y consiste en realizar una preforma a base de apilar ordenadamente capilares y varillas de sílice, que

posteriormente será fundida y estirada a fibra óptica. El sistema que empleamos para fabricar nuestras MOFs se basa en una torre de estiramiento utilizada habitualmente para la fabricación de fibra óptica convencional, que ha sido modificada convenientemente para cumplir los requisitos específicos de la fabricación de MOFs de sílice. Una vez fabricadas las fibras objetivo, la sección transversal de las mismas se caracteriza mediante microscopía electrónica de barrido (SEM), y se seleccionan aquellas que cumplen con los parámetros de diseño.

A lo largo de este proyecto de investigación se fabricaron un buen número de MOFs para llevar a cabo los experimentos de generación de FWM/PMI. En concreto, se han fabricaron tres familias de MOFs con diferentes propiedades de dispersión: (1) MOFs que exhiben una dispersión totalmente normal en un amplio rango de longitudes de onda (por sus siglas en inglés, fibras ANDi), (2) MOFs con dispersión normal pequeña a la longitud de onda experimental, y (3) MOFs con dispersión anómala.

En muchos de los experimentos de esta tesis, requerimos un ajuste fino de la dispersión cromática de una MOF para controlar la posición espectral de las bandas generadas mediante FWM/PMI. En una MOF, cuyos agujeros están rellenos de aire, la dispersión cromática de la fibra queda fijada por sus parámetros estructurales, y no hay un método sencillo de modificarla a posteriori. Sin embargo, cuando los orificios de las fibras se rellenan con una sustancia con propiedades ópticas adecuadas, se obtiene un grado de libertad adicional para ajustar la dispersión de la fibra en una etapa posterior a la fabricación de las mismas. Así, en algunos experimentos infiltramos líquidos en los agujeros de las MOFs para ajustar eficazmente su dispersión. En concreto, utilizamos agua pesada, etanol y mezclas de etanol y agua.

El montaje experimental que hemos empleado para excitar y caracterizar los efectos no lineales de FWM/PMI producidos en MOFs, consta de un láser que emite

pulsos a una longitud de onda de 1064 nm, con una duración del pulso de 700 ps y una potencia máxima de ~ 11 kW. La emisión del láser es linealmente polarizada. El haz emitido por el láser se utilizó como señal de bombeo. A la salida del láser, el montaje dispone de una lámina de media onda para rotar el plano de polarización del haz de bombeo con respecto a los ejes principales de la fibra bajo prueba. El haz de bombeo se introduce en las fibras por medio de lentes asféricas de diferente distancia focal y una base de alineación micrométrica XYZ en la cual se fija la fibra a caracterizar. La relación de potencia acoplada varía entre el 40 y el 50 % dependiendo de cada fibra y la longitud típica de la fibra utilizada en los experimentos fue de ~1 m.

Para caracterizar el estado de polarización de la luz generada en la fibra óptica por la interacción no lineal, se utilizó un polarizador lineal situado a la salida de la fibra a caracterizar. Por otro lado, empleamos un analizador de espectros óptico para registrar y analizar los espectros de la luz a la salida de la fibra óptica, normalmente con una resolución espectral de 0.2 nm. Por último, se utilizó un medidor de potencia para medir la potencia de la señal de bombeo que se inyecta en la fibra.

Con este arreglo experimental llevamos a cabo los experimentos de generación y sintonización de bandas de FWM/PMI. De acuerdo con las características de cada experimento, las fibras se sometieron a diferentes pruebas físicas (por ejemplo, tensión axial, flexión, calor), por lo que fue necesario añadir los subsistemas necesarios en el montaje experimental de acuerdo a cada caso.

Resultados y conclusiones

En esta tesis nos hemos centrado en el estudio del efecto óptico no lineal de FWM vectorial en fibras ópticas, y en el desarrollo de mecanismos viables para la sintonización de las bandas de FWM generadas. La mayor parte de los experimentos

se han realizado utilizando MOFs, aunque también se incluyen algunos resultados obtenidos con fibras convencionales. El objetivo principal de este trabajo es producir el conocimiento, y un conjunto de técnicas para apoyar el desarrollo de fuentes de luz de fibra óptica versátiles basadas en este efecto no lineal.

Este estudio se ha organizado en dos partes principales. En la primera, presentamos un estudio detallado, tanto teórico como experimental de los efectos no lineales de PMI y FWM que pueden producirse en las fibras ópticas. Este estudio nos ha permitido identificar los parámetros de la fibra que determinan las principales características de los efectos PMI y FWM. La segunda parte se dedicó al desarrollo de métodos sencillos para sintonizar las bandas espectrales generadas mediante PMI y FWM, actuando sobre las propiedades de la fibra, en particular sobre la dispersión cromática y la birrefringencia. El control de estos parámetros de la fibra se logró mediante métodos dinámicos basados en los efectos elasto-óptico y termo-óptico.

En el capítulo 2, hemos proporcionado la descripción teórica del efecto no lineal de FWM en fibras ópticas. Hemos obtenido las ecuaciones para las amplitudes acopladas, el ajuste de fase y la ganancia que describen el efecto FWM para fibras isotrópicas y débilmente birrefringentes teniendo en cuenta la naturaleza vectorial de la luz. Este marco teórico proporcionó una descripción detallada de los efectos de FWM y PMI en la colección de MOFs que se utilizaron para esta tesis. Por lo tanto, pudimos comparar los resultados experimentales con simulaciones teóricas con una concordancia relativamente buena.

En cuanto a la parte experimental de esta tesis, hemos estudiado en detalle el efecto de PMI producido en MOFs con diferentes características de dispersión cromática bajo bombeo cuasi-CW. En particular, hemos caracterizado el PMI generado con un bombeo con polarización orientada con el eje lento de las fibras en una amplia familia de MOFs, incluyendo MOFs rellenas de aire, de etanol y de agua pesada. Las fibras investigadas se diseñaron para que presentaran diferentes perfiles

de dispersión, abarcando fibras de tipo 1-ZDW, 2-ZDW y ANDi. En el caso de las fibras ANDi, hemos demostrado, por primera vez, que la separación en frecuencia entre de las bandas PMI y el bombeo (Ω) es máxima cuando la longitud de onda de bombeo coincide con la longitud de onda en que la curva de dispersión presenta un máximo (MDW). El mayor valor de Ω medido con este tipo de fibras fue 1538 cm^{-1}, obtenido en una fibra con MDW = 1058 nm. Cabe comentar que el FWM/MI escalar no se puede dar en las fibras ANDi, ya que la condición de ajuste de fase para ese proceso de FWM no puede satisfacerse en este tipo de fibras. En su lugar, sólo se puede generar PMI, lo que también se corroboró con nuestros experimentos. Adicionalmente, hemos demostrado que se puede generar bandas de PMI con valores de Ω incluso mayores en fibras con 1 o 2 ZDW cuando la dispersión de la fibra a la longitud de onda de bombeo es normal y baja, lo que puede darse, por ejemplo, cuando la longitud de onda de excitación está en la cercanía de un ZDW.

El conjunto de resultados experimentales incluidos en el capítulo 4 nos permitió señalar la relevancia de la birrefringencia de la fibra en el cumplimiento de la condición de ajuste de fase del PMI. Esto se concluyó tras comparar los resultados obtenidos con fibras con valores de dispersión similares en la longitud de onda de excitación, pero con diferente birrefringencia residual. Una mayor birrefringencia da lugar a bandas más separadas del bombeo, por tanto, a valores mayores de **Ω**.

Una parte importante del trabajo se dedicó a estudiar diferentes métodos para controlar y sintonizar la ubicación espectral de las bandas de PMI y FWM. En el capítulo 5, mostramos diferentes métodos que permitieron sintonizar las bandas de PMI producidas en MOFs y fibras ópticas estándar en un amplio rango de frecuencias. Hemos desarrollado métodos sencillos para controlar la birrefringencia y la dispersión de la fibra, y explotamos esa característica para controlar la posición espectral de las bandas de PMI.

Los métodos empleados para inducir birrefringencia de manera controlada en las fibras ópticas empleados se fundamentan ambos en el efecto elasto-óptico. El primero se basa en introducir una curvatura controlada en la fibra óptica. En el segundo método se utiliza la tensión mecánica aplicada a un arrollamiento de fibra óptica para modificar la birrefringencia. Estos experimentos se realizaron con fibras ópticas estándar de salto de índice que presentan una birrefringencia residual relativamente baja cuando las fibras no están sujetas a deformaciones.

En cuanto al efecto de birrefringencia inducida por flexión pura, se consiguió un rango de desplazamiento de la frecuencia de las bandas de PMI desde $\Omega = 111$ cm^{-1} hasta $\Omega = 779$ cm^{-1} variando la birrefringencia de la fibra desde 4.6×10^{-7} hasta 3.9×10^{-5}. Los resultados obtenidos con la técnica de tensión y arrollamiento fueron más pobres. El rango de sintonización de Ω conseguido en nuestros experimentos está comprendido entre 621 cm^{-1} y 726 cm^{-1} para un rango de tensión de 3.8×10^{-3} a 5.0×10^{-3}. Con los resultados obtenidos por esta técnica pudimos evidenciar que la contribución de las propiedades elásticas del polímero que recubre la fibra óptica actúa como amortiguación de la tensión aplicada a la misma, por ende, se reduce significativamente la birrefringencia inducida por el tensado y enrollado de la fibra. Aprovechando la relación directa entre el desplazamiento de frecuencia de las bandas de PMI y el cambio de birrefringencia en una fibra con un alto valor de dispersión normal a la longitud de onda de la bomba, pudimos estimar la tensión real aplicada en las fibras enrolladas a tensión. En este sentido, nos gustaría resaltar que el efecto PMI en fibra óptica puede ser explotado para la caracterización de las propiedades de la misma. Basándose en este efecto no lineal, se pueden determinar parámetros de la fibra como el coeficiente no lineal, la birrefringencia o la dispersión cromática.

La segunda parte del Capítulo 5 está dedicada a la sintonización de las bandas PMI mediante el control de la birrefringencia y la dispersión de la fibra a través de

los efectos térmicos. Estos trabajos se han realizado con MOFs infiltradas con líquidos con propiedades ópticas y termo-ópticas adecuadas. En concreto, en nuestros experimentos se utilizaron fibras infiltradas con etanol y agua pesada. Estos líquidos presentan valores del coeficiente termo-óptico relativamente grandes, por lo que cambios moderados de temperatura pueden provocar cambios grandes tanto de la dispersión cromática como de la birrefringencia de la fibra. En términos generales podemos afirmar que hemos podido sintonizar las bandas de PMI en un amplio rango de frecuencias con variaciones moderadas de la temperatura. En el mejor resultado obtenido con una MOF con orificios rellenos de etanol, Ω se sintonizó desde 1274 cm^{-1} hasta 2189 cm^{-1} en un rango de temperatura de 20 °C a 60 °C. Con MOFs infiltradas con agua pesada, el rango de sintonización mayor que se obtuvo está comprendido entre 1084 cm^{-1} y 2786 cm^{-1}, para un rango de temperatura de 20 °C a 90 °C, siendo este último experimento con el que se obtuvo el mayor rango de sintonización de las bandas del PMI de todos los experimentos realizados.

El rango de sintonía de las bandas PMI conseguido con esta técnica casi cubre las frecuencias vibracionales (de 1000 cm^{-1} a 3700 cm^{-1}) de la mayoría de los grupos funcionales representativos para la bio-imagen de moléculas empleadas en la microscopía avanzada basada en efecto Raman. Además, nos gustaría destacar que las bandas de PMI producidas en las MOFs infiltradas con líquidos fueron capaces de excitar por sí mismas fotones de dispersión Raman, lo que indica que la intensidad de las bandas PMI puede ser notablemente alta. Por lo tanto, podemos concluir que la PMI puede ser un mecanismo físico adecuado para el desarrollo de fuentes de luz de banda estrecha polarizada de alto rendimiento con bajo ruido de fondo.

En el capítulo 6 recopilamos el trabajo realizado en relación a la generación dual y simultanea de FWM escalar y PMI en MOFs, y a los experimentos para la sintonización simultánea de las bandas producidas por ambos efectos no lineales.

Las especificaciones de las fibras para la generación simultánea de ambos efectos no lineales requirieron un ajuste fino de las propiedades de guiado, que se consiguió utilizando MOFs infiltradas con soluciones de etanol-agua. La caracterización de la polarización de los espectros de luz resultantes a la salida de los MOF nos permitió identificar qué bandas espectrales eran producidas por PMI y cuales por FWM escalar.

Respecto a la sintonización de ambos efectos no lineales, implementamos dos métodos para controlar simultáneamente la posición espectral de las bandas producidas por dichos efectos no lineales. El primero se basa en rellenar los agujeros del MOF con soluciones de etanol-agua de diferentes concentraciones. El índice de refracción de las soluciones depende de la concentración de etanol. A su vez, la birrefringencia y la dispersión cromática varían con el índice de refracción en la región de los agujeros. Así, la localización espectral de las bandas de PMI y FWM generadas, se pudo variar en un rango amplio controlando la concentración de etanol (EtOH) de la solución. El segundo método se basa en las propiedades termo-ópticas del líquido infiltrado en el MOF, similar a la técnica empleada en el Capítulo 5.

En cuanto a los resultados obtenidos mediante el primer método, hemos demostrado que es posible sintonizar las bandas de FWM en un amplio rango de frecuencias. Hemos demostrado experimentalmente que el desplazamiento de frecuencia del FWM aumenta con la concentración de EtOH, mientras que disminuye para las bandas de PMI, conforme a las conclusiones teóricas. En el mejor resultado, el desplazamiento de frecuencia Ω de las bandas de FWM se sintonizó desde 2302 cm^{-1} hasta 4028 cm^{-1}, en una MOF infiltrada con soluciones con concentraciones de EtOH desde 0 %wt. a 44 %wt. (fracción en peso). Respecto a las bandas de PMI, el mejor resultado comprende la variación de Ω desde 391 cm^{-1} hasta 1188 cm^{-1}, para soluciones con concentraciones de EtOH entre 8 %wt al 100 %wt. En estos experimentos, se consiguió ajustar el desplazamiento en

frecuencia (o equivalentemente la posición espectral) de las bandas de FWM y PMI en un rango amplio. Sin embargo, este método no es un método dinámico en el sentido de que la sintonización de las bandas PMI/FWM requiere llenar y vaciar los agujeros de las MOFs.

El segundo método nos permitió la sintonización simultánea de las bandas PMI y FWM en un rango espectral amplio, de forma dinámica. El índice de refracción de una determinada solución infiltrada en la fibra se sintonizó continuamente en torno a un valor inicial fijado por la concentración de etanol-agua aprovechando el efecto termo-óptico. Utilizando esta técnica, fue posible generar bandas de PMI y FWM de amplitud significativa y bien separadas espectralmente del bombeo, y, además, de sintonizarlas de manera continua y dinámica cambiando la temperatura de la fibra. Dado que el coeficiente termo-óptico de las soluciones es negativo, el desplazamiento de las bandas es tal que, al aumentar la temperatura, las bandas de FWM se aproximan al bombeo mientras que las bandas de PMI se alejan del mismo. En estos experimentos, los mayores rangos de sintonización obtenidos fueron desde 3851 cm^{-1} a 1631 cm^{-1} para las bandas de FWM, en un rango de temperatura de 23 °C a 96 °C, y para las bandas de PMI, desde 1023 cm^{-1} a 1583 cm^{-1}, en un rango de temperatura de 23 °C a 66 °C.

Cabe comentar que las propiedades de polarización de la luz generada por PMI y por FWM pueden dar lugar a diversas combinaciones que pueden permitir el desarrollo de fuentes de luz sintonizables, simplemente filtrando las longitudes de onda deseadas con dispositivos ópticos adecuados, como polarizadores o filtros de paso de banda. Además, para aplicaciones en las que los efectos de la polarización son despreciables, una fuente de luz de banda estrecha que cubra casi el espectro del infrarrojo cercano puede basarse en la combinación de las bandas producidas por FWM y PMI.

Por último, en el capítulo 6 incluimos dos aplicaciones prácticas basadas en la respuesta de la banda *signal* del FWM a los cambios de índice de refracción y/o temperatura. En las MOFs infiltradas de líquido, la dependencia de las longitudes de onda del FWM con el índice de refracción del líquido de relleno puede utilizarse para el desarrollo de refractómetros altamente sensibles para soluciones de base acuosa. La segunda aplicación está relacionada con la caracterización de las propiedades termo-ópticas de los líquidos. El método se basa en la respuesta térmica de la banda de *signal* de FWM producida en un MOF lleno del líquido bajo prueba. Para demostrar la viabilidad de la propuesta, se investigó una solución de etanol-agua. El método pudo mostrar (y cuantificar) la dependencia no lineal del índice de refracción de dicha solución con la temperatura. Esta técnica puede aplicarse para caracterizar la respuesta termo-óptica de muchos otros líquidos, siempre que el índice de refracción del líquido sea inferior al índice de refracción de la sílice.

A lo largo de esta tesis, han surgido varias ideas para diferentes experimentos y aplicaciones basadas en los efectos PMI/FWM como trabajo futuro. Por ejemplo, la dependencia de la posición espectral de las bandas de PMI con la birrefringencia puede ser explotada para medir deformación o curvatura de una fibra óptica. Además, los parámetros de una fibra, como la birrefringencia o el parámetro no lineal, también pueden medirse basándose en la respuesta de desplazamiento de frecuencia de la PMI. En la misma dirección, hemos señalado anteriormente la posibilidad de desarrollar sensores de fibra basados en la respuesta de la PMI a las variaciones del índice de refracción de un líquido infiltrado en una MOF y la posibilidad de caracterizar la respuesta térmica de una amplia variedad de soluciones de base acuosa. Por último, nos gustaría destacar que las técnicas de sintonización de FWM/PMI y los rangos de sintonización alcanzados en nuestros experimentos abren un abanico de nuevas posibilidades que pueden fundamentar el desarrollo de nuevas fuentes de luz versátiles con aplicaciones en diferentes campos.

Chapter 1
Introduction

Light sources based on nonlinear optics are of great interest for photonic technologies. Nonlinearities arise as a response of a medium when it is subjected to a strong electromagnetic field. As a result of light-matter interaction, unique effects can occur, for example: self-focusing (or defocusing) of a light beam; mixing of waves at different frequencies; modulation of the optical properties of the material (refractive index or absorption coefficient); generation of new frequencies; spectral broadening of a narrow optical pulse; to name a few. The effects related to the mixing or generation of new frequencies are the most relevant nonlinear effects for the development of light sources. The light sources produced by nonlinear effects exhibit suitable spectro-temporal properties that allow them to be exploited in different areas, from fundamental research to applications related to biomedicine, quantum optics, remote sensing, telecommunications and materials analysis, etc. [1–3].

In photonic applications, several materials are used to efficiently excite nonlinear effects, such materials are also known as nonlinear optical materials and their relevance is related to the desired application. Among them, we can find [4]: semiconductors, organic and polymeric materials, electro-optical crystals, liquid crystals and photonic crystals (1D, 2D and 3D).

Optical fiber technology enables the development of light sources with all the benefits of an optical fiber, the perfect example is an all-fiber laser. In addition, the

advent of microstructured optical fibers (MOFs), also known as photonic crystal fibers (PCFs), has broadened the potentiality of optical fibers for nonlinear applications. The invention of MOFs was a watershed for nonlinear applications based on optical fiber technology. The strong optical field density confined in small area, the feasibility of long interaction lengths, high nonlinearity and increased flexibility for chromatic dispersion make MOFs a suitable platform for exciting nonlinear effects, and, therefore, for development of light sources based on nonlinear optical effects.

Nowadays, the most remarkable nonlinear light source is based on supercontinuum (SC) generation produced in MOF [5]. SC occurs in optical fibers when intense light with a narrow bandwidth propagating within the fiber, typically produced by a laser, experiences spectral broadening triggered by the interplay between the dispersive properties and nonlinearities of the MOF. Large bandwidth of SC light sources can be design, ranging from few hundreds of nm to bandwidths that almost covers the optical transparency window of fused silica. In general, SC light sources has average powers from several mW to few W, however, the power ratio carried by the different spectral components of the SC spectrum is relatively low. Due to the suitable spectro-temporal properties, SC light source has been broadly exploited in many areas, such as spectroscopy [6, 7], optical coherent tomography [8], bio-imaging [9], and still is an open research topic.

The nonlinear effects produced in an optical fiber also allow the development of narrowband light sources emitting at certain frequencies. Four-wave mixing (FWM) is a nonlinear effect that can be produced in an optical fiber which is capable of generating photons at different frequency from the excitation wavelength [10]. Thus, light generated by FWM allows designing light sources with dual-wavelength emission and narrowband gain. Nowadays, this type of light sources is not only of research interest, but applications for advanced microscopy based on the FWM

effect have already been developed [11]. In the present thesis, we focus our study on the generation of FWM in MOFs for the development of narrow bandwidth light sources. The FWM is an elastic nonlinear effect, in which the energy of the excitation photons is not transferred to the medium (optical fiber), but its energy is transferred to two new photons at different frequencies. FWM is a parametric process, so it requires the fulfillment of a phase-matching condition for it to occur efficiently. FWM is highly dependent on the chromatic dispersion and the nonlinear response of the fiber. In fact, phase matching occurs when the dispersion contribution and the nonlinear contribution are balanced at the frequencies of the FWM photons and the excitation photons. Ideally, once phase matching is achieved, the power of the pump is transferred to two spectral bands, typically referred to as *signal* and *idler* bands. The *signal* and *idler* bands occur at higher or lower frequencies, respectively. Depending on the fiber dispersion, FWM sidebands can be generated in different regions of the optical spectrum [12].

Depending on the polarization state of the pump light, the FWM sidebands can exhibit different properties, which is the evidence of the vector nature of FWM. In optical fibers, their birefringence together with the polarization state of the pump light are responsible for triggering different vector processes of FWM. For example, in a linearly polarized frame, the FWM sidebands may be co-polarized or orthogonally polarized. In the present work, we pay special attention to a particular case of vectorial FWM that can occur in weakly birefringent fibers, in which, the two generated FWM sidebands are co-polarized but orthogonally polarized with respect to the orientation of the polarization of the pump light. This vector case of FWM can effectively occur when the pumping light excites one of the eigenmodes which electric field is polarized along one major axis of the fiber (fast or slow), and thus the generated FWM sidebands are polarized along the orthogonal axis (slow or fast). This particular effect is known as polarization modulation instability (PMI) and allows the possibility to design polarized light sources.

Historical background

Nonlinear optics is a branch of physics that studies the phenomena that occur as a consequence of the modification of the optical properties of a material system by the presence of intense light. Nonlinear optical phenomena are "nonlinear" in the sense that they occur when the response of a material to an applied optical field depends in a nonlinear manner on the strength of the optical field. Typically, only laser light is sufficiently intense to modify the optical properties of a material system. In this sense, the birth of nonlinear optics comes just after the invention of the first functional laser in 1960 by Maiman [13]. The beginning of the field of nonlinear optics is often taken to be the discovery of harmonics generation by Franken et al. in 1961 [14]. However, before the invention of the laser, several theoretical predictions about nonlinear optical phenomena had already been made, in 1931 Goeppert and Mayer theoretically predicted the two-photon absorption [15]; in 1956 Buckingham proposed the theory of Kerr effect [16].

In the context of optical fibers, FWM was first observed soon after low loss fiber became available by Stolen et al. in 1974 [17]; they reported the generation of blue light through FWM when pumping light at 532 nm (green) together with a seeded signal light at 630 nm (red) propagated in a fused silica rod. In their experiments, phase-matching was accomplished for different guided modes, according with the far field pattern observed at the fiber output. In the following years FWM produced in optical fibers was extensively studied, FWM in single mode fibers was observed by Hill et al. in 1981 [18]; they reported the feasibility to measure the nonlinearity of a single-mode optical fiber through FWM effect.

The gain produced by FWM effect was proposed for all-fiber optical parametric amplifier (FOPA) [19, 20]. Different studies demonstrated that the efficiency of the FOPA was degraded mainly by the state of polarization of the pumping light and the birefringence of the fiber. It was observed that FWM

efficiency was the largest when both pump light and FWM sidebands were co-polarized. However, either the polarization of the pump light and the polarization of the *signal* and *idler* sidebands varied as they propagated along the fiber. The first theoretical description of vector FWM in optical fiber was reported by Inoue in 1992 [21], in this, the theory of vector FWM in a single-mode optical for general polarization states of pump light was described. One decade later, vector FWM theory was expanded by Lin and Agrawal in 2004 [22]. In their work, the influence of the polarization state of the pump light together with the FWM sidebands was considered to describe the efficiency of FWM for the implementation of FOPAs. Moreover, the basis for deriving the phase-matching equations in the frame of circular or linear polarized light was addressed.

In particular, the effect of PMI was predicted theoretically in single-mode fibers with low birefringence in 1988 by Wabnitz [23], a few years before the general theory of vector FWM was developed by Inoue. It was demonstrated that the interplay of fiber birefringence together with the polarization of the pumping light can lead the generation of the modulation instability of a continous wave pump propagating within an optical fiber, even for the normal dispersion regime. Wabnitz showed that a short optical pulse can be converted into a train of pulses due to the instability produced when two small perturbations (sidebands) arises from the coupling of the two polarizations of the fundamental mode. In 1981, Stolen et al. [24], experimentally observed the generation of two co-polarized sidebands propagating with orthogonal polarization with respect to the pump polarization. In their experiments two sidebands propagating in the fast axis of the fiber were produced by linearly polarized light oriented to the slow axis of the fiber, which is a particular case of PMI. However, it was until 1995 when the first experimental demonstration that claims the generation of PMI in single-mode optical fiber by Murdoch et.al. [25] was reported. In the context of MOFs, PMI was first observed in the

normal dispersion regime in a large-air-filling fraction MOF pumped near the zero-dispersion wavelength [26].

FWM based light source

The suitable temporal and spectral properties of FWM allow the implementation of light sources based on this nonlinear effect. In recent years, FWM has been exploited in many areas of interest, such as quantum optics and advanced microscopy. In addition, the FWM remains an open research topic for the development of optical parametric oscillators and resonators.

In the case of advanced microscopy based on Raman spectroscopy, stimulated Raman scattering (SRS) [27] and coherent anti-Stokes Raman spectroscopy (CARS) [28], can be used to increase the Raman signal intensity of a biological sample, in which two intense collinear laser beams irradiate the sample. One laser is held at constant frequency (Stokes), while the other is tunable (pump). When the frequency difference matches a Raman active resonant mode of the sample, the Raman signal emitted by the sample will be increased. Such spectroscopy techniques allow imaging of specific chemical groups. The requirements of a light source for SRS or CARS imaging can be supplied intrinsically by the tandem of fiber laser technology and FWM produced in a nonlinear MOF [29]. FWM based light sources for SRS/CARS bio-imaging require a wide tuning range of the *signal* band of FWM. The vibrational frequencies of the most representative functional groups are in the range from 1000 cm^{-1} to 3700 cm^{-1}. Recently, it was demonstrated that suitable light sources based on tunable FWM in MOFs can be attained by tuning the pump wavelength [11]. Large frequency shift of FWM sidebands was achieved in a MOF with the zero-dispersion wavelength near to the wavelength range of pump laser. However, many suitable lasers with sufficient pump power to excite nonlinear effects in an optical fiber do not always allow tuning of their emission wavelength.

They are usually lasers designed to operate at a fixed wavelength. Moreover, in those where it may be possible, the tuning range is generally limited to a few nm. A simple solution for broadband tuning of FWM sidebands at a fixed pump wavelength, can be achieved by means of tuning the dispersion of the MOF through a controlled external factor [30, 31].

FWM effect has also attracted the attention for the development of fiber-based photon sources in quantum photonics. The phenomenon of FWM occurring inside optical fibers provides a natural way to generate correlated photon pairs in a single spatial mode directly inside an optical fiber [32, 33]. However, the performance of fiber-based correlated photon-pair sources is severely deteriorated by the phenomenon of spontaneous Raman scattering (RS) that accompanies scalar FWM inevitably. In the past, stable polarization-entangled photon pairs has been generated by FWM with two orthogonal polarized pump sources [34, 35]. Since RS and FWM interaction is maximum when both effects are co-polarized and minimum for orthogonal polarization of FWM photons, the limitation induced by RS into correlated photons, can be managed with the polarization state of the pump and FWM photons. Therefore, PMI effect can be of interest for development of fiber-based correlated-photon pair sources since photons produced through PMI are intrinsically orthogonal polarized. In addition, the frequency at which PMI photons are produced, can be adjusted with the control of the fiber dispersion together with the fiber birefringence, in order to match the wavelength window of available detectors for quantum-photonics applications.

Recently PMI effect has attracted again the attention for fundamental research. Frequency comb generation in the presence of polarization effects induced by nonlinear mode coupling in microresonator devices has been investigated. PMI was theoretically predicted in driven microresonators [36] and was experimentally observed in a single Kerr microresonator, capable to emit two orthogonally

polarized individually coherent combs generated by cross-phase modulation [37]. In the context of optical fibers, PMI has been recently observed in a fiber Kerr resonator, built with 12 m long normal dispersion spun fiber ring cavity driven with a 1552.4 nm wavelength continous-wave laser.

Aims of the thesis

The objectives of this thesis can be divided into two parts, the first is related to the study of PMI and FWM generation in MOFs with different dispersion properties, the study also will include the design and fabrication of nonlinear MOFs. The second part is related to the development of practical tuning techniques to control the spectral position of the FWM and PMI sidebands over a wide spectral range.

The first objective of this work involved to study the main theoretical aspects of the FWM and PMI produced in an optical fiber. This study will allow us exploring the dependence of the fiber parameters on the phase-matching condition of both effects, and furthermore their relevance for the control of parametric wavelengths. This study serves for the development and description of the tuning techniques that will be employed throughout this thesis. In chapter 2, the theoretical description of FWM including its vector nature will be addressed.

We are also interested in MOFs design and fabrication, since most of the experiments related to FWM and PMI will be carried out on fibers designed and fabricated according to the desired application. Therefore, modeling the dispersion properties of a MOF as a function of its structural parameters is necessary for the fabrication of the nonlinear fibers that will be used in the experiments of the present work. In Chapter 3 we will address the modeling together with the fabrication

technique of the nonlinear MOFs. In addition, the experimental procedure followed to characterize and excite the nonlinear effects in the MOFs will also be addressed.

One of the objectives of this work is to study the relevance of fiber dispersion on the phase-matching condition of FWM and PMI in order to control the spectral location of the sidebands generated by such effects. Therefore, Chapter 4 will be devoted to the study of PMI generation in fibers with tailored dispersion design, including MOFs filled with optical liquids.

We are interested in developing practical tuning techniques for widely detuned sidebands produced by FWM and PMI. We explored different tuning techniques that rely on the control of fiber parameters through physical factors such as temperature or mechanical stress. These external factors are related to linear variations of phase birefringence induced by the elasto-optic effect and to simultaneous variations of fiber dispersion and birefringence induced by the thermo-optic effect. In Chapter 5, we will explore the possibility of controlling PMI sidebands by inducing linear birefringence in a fiber through fiber bending and also by tensioned-coiled fibers in cylindrical molds. In addition, we will study the tuning performance of PMI sidebands with temperature control by infiltrating liquids into MOFs with suitable refractive index and high thermo-optic coefficients.

Finally, in Chapter 6, will deal with the experimental study of the simultaneous generation of FWM and PMI in MOFs with proper dispersion for their generation. We will address the possibility of simultaneously controlling PMI and FWM sidebands by two mechanisms. We will present the viability to achieve tuning of the PMI and FWM sidebands by fine-tuning of the refractive index of the microstructured region of the fiber. In addition, we will also study the possibility of tuning the PMI and FWM sidebands over a wide wavelength range by thermal control, following the tuning technique employed in Chapter 5.

References

1. T. Gottschall, T. Meyer, M. Baumgartl, C. Jauregui, M. Schmitt, J. Popp, J. Limpert, and A. Tünnermann, "Fiber-based light sources for biomedical applications of coherent anti-Stokes Raman scattering microscopy," Laser Photonics Rev. **9**, 435–451 (2015).

2. E. Garmire, "Nonlinear optics in daily life," Opt. Express **21**, 30532 (2013).

3. E. Garmire, "Overview of Nonlinear Optics," in *Nonlinear Optics* (IntechOpen, 2012).

4. C. Li, "Importance of Nonlinear Optics," in *Nonlinear Optics: Principles and Applications* (Springer Singapore, 2017), pp. 1–5.

5. J. M. Dudley, G. Genty, and S. Coen, "Supercontinuum generation in photonic crystal fiber," Rev. Mod. Phys. **78**, 1135–1184 (2006).

6. J. M. Langridge, T. Laurila, R. S. Watt, R. L. Jones, C. F. Kaminski, and J. Hult, "Cavity enhanced absorption spectroscopy of multiple trace gas species using a supercontinuum radiation source," Opt. Express **16**, 10178 (2008).

7. H. Kano and H. O. Hamaguchi, "Femtosecond coherent anti-Stokes Raman scattering spectroscopy using supercontinuum generated from a photonic crystal fiber," in *Applied Physics Letters* (American Institute of PhysicsAIP, 2004), Vol. 85, pp. 4298–4300.

8. S. Moon and D. Y. Kim, "Ultra-high-speed optical coherence tomography with a stretched pulse supercontinuum source," Opt. Express **14**, 11575 (2006).

9. A. Labruyère, A. Tonello, V. Couderc, G. Huss, and P. Leproux, "Compact supercontinuum sources and their biomedical applications," Opt. Fiber Technol. **18**, 375–378 (2012).

10. G. P. Agrawal, *Nonlinear Fiber Optics* (Elsevier Inc., 2019).

11. M. Baumgartl, M. Chemnitz, C. Jauregui, T. Meyer, B. Dietzek, J. Popp, J. Limpert, and A. Tünnermann, "All-fiber laser source for CARS microscopy based on fiber optical parametric frequency conversion," Opt. Express **20**, 4484 (2012).

12. C. Lin, W. A. Reed, H.-T. Shang, and A. D. Pearson, "Phase matching in the minimum-chromatic-dispersion region of single-mode fibers for stimulated four-photon mixing," Opt. Lett. **6**, 493 (1981).

13. T. H. Maiman, "Optical and microwave-optical experiments in ruby," Phys. Rev. Lett. **4**,

564–566 (1960).

14. P. A. Franken, A. E. Hill, C. W. Peters, and G. Weinreich, "Generation of optical harmonics," Phys. Rev. Lett. **7**, 118–119 (1961).

15. M. Göppert-Mayer, "Über Elementarakte mit zwei Quantensprüngen," Ann. Phys. **401**, 273–294 (1931).

16. A. D. Buckingham and J. A. Pople, "Theoretical studies of the Kerr effect I: Deviations from a linear polarization law," Proc. Phys. Soc. Sect. A **68**, 905–909 (1955).

17. R. H. Stolen, J. E. Bjorkholm, and A. Ashkin, "Phase-matched three-wave mixing in silica fiber optical waveguides," Appl. Phys. Lett. **24**, 308–310 (1974).

18. K. O. Hill, D. C. Johnson, B. S. Kawasaki, and R. I. MacDonald, "Cw three-wave mixing in single-mode optical fibers," J. Appl. Phys. **49**, 5098–5106 (1978).

19. M. Ohashi, K. I. Kitayama, Y. Ishida, and N. Uchida, "Phase-matched light amplification by three-wave mixing process in a birefringent fiber due to externally applied stress," Appl. Phys. Lett. **41**, 1111–1113 (1982).

20. T. Hasegawa, K. Inoue, and K. Oda, "Polarization Independent Frequency Conversion By Fiber Four-Wave Mixing With A Polarization Diversity Technique," IEEE Photonics Technol. Lett. **5**, 947–949 (1993).

21. K. Inoue, "Polarizers Effect on Four-Wave Mixing Efficiency in a Single-Mode Fiber," IEEE J. Quantum Electron. **28**, 883–894 (1992).

22. Q. Lin and G. P. Agrawal, "Vector theory of four-wave mixing: polarization effects in fiber-optic parametric amplifiers," J. Opt. Soc. Am. B **21**, 1216 (2004).

23. S. Wabnitz, "Modulational polarization instability of light in a nonlinear birefringent dispersive medium," Phys. Rev. A **38**, 2018–2021 (1988).

24. R. H. Stolen, M. A. Bösch, and C. Lin, "Phase matching in birefringent fibers," Opt. Lett. **6**, 213 (1981).

25. S. G. Murdoch, R. Leonhardt, and J. D. Harvey, "Polarization modulation instability in weakly birefringent fibers," Opt. Lett. **20**, 866 (1995).

26. R. J. Kruhlak, G. K. Wong, J. S. Chen, S. G. Murdoch, R. Leonhardt, J. D. Harvey, N. Y. Joly, and J. C. Knight, "Polarization modulation instability in photonic crystal fibers," Opt.

Lett. **31**, 1379 (2006).

27. C. W. Freudiger, W. Min, G. R. Holtom, B. Xu, M. Dantus, and X. S. Xie, "Highly specific label-free molecular imaging with spectrally tailored excitation-stimulated Raman scattering (STE-SRS) microscopy," Nat. Photonics 2010 52 **5**, 103–109 (2011).

28. M. D. Duncan, J. Reintjes, and T. J. Manuccia, "Scanning coherent anti-Stokes Raman microscope," Opt. Lett. **7**, 350 (1982).

29. T. Gottschall, M. Baumgartl, A. Sagnier, J. Rothhardt, C. Jauregui, J. Limpert, and A. Tünnermann, "Fiber-based source for multiplex-CARS microscopy based on degenerate four-wave mixing," Opt. Express **20**, 12004 (2012).

30. L. Velázquez-Ibarra, A. Díez, E. Silvestre, and M. V. Andrés, "Wideband tuning of four-wave mixing in solid-core liquid-filled photonic crystal fibers," Opt. Lett. **41**, 2600 (2016).

31. L. Velazquez-Ibarra, A. Diez, E. Silvestre, and M. V. Andres, "Tunable Four-Wave Mixing Light Source Based on Photonic Crystal Fibers with Variable Chromatic Dispersion," J. Light. Technol. **37**, 5722–5726 (2019).

32. Q. Lin, F. Yaman, and G. P. Agrawal, "Photon-pair generation in optical fibers through four-wave mixing: Role of Raman scattering and pump polarization," Phys. Rev. A - At. Mol. Opt. Phys. **75**, 023803 (2007).

33. Q. Lin, F. Yaman, and G. P. Agrawal, "Photon-pair generation by four-wave mixing in optical fibers," Opt. Lett. **31**, 1286 (2006).

34. X. Li, P. L. Voss, J. E. Sharping, and P. Kumar, "Optical-fiber source of polarization-entangled photons in the 1550 nm telecom band," Phys. Rev. Lett. **94**, 053601 (2005).

35. H. Takesue and K. Inoue, "Generation of polarization-entangled photon pairs and violation of Bell's inequality using spontaneous four-wave mixing in a fiber loop," Phys. Rev. A - At. Mol. Opt. Phys. **70**, (2004).

36. T. Hansson, M. Bernard, and S. Wabnitz, "Modulational instability of nonlinear polarization mode coupling in microresonators," J. Opt. Soc. Am. B **35**, 835 (2018).

37. C. Bao, P. Liao, A. Kordts, L. Zhang, A. Matsko, M. Karpov, M. H. P. Pfeiffer, G. Xie, Y. Cao, A. Almaiman, M. Tur, T. J. Kippenberg, and A. E. Willner, "Orthogonally polarized frequency comb generation from a Kerr comb via cross-phase modulation," Opt. Lett. **44**, 1472 (2019)

Chapter 2
Theory of four-wave mixing

In this chapter, we describe the main theoretical aspects of the nonlinear effect of FWM. We will address the general FWM theory for optical fibers by deriving the coupled equations for the amplitude of the fields involved in such process. The FWM phase-matching equation along with the spectral gain of its sidebands are derived under the scalar approximation, and then we extend the study for fibers with low birefringence where a vector description of the electromagnetic fields is required. In particular, we derive the coupled amplitude equations together with the phase-matching equations for the possible FMW processes allowed in an optical fiber when the pump wave is linearly polarized, which is the case of the light source used throughout this thesis. Since the fiber chromatic dispersion plays an important role for the fulfillment of the FWM phase-matching conditions (both in the vector and scalar cases), the description of the fiber dispersion is also addressed at the beginning of this chapter.

Following the theoretical study of FWM, we were able to build a model to accurately describe the effect of FWM in optical fibers that allows us exploring the dependence of FWM on the different optical parameters. Moreover, in this chapter, we analyze the physical principles in which the different techniques implemented for controlling the spectral position of FWM are based. Numerical simulations are also performed to show the potential of the different methods.

2.1 Chromatic dispersion of optical fibers

Chromatic dispersion is a measure of the degree to which the group velocity changes as a function of wavelength. It plays a very important role in fiber technology. Chromatic dispersion has an important impact on the propagation of light pulses, because a pulse has a finite spectral width, so that, dispersion can cause frequency-dependent phase changes. Consequently, its frequency components propagate with different group velocities. It is said that the pulse is "chirped", meaning that the instantaneous optical frequency changes within the pulse. In applications based on linear propagation such as in optical telecommunications, chromatic dispersion is a relevant factor since it determines the temporal broadening of optical pulses, which is a limiting factor of the bandwidth capacity of a given network. In the nonlinear regime, dispersion is also a key fiber parameter since most nonlinear effects require low values of dispersion, and some nonlinear effects require a given sign of the dispersion to be able to occur.

By constitution, optical fibers are dispersive media because, in part but not only, the dielectric material of which they are composed (commonly SiO_2) is also dispersive. In general, the response of the material to the interaction with an electromagnetic wave depends on the optical frequency ω. This property of the material is quantified by the frequency dependence of the refractive index of the fiber $n(\omega)$. The origin of the material chromatic dispersion is related to the characteristic resonance frequencies at which the medium absorbs electromagnetic radiation through the oscillations of bound electrons. For optical wavelengths far from the absorption resonances, the refractive index of most glasses, and in particular of fused silica can be well approximated through a Sellmeier equation of order $m = 3$,

$$n(\lambda) = 1 + \sum_{j}^{m} \frac{B_j \lambda^2}{\lambda^2 - \lambda_j^2} \qquad (2.1)$$

where λ is the optical wavelength, and λ_j and B_j represent the wavelength and the strength of the absorption resonances. For fused silica, the Sellmeier parameters were obtained experimentally [1] and found to be B_1=0.6961663, B_2=0.4079426, B_3=0.8974794, λ_1=0.0684043 μm, λ_2=0.1162414 μm and λ_1=9.9896161 μm. Fig. 2.1 shows the chromatic dependence of the refractive index of fused silica.

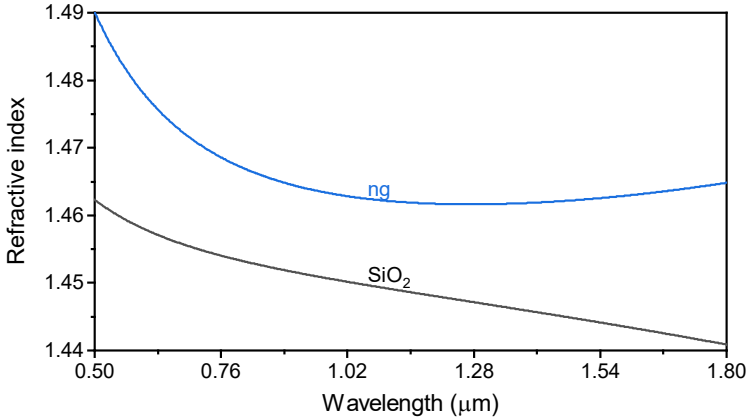

Figure 2.1. Refractive index (black) and group index (blue) of fused silica as a function of wavelength.

In optical fibers, chromatic dispersion is attributed to three sources of dispersion: (i) Material dispersion, (ii) waveguide dispersion and (iii) mode dispersion. Material dispersion, as mentioned above, is caused by the wavelength dependence of the refractive index of fused silica. Waveguide dispersion is related to the wave guiding phenomena [2]. In optical fibers, the fields of guided modes overlap partially the core and partially the cladding. The *mode* field diameter changes with wavelength. Since the refractive index is different in the core than in the cladding, a change in mode field diameter also results in a change in the group velocity. Finally, mode dispersion happens due to the existence of several modes

propagating in the fiber, since each mode propagates with different propagation factor and velocities. The latter contribution, does not happen in single-mode optical fibers in which only the fundamental mode (HE_{11}) is guided by the fiber. In this work, we employ MOFs that operate as single-mode fibers in the experimental wavelength range. Therefore, the contribution of mode dispersion can be neglected. Mathematically the effects of fiber dispersion are taken into account by expanding the propagation factor of the guided mode β in a Taylor series around the carrier frequency ω_0,

$$\beta(\omega) = n_{eff}(\omega)\frac{\omega}{c} = \beta_0 + \beta_1(\omega-\omega_0) + \frac{1}{2}\beta_2(\omega-\omega_0)^2 + \ldots \qquad (2.2)$$

where n_{eff} is the effective index of the guided mode and,

$$\beta_m = \left(\frac{\partial^m \beta}{\partial \omega^m}\right)_{\omega_0} \qquad m = 0,\ 1,\ 2,\ldots \qquad (2.3)$$

The different coefficients β_m are related to some propagation quantities. In particular, β_1 is the inverse of the group velocity v_g,

$$\beta_1 = \frac{1}{c}\left(n_{eff} + \omega\frac{dn_{eff}}{d\omega}\right) = \left(\frac{1}{v_g}\right) = \frac{n_g}{c} \qquad (2.4)$$

and β_2 contains the dependence of the inverse of the group velocity with frequency. In the bibliography, β_2 is referred as the group velocity dispersion (GVD),

$$\beta_2 = \frac{1}{c}\left(2\frac{dn_{eff}}{d\omega} + \omega\frac{d^2 n_{eff}}{d\omega^2}\right) = \frac{d}{d\omega}\left(\frac{1}{v_g}\right) \qquad (2.5)$$

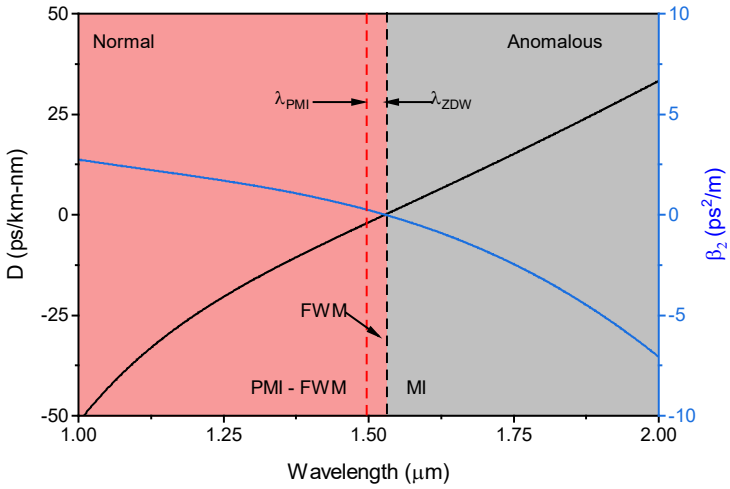

Figure 2.2. Chromatic dispersion (black) and β_2 parameter (blue) as a function of wavelength of an optical fiber. Dispersion regimes are denoted by the shadow regions. Vertical dashed lines indicate the λ_{ZDW} and λ_{PMI}.

In some areas of optical fibers, chromatic dispersion is commonly described through the parameter D which is related to the GVD parameter. The dispersion parameter D is defined as $d\beta_1 / d\lambda$, and is expressed in terms of β_2 and n_{eff} as follows:

$$D = \frac{d\beta_1}{d\lambda} = -\frac{2\pi}{\lambda^2}\beta_2 = -\frac{\lambda}{c}\frac{d^2 n}{d\lambda^2} \qquad (2.6)$$

Figure 2.2 shows an example of the wavelength dependence of dispersion and β_2 parameter of an optical fiber (*numerical aperture: 0.17*, *core diameter: 2.18 μm*). The most notable feature is that both β_2 and D vanish at a wavelength of about 1.52 μm and change sign for longer wavelengths. This wavelength is referred to as the *zero-dispersion wavelength* and is denoted as λ_{ZDW}. One can think that the dispersion of a fiber can be suppressed at the λ_{ZDW}, however, due to higher order dispersion (HOD) contributions ($m \geq 3$ in Eq. 2.3), an optical fiber can still be dispersive. For instance, the term β_3 is responsible for the distortion (asymmetric broadening) of a short optical pulse propagating in a single-mode optical fiber [3].

According to the sign of fiber dispersion, it is usual to talk about two dispersion regimes: normal dispersion, for wavelengths with negative values of D (positive GVD), and anomalous dispersion for wavelengths with positive values of D (negative GVD). In the case of the example depicted in Fig. 2.2, normal dispersion regime happens when the optical wavelength is lower than λ_{ZDW} and the anomalous dispersion regime when the optical wavelength is larger than λ_{ZDW}.

As mentioned above, fiber dispersion plays an important role in the context of nonlinear optics, due to its strong dependence on that fiber parameter. In the particular case of FWM, depending on the dispersion regime and the dispersion slope (loosely named dispersion profile), the FWM effect can exhibit different properties. For example, in optical fibers with anomalous dispersion at the excitation wavelength, scalar FWM can be produced with FWM sidebands generated near the excitation wavelength. This particular type of FWM is commonly known as modulation instability (MI). When the fiber dispersion at the excitation wavelength is normal, largely detuned FWM sidebands can be generated. Moreover, in birefringent fibers, various FWM vector processes can be generated in both dispersion regimes. In particular, for fibers with low birefringence, the PMI effect only occurs in the normal dispersion regime and exhibits a wavelength cutoff (λ_{PMI}), so that if pump wavelength is above λ_{PMI}, PMI cannot be produced. The above-mentioned regimes for FWM processes are illustrated in Fig. 2.2.

2.2 Four-wave mixing in optical fibers

Spontaneous four-wave mixing is a nonlinear process in which two photons of different frequency transfers their energy to two new photons. FWM photons are often known as *signal* and *idler* photons. When *signal*/*idler* photons are produced from two pump photons at the same frequency, the FWM process is known as degenerated. FWM is considered as a parametric process and it is related to the

modulation of the refractive index of the medium through Kerr effect. Physically speaking, FWM arises from the nonlinear response of bounded electrons of a material in the presence of an intense electromagnetic field. In general, the polarization induced in the dielectric medium by the electromagnetic field contains terms that do not depend linearly on the electric field, whose magnitude is governed by their nonlinear susceptibilities $\chi^{(n)}$, [4 – 6]. The resulting nonlinear effects can be classified as second-order or third-order parametric processes, depending on whether the second-order susceptibility $\chi^{(2)}$, or the third-order susceptibility $\chi^{(3)}$, is responsible for them. Both exhibit instantaneous response in time scale of ~fs. In the context of optical fibers, third order parametric processes are the most exploited in nonlinear optics. In contrast, the second-order nonlinear effects (e.g., second-harmonic generation) are more difficult to occur in silica-based optical fibers. The centrosymmetric nature of fused silica molecules makes $\chi^{(2)}$ to vanish. The third-order parametric processes involve the nonlinear interaction among four optical waves and include the phenomena such as FWM and third-harmonic generation.

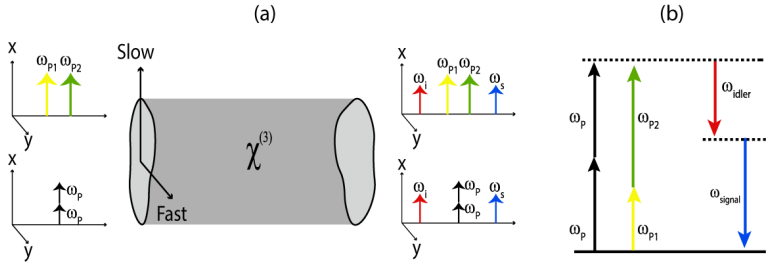

Figure 2.3. (a) Schematic of scalar FWM process in an optical fiber for pump with linear polarization. (b) Energy level diagram for degenerated and non-degenerate FWM.

Fig. 2.3 shows a schematic describing the FWM process generated in an optical fiber and the energy level diagram representation. In practice, due to the low efficiency of FWM in optical fibers, the remaining pump photons are also observable.

In this section the theoretical description of FWM in optical fibers is addressed, we follow the classical theory of FWM reported in [7–9] to describe the nonlinear propagation of an electromagnetic field in an optical fiber. To obtain a complete picture of the FWM effect with the experimental observations of this thesis, we derive the coupled differential equations describing the evolution of the FWM electric fields amplitude under the continuous wave (CW) approximation. In our experiments, a pulsed light source with pulse duration of few hundred of ps was used. Although it is not a CW regime, it is considered as a quasi-CW regime since the pulse duration is many orders of magnitude larger than the time response of the nonlinear effects investigated. Then, the formulation derived to describe FWM under CW pumping is suitable to quasi-CW pump regime.

First, we begin by defining Maxwell's equations for a charge-free, nonconducting medium (such as an optical fiber), these equations take the form,

$$\nabla \times \mathbf{E} = -\frac{\partial \mathbf{B}}{\partial t} \qquad (2.7)$$

$$\nabla \times \mathbf{H} = \frac{\partial \mathbf{D}}{\partial t} \qquad (2.8)$$

$$\nabla \cdot \mathbf{D} = 0 \qquad (2.9)$$

$$\nabla \cdot \mathbf{B} = 0 \qquad (2.10)$$

where $\boldsymbol{E\ (r,\ t)}$ and $\boldsymbol{H\ (r,\ t)}$ are the electric and magnetic field vectors, respectively, and $\boldsymbol{D}$ and $\boldsymbol{B}$ are the electric and magnetic flux densities. The flux densities arise from the response of the dielectric medium (which is the material of a fiber) to the presence of an electromagnetic wave propagating within the material and are related through the constitutive equations, as follows:

$$\mathbf{D} = \varepsilon_0 \mathbf{E} + \mathbf{P} \qquad (2.11)$$

$$\mathbf{B} = \mu_0 (\mathbf{H} + \mathbf{M}) \qquad (2.12)$$

where ε_0 is the vacuum permittivity, μ_0 is the vacuum permeability, and $\boldsymbol{P}$ and $\boldsymbol{M}$ are the induced electric and magnetic polarizations. For a non-magnetic medium such as optical fibers, $\boldsymbol{M}= 0$.

Taking the curl of equation 2.7 and after some simplifications (using equations 2.8, 2.11, and 2.12) the wave equation can be obtained as a function of $\boldsymbol{E(r, t)}$ and $\boldsymbol{P(r, t)}$ as follows

$$\nabla^2\mathbf{E} - \frac{1}{c^2}\frac{\partial \mathbf{E}}{\partial t^2} = \mu_0 \frac{\partial^2 \mathbf{P}}{\partial t^2}, \qquad (2.13)$$

where the relation $\varepsilon_0 \cdot \mu_0 = 1/c^2$ was also used. In general, for optical fibers the operation wavelength range (typically from $0.5\ \mu m$ to $2\ \mu m$) is far from the resonances of the fused silica, then one can evaluate $\boldsymbol{P(r,t)}$ as function of the electric field, using the following phenomenological relation [5],

$$\mathbf{P} = \varepsilon_0(\chi^{(1)} \cdot \mathbf{E} + \chi^{(2)} : \mathbf{EE} + \chi^{(3)} \vdots \mathbf{EEE} + ...) \qquad (2.14)$$

where $\chi^{(n)}$ is the *n-th* order of the electric susceptibility tensor (of rank n+1) of the material. The polarization can then be rewritten in terms of its linear and nonlinear contribution as,

$$\mathbf{P} = \mathbf{P}_L + \mathbf{P}_{NL} \qquad (2.15)$$

$\boldsymbol{P_L}$ is related to $\boldsymbol{E}$ trough the relation,

$$\mathbf{P}_L(r,t) = \varepsilon_0 \int_{-\infty}^{\infty} \chi^{(1)}(t-t') \cdot \mathbf{E}(r,t')dt' \qquad (2.16)$$

The dependence of $\boldsymbol{P_{NL}}$ with the electric field $\boldsymbol{E}$ is quite more involved and, in general, it includes several nonlinear contributions. If Raman contribution are neglected, which in our case it makes sense since the experiments were carried out with short fiber sections, taking into account the instantaneous response of the polarizability of the material, and including effects only related to the third-order nonlinear susceptibility, the nonlinear term $\boldsymbol{P_{NL}}$ takes the form:

$$\mathbf{P}_{NL}(r,t) = \varepsilon_0 \chi^{(3)} \vdots \mathbf{E}(r,t)\mathbf{E}(r,t)\mathbf{E}(r,t) \qquad (2.17)$$

where (⋮) indicates the triple inner product. If we assume that the nonlinear response is isotropic for silica fibers [5], the $\chi^{(3)}$ has 21 nonzero components among which only four are independent, thus the third-order nonlinear properties of silica fibers can be expressed as below:

$$\chi_{ijkl}^{(3)} = \frac{1}{3}\chi_{xxxx}^{(3)}(\delta_{ij}\delta_{kl} + \delta_{ik}\delta_{jl} + \delta_{il}\delta_{jk}) \qquad (2.18)$$

where δij is a Kronecker delta. Due to the permutation symmetry of $\chi^{(3)}$ [10] the independent parameters are related to themselves and can be expressed in terms of the single parameter as:

$$\chi_{xxyy}^{(3)} = \chi_{xyxy}^{(3)} = \chi_{xyyx}^{(3)} = \frac{\chi_{xxxx}^{(3)}}{3} \qquad (2.19)$$

In the case of nondegenerate FWM, four distinct optical fields propagate simultaneously inside the optical fiber at different frequencies (ω_j, j = 1 - 4) with arbitrary polarizations (see Fig. 2.3(b)), therefore the total electric field satisfying the Maxwell wave equation can be decomposed as

$$\mathbf{E}(r,t) = \frac{1}{2}\sum_{j=1}^{4}\mathbf{E}_j e^{-i\omega_j t} + c.c. \qquad (2.20)$$

where $\boldsymbol{E_j}$ is the slow varying amplitude (complex) of the electric field oscillating at a given frequency ω_j. In the following procedures, for ω_j with $j = 1, 2$ refers to the frequency of the pump photons, whereas for $j = 3, 4$ refers to the *signal* and *idler* photons, respectively. The term c.c. refers to the complex conjugate of the electric field. $\boldsymbol{P_{NL}(r,t)}$ can be written in a similar fashion as,

$$\mathbf{P}_{NL}(r,t) = \frac{1}{2}\sum_{j=1}^{4}\mathbf{P}_j e^{-i\omega_j t} + c.c. \qquad (2.21)$$

By introducing Eqs. 2.19-2.21 into Eq. 2.17 and solving for the pump waves (i.e., *j = 1, 2*), the induced nonlinear polarization contribution is given by,

$$\mathbf{P}_j(\omega_j) = \frac{\varepsilon_0 \chi^{(3)}_{xxxx}}{4}[(\mathbf{E}_j \cdot \mathbf{E}_j)\mathbf{E}^*_j + 2(\mathbf{E}^*_j \cdot \mathbf{E}_j)\mathbf{E}_j + 2(\mathbf{E}^*_m \cdot \mathbf{E}_m)\mathbf{E}_j + 2(\mathbf{E}_m \cdot \mathbf{E}_j)\mathbf{E}^*_m + 2(\mathbf{E}^*_m \cdot \mathbf{E}_j)\mathbf{E}_m] \quad (2.22)$$

where *j* and *m* are *1* or *2* (with $j \neq m$). In the latter equation, we considered there is no pump depletion i.e., the *signal* and *idler* waves have not exceeded the intensities of the pump waves. Following the same procedure, we derive the nonlinear polarization contribution at the *signal* and *idler* frequencies,

$$\begin{aligned}\mathbf{P}_j(\omega_j) = \frac{\varepsilon_0 \chi^{(3)}_{xxxx}}{2}[&(\mathbf{E}^*_1 \cdot \mathbf{E}_1)\mathbf{E}_j + (\mathbf{E}_1 \cdot \mathbf{E}_j)\mathbf{E}^*_1 \\ &+ (\mathbf{E}^*_1 \cdot \mathbf{E}_j)\mathbf{E}_1 + (\mathbf{E}^*_2 \cdot \mathbf{E}_2)\mathbf{E}_j + (\mathbf{E}_2 \cdot \mathbf{E}_j)\mathbf{E}^*_2 \\ &+ (\mathbf{E}^*_2 \cdot \mathbf{E}_j)\mathbf{E}_2 + (\mathbf{E}^*_m \cdot \mathbf{E}_1)\mathbf{E}_2 + (\mathbf{E}^*_m \cdot \mathbf{E}_2)\mathbf{E}_1 \\ &+ (\mathbf{E}_1 \cdot \mathbf{E}_2)\mathbf{E}^*_m]\end{aligned} \quad (2.23)$$

where *j* and *m* are 3 or 2 (*signal* and *idler*), with $j \neq m$.

In general, under non-depleted pump conditions, FWM includes the combination of the nonlinear effects of self-phase modulation (SPM), and cross-phase modulation (XPM). SPM is a nonlinear effect that refers to the self-induced phase shift experienced by an intense optical field during its propagation and leads to the spectral broadening of the optical pulse; XPM refers to the phase shift of an optical field induced by another field with different frequency, direction or state of polarization propagating simultaneously in the fiber. In Eq. 2.22, the first two terms correspond to pump induced SPM, while the last three terms correspond to XPM. To obtain Eqs. 2.22 and 2.23, the SPM and XPM terms induced by the *signal* and *idler* waves were neglected because in the majority of cases, their relatively low intensities are unable of self-producing such effects, thus their contribution can be neglected.

The four optical fields $\boldsymbol{E_j}$ evolve along the fiber length according to the Maxwell wave equation. For solving this equation, we set the z axis along the fiber axis and assume that the vector $\boldsymbol{E_j}$ lies in the (x, y) plane. This assumption entails that the longitudinal component of the fields are neglected. This assumption is applicable for fiber modes, for which the amplitude of the axial fields components are generally much smaller that the fields components in the transverse plane. To account for the polarization changes, we represent each field as a Jones vector and employ the bra and ket notation of [11]. More specifically, we write the four fields at any point **r** inside the fiber as

$$\mathbf{E}_j(r,t) = F_j(x,y)\left|A_j(z,t)\right\rangle e^{i\beta_j z} \qquad (2.24)$$

where $F_j(x, y)$ represents the fiber-mode profile, β_j is the propagation constant at the carrier frequency ω_j, and the Jones vector $\left|A_j\right\rangle$ is a two-dimensional column vector representing the envelope of the two components of the electric field in the (x, y) plane. In this notation, $\boldsymbol{E_j^*} \cdot \boldsymbol{E_j}$ is proportional to $\left\langle A_j \middle| A_j \right\rangle$ and $\boldsymbol{E_j} \cdot \boldsymbol{E_j}$ to $\left\langle A_j^* \middle| A_j \right\rangle$. The fiber mode profiles are assumed to be nearly the same for the four fields and can be related to the effective mode area A_{eff} through the relation:

$$A_{eff} = \frac{\left(\int_{-\infty}^{\infty}\int |F(x,y)|^2\, dx \cdot dy\right)^2}{\int_{-\infty}^{\infty}\int |F(x,y)|^4\, dx \cdot dy} \qquad (2.25)$$

Introducing Eqs. 2.22 – 2.24 into the Maxwell wave Eq. 2.13, integrating over the transverse-mode distribution in the (x, y) plane, and assuming $\left|A_j\right\rangle$ to be slowly varying functions of z so that we can neglect its second-order derivative with respect to z, we find that the two pump waves evolve as

$$\frac{d\left|A_j\right\rangle}{dz} = i\beta\left|A_j\right\rangle + \frac{i\gamma}{3}(2\left\langle A_j\middle|A_j\right\rangle + 2\left\langle A_m\middle|A_m\right\rangle + \left|A_j^*\right\rangle\left\langle A_j^*\right| + 2\left|A_m\right\rangle\left\langle A_m\right| + 2\left|A_m^*\right\rangle\left\langle A_m^*\right|)\left|A_j\right\rangle \tag{2.26}$$

where *j, m = 1, 2, (j ≠ m),* $\left\langle A\right|$ and $\left|A^*\right\rangle$ are the Hermitian and complex conjugates of $\left|A\right\rangle$, respectively. By using the same procedure, the *signal* and *idler* equations are given by,

$$\begin{aligned}\frac{d\left|A_j\right\rangle}{dz} = {} & i\beta_j\left|A_j\right\rangle + \frac{2i\gamma}{3}(\left\langle A_1\middle|A_1\right\rangle + \left\langle A_2\middle|A_2\right\rangle + \left|A_1\right\rangle\left\langle A_1\right| \\ & + \left|A_2\right\rangle\left\langle A_2\right| + \left|A_1^*\right\rangle\left\langle A_1^*\right| + \left|A_2^*\right\rangle\left\langle A_2^*\right|)\left|A_j\right\rangle \\ & + \frac{2i\gamma}{3}\left(\left\langle A_m\middle|A_1\right\rangle\left|A_2\right\rangle + \left\langle A_m\middle|A_2\right\rangle\left|A_1\right\rangle + \left\langle A_1^*\middle|A_2\right\rangle\left|A_m\right\rangle\right),\end{aligned} \tag{2.27}$$

where *j, m = 3, 4, (j ≠ m).* In the case of the degenerate FWM, Eq. 2.27 still represent the *signal* and *idler* evolution by replacing the amplitudes $\left|A_2\right\rangle \to \left|A_1\right\rangle$ and by setting the nonlinear terms to *γ/3*. In this case the equation describing the amplitude of the pump field is given by Eq. 2.26 by setting $\left|A_2\right\rangle = 0$.

In these equations, both the SPM and the XPM and, therefore, FWM are governed by the same nonlinear parameter *γ* defined as,

$$\gamma = \frac{3k_0\,\mathrm{Re}\left[\chi^{(3)}_{xxxx}\right]}{8n_{eff}A_{eff}} = \frac{n_2 \cdot k_0}{A_{eff}} \tag{2.28}$$

where k_0 is the wave vector at a wavelength λ, n_{eff} is the mode effective index. The parameter n_2 is known as the nonlinear refractive index, which is related to the modulation of the refractive index induced by intense electromagnetic field through the Kerr effect [5],

$$\tilde{n}(\omega,t) = n(\omega) + n_2(\omega)I(t) \tag{2.29}$$

In this work, in all the calculations for FWM gain and its parametric wavelengths, we have taken $n_2=2.7 \times 10^{-20}\ m^2W^{-1}$[7].

2.2.1 Scalar approximation

Eqs. 2.26 and 2.27 represent the most general case of vector FWM that can be supported in an optical fiber. So far, we have considered the vector nature of FWM, in which pump waves have arbitrary states of polarizations. However, and for the purpose of this thesis, we believe it is useful to provide an overview of FWM and its dependence on the fiber parameters in the framework of the scalar approximation.

In the scalar approximation, we assume that the polarization of the light is preserved in the FWM process. If we consider that the electric field has only one component which is polarized along the $\hat{x}$ axis (could be the fast or slow axis of a fiber), Eqs. 2.20 and 2.24 take their scalar forms and by introducing them into Eq. 2.23, one can derive the induced nonlinear polarization of FWM fields. In this case the induced polarization at the *signal* frequency, P_s is given by,

$$P_s = \frac{3\varepsilon_0}{4}\chi^{(3)}_{xxxx}\begin{bmatrix} |E_s|^2 E_s e^{i\beta_s z} + 2\left(|E_{p1}|^2 + |E_{p2}|^2 + |E_i|^2\right)E_s e^{i\beta_s z} \\ +2E_{p1}E_{p2}E_i e^{i\theta_+} + 2E_{p1}E_{p2}E_i^* e^{i\theta_-} + \ldots \end{bmatrix} \qquad (2.30)$$

where the phases θ_+ and θ_- are defined as:

$$\theta_+ = \left(\beta_1 + \beta_2 + \beta_s - \beta_i\right)z - \left(\omega_1 + \omega_2 + \omega_s - \omega_i\right)t \qquad (2.31)$$

$$\theta_- = \left(\beta_1 + \beta_2 - \beta_s - \beta_i\right)z - \left(\omega_1 + \omega_2 - \omega_s - \omega_i\right)t \qquad (2.32)$$

The last two terms in equation 2.30 are the result of the frequency combinations (sum or difference) of the four waves and, therefore, are responsible for the FWM effect. In Eqs. 2.31 and 2.32, the phase-mismatch between the electric field and polarization is given by θ_+ and θ_-, and it determines the efficiency of FWM

process. When the phase-mismatch vanishes the FWM contribution becomes more relevant. The latter requires both the matching of the four frequencies and the wave vectors involved, such requirement is often call as phase-matching condition. The phase-matching condition requires a specific choice of input wavelengths and fiber parameters before FWM can occur with high efficiency. In the next section, we will explore the relevance of the phase-matching condition for FWM frequencies as a function of fiber parameters and pump properties.

Two types of FWM processes can be classified from Eq. 2.30 The term containing θ_+ corresponds to the case in which three photons transfer their energy to a single photon at the frequency $\omega_4 = \omega_1 + \omega_2 + \omega_3$, this process is named as third-harmonic generation (THG). In general, the phase matching condition of THG is hard to be efficiently fulfilled in optical fibers, therefore, this process presents really low efficiency and can be neglected in the most of the cases. On the other hand, the term containing θ_- correspond to the case in which two photons at frequencies ω_1 (ω_{p1}) and ω_2 (ω_{p2}) transfer their energy to give rise to two photons at different frequencies ω_3 (ω_s) and $\omega_4(\omega_i)$. This process is commonly known as scalar FWM. In the degenerate case of FWM, the new frequencies are located symmetrically at each side of the pump with a frequency shift,

$$\omega_p - \omega_i = \omega_s - \omega_p \tag{2.33}$$

being ω_p, ω_i, and ω_s the pump, *idler* and *signal* frequencies, respectively. As mentioned above, FWM also requires the matching of the wave vectors, which is given by,

$$\Delta k = 2\beta_p - \beta_s - \beta_i = 0 \tag{2.34}$$

where β_p, β_i, and β_s are the propagation factors of the pump, *idler* and *signal* waves, respectively. Eq. 2.34 is also known as the linear phase-mismatch and accounts for the contribution of fiber dispersion in an FWM process.

To derive the coupled amplitude equations describing the scalar approximation of FWM in the nondegenerate case, we follow the same procedure as done to derive Eqs. 2.26 and 2.27. The total electric field and the induced polarization are introduced in the Maxwell wave equation (considering the scalar approximation). We assume the same spatial field distribution of the four waves and their time dependence is neglected (CW approximation). By considering the fiber as single-mode at all frequencies and, the overlap integrals of the mode profiles to be almost equal (same effective mode area), the evolution of the amplitude of the different waves within an optical fiber is governed by the following set of four coupled equations. The amplitude of the pump waves, A_{pj} is given by,

$$\frac{dA_{pj}}{dz} = i\left(\beta_{pj} + \gamma\left(P_j + 2P_m\right)\right)A_{pj} \qquad (2.35)$$

where $j, m = 1, 2$ (with $j \neq m$), and $P_j = |A_j(0)|^2$ is the input pump powers at $z=0$. Eq 2.35 can be directly integrated, giving the following,

$$A_{pj}(z) = \sqrt{P_j}\, e^{i\left(\beta_j + \gamma\left(P_j + 2P_m\right)\right)z} \qquad (2.36)$$

This solution shows that, in the undepleted-pump approximation, the pump waves only acquire a phase shift occurring as a result of SPM and XPM. Following the same procedure, we can obtain the differential equations that rule the *signal* and *idler* amplitudes,

$$\frac{dA_j}{dz} = 2i\gamma\left[\left(P_1 + P_2\right)A_j + \sqrt{P_1 P_2}\, e^{i\phi z} A_m^*\right] \qquad (2.37)$$

where $j, m = s$ or i ($j \neq m$) and $\phi = \Delta k + 3\gamma\left(P_1 + P_2\right)$. To solve these equations, we introduce an auxiliary field amplitude $A_j = e^{2i\gamma(P_1+P_2)z} B_j$ into Eq. 2.37, to obtain,

$$\frac{dB_j}{dz} = 2i\gamma\sqrt{P_1P_2}e^{i\kappa z}B_m^* \qquad (2.38)$$

Notice that B_s depends on B_i^* and vice versa. Thus, the *idler* should be a phase conjugated version of the *signal*, if the pump phases remain relatively constant during the FWM process. The parameter κ is known as the net phase-mismatch and it is given by

$$\kappa = \beta_{p1} + \beta_{p2} - \beta_s - \beta_i - \gamma\left(P_1 + P_2\right) \qquad (2.39)$$

The last term in Eq. 2.39, i. e. the nonlinear phase-mismatch contribution, is a phase shift resulting from the SPM and XPM induced by the pump as it propagates through the fiber.

To obtain the solution of Eqs. 2.38, we can manipulate them to obtain two uncoupled second-order differential equations as follows,

$$\frac{d^2B_s}{dz^2} + i\kappa\frac{dB_s}{dz} - \left(4\gamma P_1P_2\right)B_s = 0 \qquad (2.40)$$

where $j = s, i$. The general solution for B_s and B_i is given by,

$$B_s\left(z\right) = \left(a_se^{gz} + b_se^{-gz}\right)\cdot e^{-i\kappa z/2} \qquad (2.41)$$

$$B_i^*\left(z\right) = \left(a_ie^{gz} + b_ie^{-gz}\right)\cdot e^{i\kappa z/2} \qquad (2.42)$$

where the constants a_j and b_j (j= *s, i*) are determined from the boundary conditions. The parameter g that has been introduced in Eqs. 2.41 and 2.42 represent the gain of the process. The gain depends on the total pump power P ($P=P_1 + P_2$) and on the net phase-mismatch as follows [12],

$$g = \sqrt{\left(\gamma P\right)^2 - \left(\kappa/2\right)^2} \qquad (2.43)$$

From Eq. 2.43 we can deduce that significant FWM can occur when κ tends to zero, so the fulfillment of the phase-match condition ($\kappa \rightarrow 0$) implies an efficient FWM process with peak gain equal to γP.

2.2.2 Vector FWM

In this section we will derive the net phase-mismatch equations for specific cases of vector FWM considering a linearly polarized pump source. We also study the dependence of the FWM frequency shift on the phase birefringence in a weak birefringent fiber. In particular, we focus this theoretical study on two specific vector cases, which describe the nonlinear effect of PMI. For the purpose of this work, we address the derivation of the parametric gain along with the main theoretical aspects of such a nonlinear effect.

In anisotropic materials, the refractive index depends on the polarization and propagation direction of incident light. These optically anisotropic materials are said to be birefringent. Optical fibers including microstructured optical fibers are, in general, birefringent media. Some fibers are designed to exhibit large birefringence, but even fibers that are designed to be isotropic, exhibit a certain degree of birefringence, known as residual birefringence, whose origin is related to geometrical anisotropy and/or internal-stress fields formed during the fabrication stage [13].

Birefringence breaks the polarization degeneracy of the fundamental fiber mode that exists in perfectly cylindrical isotropic optical fibers. Therefore, in birefringent single-mode fibers, two eigenmodes with different propagation factor and orthogonal polarization can propagate, called fast mode and slow mode according to their relative propagation velocities. Thus, this establishes two preferred optical axes of an optical fiber, the fast axis being the axis that coincides with the polarization orientation of the faster propagating mode, and the slow axis

being the axis of the fiber that coincides with the polarization of the slow mode. When the pump polarization is not aligned to any of the principal axes of the fiber, the state of polarization will change as the beam propagates along the fiber. In the case of a single-mode fiber, this is related to the different evolution of the two polarizations of the fundamental mode, which is quantified through the modal birefringence Δn,

$$\Delta n = n_S - n_F = \frac{\lambda}{2\pi}(\beta_S - \beta_F)\frac{\lambda}{2\pi}\Delta\beta \qquad (2.44)$$

where n_S, n_F, β_S and β_F are the effective indices of the modes with polarization oriented to the slow and fast axis, respectively. For convenience, we will consider a reference system with x-axis oriented to the fast fiber axis and y-axis oriented with the slow fiber axes, so that $\beta_F \equiv \beta_x$ and $\beta_S \equiv \beta_y$.

When considering a linearly polarized pump source, there are two possible cases in which the generated FWM sidebands can be polarized, i.e. sidebands that are co-polarized and sidebands that are orthogonally polarized. This results when the pump polarization coincides with one or both of the fiber axes. Fig. 2.4 shows the schematic of the two types of polarized FWM sidebands. However, it will be shown later that co-polarized pumps exciting one eigenmode of a fiber can produce two FWM sidebands with polarization orientation orthogonal to the pump polarization. The latter case is included in Fig. 2.4 and shows the dependence of FWM on the orientation of the polarization of the pump fields with respect to the principal axes of an optical fiber, and points out the relevance of the fiber birefringence.

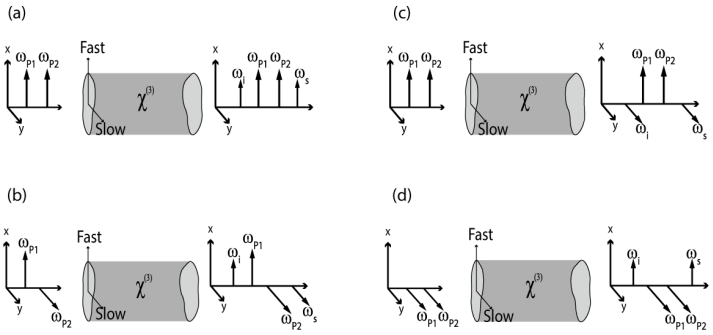

Figure 2.4. Schematic of the polarization orientations of the FWM sidebands produced in a birefringent fiber with linearly polarized pump. FWM sidebands can be (a) co-polarized, (b) co-polarized as orthogonally polarized and (c and d) orthogonally polarized with respect to the pump fields.

To study vector FWM, we can start by assuming that the fiber is isotropic, hence it is non-birefringent. The latter assumption supports the description of the possible vector FWM cases that can occur in a realistic optical fiber of a short length (*L ~ 1m*), in which the birefringence of a fiber can be considered independent of the length itself [9]. However, to obtain a complete picture of the dependence of FWM on the birefringence of a fiber, one must include the change of the state of polarization (SOP) of the pump, *signal* and *idler* fields induced by random changes of the residual birefringence along the length of the fiber. For FWM applications with long interaction lengths, e.g., FOPAs with operating lengths of L ~ 0.5 km, the random birefringence of the fiber along with the nonlinear polarization rotation (NPR) [7] must be considered, since such effects are responsible for modifying the SOPs of the four fields, hence the phase matching condition of the FWM is also modified. Under this condition, the coupled amplitude equations describing the evolution of the pump and FWM fields must be considered as stochastic system [14,15]. Since the experiments carried out along this thesis, the length of the employed fibers is relatively short (*L ~ 1 m*), therefore, NPR effect can be neglected. Furthermore, we assume that the SOPs of the four fields are preserved during the

FWM process. The residual fiber birefringence is taken into account by introducing a phase shift of the pump fields. The starting point is Eq. 2.26 which describes the evolution of the pump fields including their states of polarization, under undepleted-pump approximation.

$$\frac{d\left|A_j\right\rangle}{dz} = i\beta\left|A_j\right\rangle + \frac{i\gamma}{3}(2\left\langle A_j\right|\left.A_j\right\rangle + 2\left\langle A_m\right|\left.A_m\right\rangle + \left|A_j^*\right\rangle\left\langle A_j^*\right| + 2\left|A_m\right\rangle\left\langle A_m\right| + 2\left|A_m^*\right\rangle\left\langle A_m^*\right|)\left|A_j\right\rangle \tag{2.45}$$

For our purpose, we solve Eq. 2.45 considering the case of linearly co-polarized pumps and assuming that the orientation of the pump polarization with respect to a fiber axis is quantified by an angle θ. Fig. 2.5 shows the reference system taken to solve Eq. 2.45, for simplicity we consider the fiber axes in cartesian coordinates.

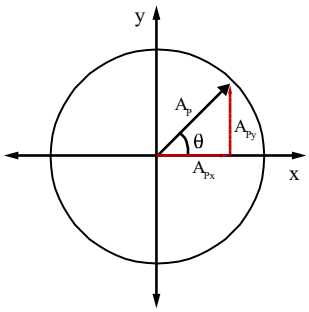

Figure 2.5. Schematic of the reference system.

Thus, the solution of Eq. 2.45 is given by,

$$\left|A_j\right\rangle(z) = \sqrt{P_j}\begin{pmatrix} \cos\theta e^{i\left(\beta_j + \frac{2}{3}\gamma_x\left(P_{jx}+2P_{mx}\right)\right)z} \\ \sin\theta e^{i\left(\beta_j + \frac{2}{3}\gamma_y\left(P_{jy}+2P_{my}\right)\right)z} \end{pmatrix} \tag{2.46}$$

where $j, m = 1, 2$ (with $j \neq m$) and $\left\langle A_j\right|\left.A_j\right\rangle = P_j$. The coefficients γ_x and γ_y are the nonlinear coefficient of the two polarization modes. In order not to lose generality

in the result, we have considered the possibility that eventually they could be different. In optical fibers, particularly in highly birefringent, it might happen that the two polarization modes exhibit slightly different effective area, which might lead to such nonlinear birefringence.

Similar to the scalar approximation of the FWM (see Equation 2.36), the pump fields acquire a nonlinear phase shift induced by SPM and XPM effects. To account for fiber birefringence, we assume that the pump field components propagate at different velocities, resulting in a phase shift. Under this condition, we can introduce the phase birefringence, thus Eq 2.46 can be rewritten as follows.

$$\left|A_j\right\rangle(z) = e^{i\left(\beta_{jx}+\frac{2}{3}\gamma_x\left(P_{jx}+2P_{mx}\right)\right)z}\begin{pmatrix}\sqrt{P_{jx}}\cos\theta \\ \sqrt{P_{jx}}\sin\theta e^{i\delta_j}\end{pmatrix} \tag{2.47}$$

where parameter δ_j is given by,

$$\delta_j = \left[\left(\beta_{jy}-\beta_{jx}\right)+\frac{2}{3}\left(\gamma_y-\gamma_x\right)\left(P_j+2P_m\right)\right]z \tag{2.48}$$

Equations 2.47 and 2.48 indicate that there is indeed a phase shift between the pump field components, which includes a contribution due to modal birefringence and a second contribution due to the birefringence of the nonlinear coefficient. In a perfectly isotropic fiber both contributions vanish because the pump field components have the same propagation factor and effective area.

To obtain the *signal* and *idler* waves, we introduce the solution 2.47 into Eq. 2.27 to obtain the coupled equations that describes the evolution of the fields at the *signal* and *idler* frequencies,

$$\frac{d\left|A_j\right\rangle}{dz} = i\left(\beta_j + M_0\right)\left|A_j\right\rangle + e^{i\left(\beta_1+\beta_2+2\gamma_x\left(P_1+P_2\right)\right)z}M_1\left|A_m^*\right\rangle \tag{2.49}$$

where *j, m = s, i (*with *j ≠ m)* and M_0 and M_1 are two *2x2* matrices defined as,

$$M_0 = \frac{2}{3}\gamma_x \begin{pmatrix} \sigma_+ & \sigma \\ \sigma & \sigma_- \end{pmatrix} \tag{2.50}$$

$$M_1 = \frac{2}{3}\gamma_x \begin{pmatrix} \varphi_+ & \varphi \\ \varphi & \varphi_- \end{pmatrix} \tag{2.51}$$

where the different matrix coefficients are given by,

$$\begin{aligned} \sigma_+ &= 3P_{xx}\cos^2\theta + P_{yy}\sin^2\theta \\ \sigma_- &= P_{xx}\cos^2\theta + 3P_{yy}\sin^2\theta \\ \sigma &= 2\left(\sqrt{P_{1x}P_{1y}}\cos\delta_1 + \sqrt{P_{2x}P_{2y}}\cos\delta_2\right)\sin\theta\cos\theta \end{aligned} \tag{2.52}$$

$$\begin{aligned} \varphi_+ &= 3\sqrt{P_{1x}P_{2x}}\cos^2\theta + \sqrt{P_{1y}P_{2y}}\sin^2\theta e^{i(\delta_1+\delta_2)} \\ \varphi_- &= \sqrt{P_{1x}P_{2x}}\cos^2\theta + 3\sqrt{P_{1y}P_{2y}}\sin^2\theta e^{i(\delta_1+\delta_2)} \\ \varphi &= \left(\sqrt{P_{1x}P_{2y}}e^{i\delta_2} + \sqrt{P_{1y}P_{2x}}e^{i\delta_1}\right)\sin\theta\cos\theta \end{aligned} \tag{2.53}$$

where $P_{xx}=P_{1x} + P_{2x}$, $P_{yy}= P_{1y} + P_{2y}$ and represent the total pump power carried by each eigenmode. The matrix M_0 arises from the effects of SPM and XPM given by the first six nonlinear terms of Eq. 2.27. In order to solve Eq. 2.49, we introduce $\left|A_j\right\rangle = e^{i(\beta_j + M_0)z}\left|B_j\right\rangle$ and $\left|A_m^*\right\rangle = e^{-i\left(\beta_m + M_0^*\right)Z}\left|B_m\right\rangle$, thus Eq 2.49 can be rewritten as follows.

$$\frac{d\left|B_j\right\rangle}{dz} = e^{i\kappa z}M_2\left|B_m^*\right\rangle, \tag{2.54}$$

where the matrix M_2 is defined as,

$$M_2 = ie^{iM_0^* z}M_1 e^{iM_0^* z} \tag{2.55}$$

and κ is the net phase-mismatch given by,

$$\kappa = \beta_{p1} + \beta_{p2} - \beta_s - \beta_i - 2\gamma_x\left(P_1 + P_2\right) - \left(M_0 + M_0^*\right) \tag{2.56}$$

Equation 2.54 can be solved similarly as it was done for Eq. 2.38. For the present work, we have paid special attention to the phase-matching condition related

to each vector process of FWM that can occur in a weakly birefringent fiber. The coefficients of the matrix M_0 describe the polarization state with which the *signal* and *idler* bands are generated in a FWM process. We can identify six different processes that can take place. From the matrix coefficient σ_+, we identify the process in which the *x*-component of the pump fields produces *signal* and *idler* bands with polarization in *x* direction (we call this *xx-xx* in the same manner as scalar FWM) and the process in which the *y*-component of the pump fields produce FWM bands with polarization in *x* direction (*yy-xx*). Using this same notation, we describe the rest of the processes. Matrix coefficient σ is symmetric and yield the processes *xy-yx* and *xy-xy*. Finally, from matrix coefficient σ_- we identify the processes *yy-yy* and *xx-yy*. For a clear view, we have depicted each process in Fig. 2.6 by considering the above polarization orientations of the pump fields.

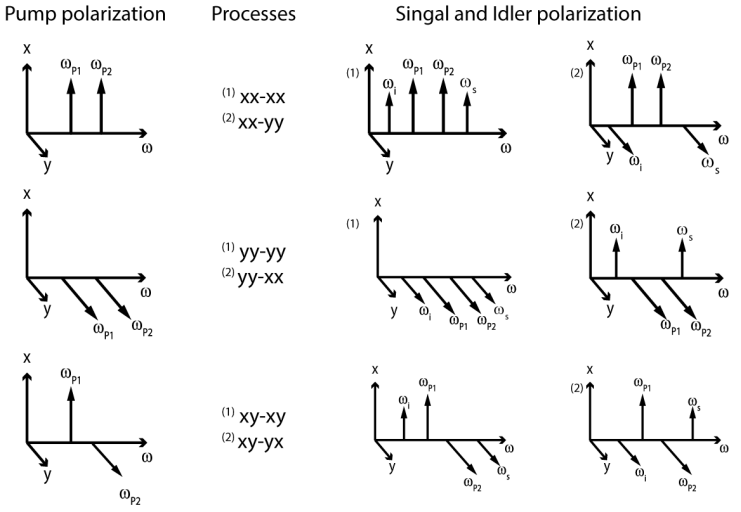

Figure 2.6. Schematic representation of the polarization orientation of each FWM vector process supported by an optical fiber.

By inspection of matrix M_0, using Eq. 2.56 and considering co-polarized pump fields, we can derive the net phase-mismatch for each vector case of FWM as a function of the angle θ,

$$\kappa_{xx-xx} = \beta_{p1x} + \beta_{p2x} - \beta_{sx} - \beta_{ix} - 2\gamma_x (P_1 + P_2)\left(2\cos^2\theta - 1\right) \quad (2.57)$$

$$\kappa_{xx-yy} = \beta_{p1x} + \beta_{p2x} - \beta_{sy} - \beta_{iy} - 2\gamma_x (P_1 + P_2)\left(\frac{2}{3}\cos^2\theta - 1\right) \quad (2.58)$$

$$\kappa_{yy-yy} = \beta_{p1y} + \beta_{p2y} - \beta_{sy} - \beta_{iy} - 2\gamma_x (P_1 + P_2)\left(2\sin^2\theta - 1\right) \quad (2.59)$$

$$\kappa_{yy-xx} = \beta_{p1y} + \beta_{p2y} - \beta_{sx} - \beta_{ix} - 2\gamma_x (P_1 + P_2)\left(\frac{2}{3}\sin^2\theta - 1\right) \quad (2.60)$$

$$\kappa_{xy-xy} = \beta_{p1x} + \beta_{p2y} - \beta_{sx} - \beta_{iy} - 2\gamma_x (P_1 + P_2)\left(\frac{2}{3}\sin\theta\cos\theta - 1\right) \quad (2.61)$$

$$\kappa_{xy-yx} = \beta_{p1x} + \beta_{p2y} - \beta_{sy} - \beta_{ix} - 2\gamma_x (P_1 + P_2)\left(\frac{2}{3}\sin\theta\cos\theta - 1\right) \quad (2.62)$$

For each vector case, the frequencies for the *signal* and *idler* bands can be obtained by solving $\kappa = 0$ (phase-matching condition). Equations 2.57-2.62 state that the phase matching condition and hence the frequency shift of the *signal* and *idler* photons depends on: (1) the pump conditions, i.e., the power and orientation of the polarization with respect to the fiber axis, (2) on the dispersion, (3) on the birefringence of the fiber, and (4) on the nonlinear coefficient.

So far, we have derived the coupled amplitude equations describing the evolution of the fields responsible for the FWM produced in a weakly birefringent fiber. In addition, we have derived the phase-matching equations when considering linearly polarized pump fields with arbitrary polarization orientation with respect to the fiber axes. The theoretical procedure presented in this section can be also applied for describing the FWM generated in a fiber with moderate to high modal

birefringence ($\Delta n > 10^{-5}$). In our model we assume that the SOPs of the four interacting fields are preserved during the FWM processes, which can indeed occur in a highly birefringent fiber. However, some assumptions must be included, e.g., to derive the coupled amplitude equations at the *signal* and *idler* band frequencies, the effect of fiber birefringence cannot be treated as a phase shift, since the coherent coupling between the pump fields due to SPM and XPM effects averages to zero during a FWM process, even for short fiber lengths [16]. In that case, the net phase mismatch can be derived by setting $M_0=0$. However, highly birefringent fibers are beyond the scope of this thesis, since most of the experiments were performed on weakly birefringent fibers $\Delta n \sim 10^{-6}$.

2.2.3 A particular case: FWM produced by slow/fast pumping

For the purposes of the present work, we are particularly interested in the case of degenerate FWM produced when the pump polarization matches one of the main axes of the fiber (slow or fast axis). Hence, in this section we derive the phase-matching equations for these particular cases. For convenience, to solve the pump amplitude equations, we set the reference frame as in Fig. 2.5. We assume that the *x*-and y-axes correspond to the fast (*F*) and slow axes (S) of the fiber, respectively. In the case that the pump orientation is aligned with the fast fiber axis (i.e., $\theta = 0$), the matrix M_0 takes the form,

$$M_0 = \frac{2}{3}\gamma \begin{pmatrix} 3P_0 & 0 \\ 0 & P_0 \end{pmatrix} \qquad (2.63)$$

and when the pump is polarized along the slow fiber axis ($\theta = \pi/2$) we find,

$$M_0 = \frac{2}{3}\gamma \begin{pmatrix} P_0 & 0 \\ 0 & 3P_0 \end{pmatrix} \qquad (2.64)$$

For degenerate FWM with pump polarization oriented to one principal axis of the fiber, we find four different vector processes. The net phase-mismatch for *S* or *F* axis pumping takes the form,

$$\kappa_{F-F} = 2\beta_p - \beta_s - \beta_i - 2\gamma P_0 \qquad (2.65)$$

$$\kappa_{F-S} = 2\beta_p - \beta_s - \beta_i - \frac{(\omega_s + \omega_i)}{c}\Delta n + \frac{2}{3}\gamma P_0 \qquad (2.66)$$

$$\kappa_{S-S} = 2\beta_p - \beta_s - \beta_i - 2\gamma P_0 \qquad (2.67)$$

$$\kappa_{S-F} = 2\beta_p - \beta_s - \beta_i + \frac{(\omega_s + \omega_i)}{c}\Delta n + \frac{2}{3}\gamma P_0 \qquad (2.68)$$

where the labels *F-F, F-S*, *S-S* and *S-F* represent the orientation of the pump polarization (first label) and polarization orientation of the FWM sidebands (second label). In Eqs. 2.66 and 2.68, we have introduced the fiber birefringence $\Delta n = n_y - n_x$. Notice that Eqs. 2.65 and 2.67 are identical to Eq. 2.39, which describes the net phase-mismatch of the scalar case of FWM. In weakly birefringent fibers, the phase-matching occurs at nearly the same frequencies for these two vector cases of FWM, so the vector nature of FWM can, in a first-order approximation, be neglected for these two particular cases. However, for moderate to high birefringence fibers, this does not apply and the vector description of the FWM (for both slow and fast axis pumping) is necessary.

Equations 2.66 and 2.68 describe the phase-matching condition of the nonlinear effect known as PMI [7]. Such nonlinear effect is investigated extensively in this work and detailed information will be given in chapter 4. In the following, the main theoretical aspects of PMI will be outlined. The polarization instability manifests as large changes in the output SOP when the input power or the input SOP of a CW beam is changed slightly [17–19]. The origin of polarization instability can be understood from the following qualitative argument [17]. When the input beam is polarized close to the slow axis, nonlinear birefringence adds to intrinsic

linear birefringence, making the fiber more birefringent. By contrast, when the input beam is polarized close to the fast axis, nonlinear effects decrease the net birefringence by an amount that depends on the input power. As a result, the fiber becomes less birefringent, and the effective beat length L_B^{eff} increases. At a critical value of the input power, nonlinear birefringence cancels the linear birefringence completely, and L_B^{eff} becomes infinite. With a further increase in the input power, the fiber again becomes birefringent but the roles of the slow and fast axes are reversed. Clearly large changes in the output polarization state can occur when the input power is close to the critical power required to balance the linear and nonlinear birefringence. The critical power is also known as the threshold power for polarization instabilities to occur and is given by [7],

$$P_{th} = \frac{3}{2}\frac{\Delta n \cdot A_{eff}}{n_2} \qquad (2.69)$$

Polarization modulation instability occurs in single-mode fibers with low birefringence and arises from coherent coupling between the two polarized components of the fundamental mode, where mode coupling is attributed to the XPM effect. PMI is responsible for the destabilization of the CW state when a beam propagates within a fiber. Therefore, PMI is somehow analogous to the scalar case of modulation instability (MI) which refers to the same process, but induced by SPM when light experiences anomalous GVD ($\beta_2 < 0$) within the fiber. In contrast, PMI occurs even in the region of normal GVD ($\beta_2 > 0$) while MI is forbidden.

As stated previously, PMI is a particular case of vector FWM, which can occur when polarized light excites one of the two polarization eigenmodes (fast or slow fiber mode) of a low birefringence optical fiber. As a result, two equally spaced sidebands with orthogonal polarization with respect to the pump polarization are generated. PMI photons are generated one with higher energy and one with lower energy and are often referred to as anti-Stokes and Stokes photons, respectively. The

phase matching equations derived in Eqs. 2.66 and 2.68 describes in a proper manner the effect of PMI when the fiber is excited by either fast-axis pumping (Eq. 2.66) or slow-axis pumping (Eq. 2.68).

To give a physical insight between the PMI effect and the fiber parameters, we followed the theoretical description from [7]. In it, a phenomenological approach was used to describe the polarization instability of an optical pulse produced in a weakly birefringent fiber. In this model, under the conditions of degenerate PMI, a set of coupled amplitude equations was derived for describing the propagation of a short optical pulse propagating inside the fiber, this equation is also known as coupled nonlinear Schrodinger equation (CNLSE). The pulse propagation equations are given by,

$$\frac{\partial A_{\pm}}{\partial z}+\beta_1\frac{\partial A_{\pm}}{\partial t}+\frac{i\beta_2}{2}\frac{\partial^2 A_{\pm}}{\partial t^2}+\frac{\alpha}{2}A_{\pm}=\frac{i\Delta\beta}{2}A_{\mp}+\frac{2i\gamma}{3}\left(\left|A_{\pm}\right|^2+2\left|A_{\mp}\right|^2\right)A_{\pm} \qquad (2.70)$$

where α are the fiber losses, A_+ and A_- are the slow varying envelope components of the electromagnetic field for right and left circularly polarized states, respectively. Circularly polarized frame was used to simplify pulse equation in cartesian coordinates. The circularly polarized components are defined as,

$$A_+=\left(A_x+iA_y\right)/\sqrt{2}, \qquad A_-=\left(A_x-iA_y\right)/\sqrt{2} \qquad (2.71)$$

In order to solve Eq. 2.70, first we neglected the time dependence of the optical pulse at $\tau=0$ (CW condition), we also assume a lossless fiber ($\alpha=0$) and the input SOP is oriented to one principal axis of the fiber, which stand for PMI produced by slow or fast axis pump. In the first case, by setting $A_x = 0$ the solution is given by,

$$A_{\pm}=\pm i\sqrt{P_0/2}\exp\left(i\gamma P_0 z\right) \qquad (2.72)$$

Eq. 2.72 represents the steady-state solution, in which the pulse only acquires a nonlinear phase shift similar to that in Eq. 2.36 describing the pump fields in the

scalar approximation of FWM. In order to introduce the modulation instability effect, we add a small perturbation to the steady state condition of the pulse as,

$$A_{\pm} = \pm\left[i\sqrt{P_0 / 2} + a_{\pm}(z,t) \right] \exp\left(i\gamma P_0 z\right) \qquad (2.73)$$

where $a_{\pm}(z,t)$ is a small perturbation. By substituting Eq. 2.73 into Eq.2.70 and linearizing in $a_{\pm}$ we obtained a set of two coupled linear equations with solutions of the form,

$$a_{\pm} = u_{\pm} \exp\left[i(\mathrm{K}z - \Phi t)\right] + iv_{\pm} \exp\left[-i(Kz - \Phi t)\right] \qquad (2.74)$$

where Φ is the frequency (detuning frequency) of the perturbation and K is the wavenumber related to the phase-matching of PMI. The terms $u_{\pm}$ and $v_{\pm}$ are related to the envelope of the sidebands produced by PMI. Solving for $u_{\pm}$ and $v_{\pm}$ we obtain a set of four algebraic equations with nontrivial solution only when the perturbation satisfies the dispersion relation [19],

$$\left[(\mathrm{K} - \beta_1\Phi)^2 - C_1\right]\left[(\mathrm{K} - \beta_1\Phi)^2 - C_2\right] = 0 \qquad (2.75)$$

where C_1 and C_2 are defined as,

$$C_1 = \frac{1}{2}\beta_2\Phi^2\left(\frac{1}{2}\beta_2\Phi^2 + 2\gamma P_0\right) \qquad (2.76)$$

$$C_1 = \left(\frac{1}{2}\beta_2\Phi^2 + \Delta\beta - \frac{2}{3}\gamma P_0\right)\left(\frac{1}{2}\beta_2\Phi^2 + \Delta\beta\right) \qquad (2.77)$$

The steady-state solution becomes unstable if $K(\Phi)$ has an imaginary part for certain values of Φ, indicating that the PMI sidebands at that frequency would grow exponentially along the fiber with the gain $g=2Im(K)$. The nature of PMI depends strongly on whether the pump power is below or above the power threshold. For $P_0<P_{th}$ the pulse remains stable, therefore PMI cannot be produced within the fiber. However, one can observed from Eq. 2.75 that PMI can occur even in the normal

dispersion regime *(β>0)* provided by $C_2<0$. This condition is satisfied in the range of frequencies from $0 < |\Phi| < \Phi_{c1}$, where,

$$\Phi_{c1} = \left(\frac{4\gamma}{3\beta_2}\right)^{\frac{1}{2}} \sqrt{P_0 - P_{th}}, \qquad (2.78)$$

the latter condition implies that modulation instability can occur in the normal dispersion regime only when $P_0>P_{th}$. In such case, the gain of PMI is given by,

$$g_{F-S}(\Phi) = |\beta_2| \sqrt{\left(\Phi^2 - \Phi_{c2}^2\right)\left(\Phi_{c1}^2 - \Phi^2\right)}, \qquad (2.79)$$

where Φ_{c2} is the frequency limit and is defined as

$$\Phi_{c2} = \left(\frac{2\Delta\beta}{\beta_2}\right)^{\frac{1}{2}}. \qquad (2.80)$$

Eq. 2.79 describes the PMI gain produced when the polarization of the pump is oriented to the fiber fast axis, thus PMI sidebands are polarized along the slow-axis. To derive the expression for the PMI gain produced by slow-axis pumping, we set $Ay = 0$ and by following the procedure described above we can derive the PMI gain which is given by,

$$g_{S-F}(\Phi) = |\beta_2| \sqrt{\left(\Phi^2 - \Phi_{c2}^2\right)\left(\Phi_{c3}^2 - \Phi^2\right)}, \qquad (2.81)$$

for this particular case, PMI can occur in a frequency range from $0 < |\Phi| < \Phi_{c3}$, where the critical frequency Φ_{c3} is defined as,

$$\Phi_{c3} = \left(\frac{4\gamma}{3\beta_2}\right)^{\frac{1}{2}} \sqrt{P_0 + P_{th}}, \qquad (2.82)$$

notice from Eq. 2.82 that S-F PMI can occur even for $P_0<P_{th}$ in the normal dispersion regime.

2.3 Numerical analysis of FWM and PMI

In this section, we investigate numerically the main features of the different cases of vector degenerate FWM discussed in section 2.2.3 in a low-birefringence, single-mode microstructured optical fiber. As shown earlier, when the pump wave is linearly polarized with polarization orientation matching one of the principal axes the fiber, four different interactions involving different polarization states are possible, two of them with characteristics very similar to the scalar FWM case (hereinafter referred to as FWM) and two interactions corresponding to PMI. We investigate the characteristics of FWM/PMI process in MOFs. We pay special attention to the dependence of the spectral shift of the generated sidebands as a function of the different parameters involved in the process, and that includes the fiber properties, and the pump characteristics.

By inspection, from the net phase mismatch of FWM/PMI given by Eqs. 2.65-2.68, it can be seen that both effects show an explicit dependency on two optical properties of the fundamental fiber mode, that is the nonlinear coefficient and the mode dispersion, which determine the linear $(\Delta\kappa_L)$ and nonlinear $(\Delta\kappa_{NL})$ contribution to the phase-matching condition. Additionally, PMI also exhibits a strong dependency on the fiber birefringence. In comparison, FWM is almost insensitive to such parameter in weakly-birefringent fibers.

First, the parametric wavelengths were calculated by numerically solving the phase-matching equations and considering the energy conservation of the photons involved. For the calculations, we considered the optical properties of the light source used in the experiments of this thesis, which is described in detail in Chapter 3. We performed all the FWM/PMI simulations for a representative MOF. The analyzed fiber is a solid-core MOF with a microstructure of air holes arranged in a triangular lattice. The inset in Fig 2.7 (a) shows a scheme of the transverse section

of the fiber. Its structural parameters are: $\Lambda = 3.53\ \mu m;\ d/\Lambda = 0.40$. It is assumed that the fiber exhibits a phase birefringence $\Delta n = 10^{-6}$. We employed a software called "Itera" to obtain the linear optical characteristics of the MOF. These are the mode propagation factor, the group refractive index, and the modal field diameter. The theoretical model on which Itera is based is described in detail in Chapter 3. Fig. 2.7 shows the chromatic dispersion of the fiber under test (FUT) as a function of optical wavelength. Within the wavelength range analyzed, chromatic dispersion shows a zero-dispersion wavelength at 1.08 μm, with normal (anomalous) dispersion for wavelengths below (above) λ_{ZDW}, respectively.

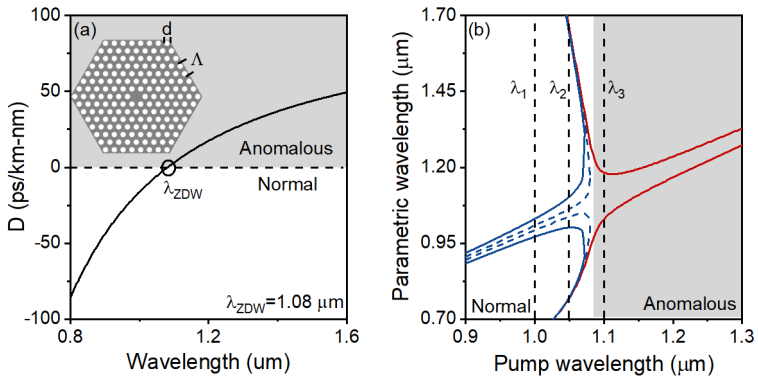

Figure 2.7. (a) MOF Chromatic dispersion of the fundamental mode as a function of wavelength. The inset shows the transverse profile of the MOF. (b) Parametric wavelengths produced by PMI (blue) and FWM (red) for slow and fast axis pumping. $\Delta n = 10^{-6}$; $P_0 = 2.5$ *kW*; $n_2 = 2.7 \times 10^{-20}\ m^2W^{-1}$. The dashed blue line indicates PMI with pumping in the fast axis and the solid blue line indicates PMI with pumping in the slow axis. Vertical dashed lines indicate three pump wavelengths representative of the different dispersion regimes.

The parametric wavelengths generated by FWM/ PMI were obtained after solving Eqs. 2.65-2.68 for this fiber. The result as a function of the pump wavelength is shown in Fig. 2.7(b). For each type of nonlinear interaction, we find either no solutions or two solutions depending on the pump wavelength. Thus, we can differentiate different regimes. When the fiber dispersion at the pump wavelength,

λ_p, is normal and the pump wavelength is relatively far from the λ_{ZDW}, so that the dispersion value is moderate to high (for example, $\lambda_p = \lambda_1$ in Fig. 2.7(b)), only solutions for PMI are found. Oppositely, when the fiber dispersion at the pump wavelength is anomalous (for example, $\lambda_p = \lambda_3$ in Fig. 2.7(b)), no solutions for PMI are found and only FWM effect is feasible. A more complex behavior is found when the dispersion of the fiber is normal and λ_p approaches λ_{ZDW}, so that the fiber dispersion is small at λ_p (for example, $\lambda_p = \lambda_2$ in Fig. 2.7(b)). In this case, both FWM and PMI can be generated simultaneously. Furthermore, in this regime, a couple of additional solutions are found for PMI at longer and shorter wavelengths, close to the parametric wavelengths found for FWM.

In Fig. 2.7 (b) it can be observed that the detuning of PMI wavelengths increases with λ_p for the inner pair of solutions and decreases for the outer pair of solutions. In the case of FWM wavelengths, the detuning decreases with the pump wavelength. Additionally, for certain pump wavelengths near to the λ_{ZDW} no solutions of PMI are found even though the fiber dispersion is normal, which indicates that PMI exhibit a cutoff which is related to the critic frequencies derived in Eqs. 2.80 and 2.82. For this fiber in particular, PMI cutoff occurs at 1.070 μm and 1.078 μm for slow-axis and fast-axis pump, respectively.

In the following, we quantify the FWM/PMI response and its gain in terms of the detuning frequency between the pump wavelength and the parametric wavelengths. For convenience, we introduce the frequency shift by means of its reciprocal spatial frequency Ω, which can be expressed as,

$$\Omega = \frac{1}{\lambda_s} - \frac{1}{\lambda_p} = \frac{1}{\lambda_p} - \frac{1}{\lambda_I} \qquad (2.83)$$

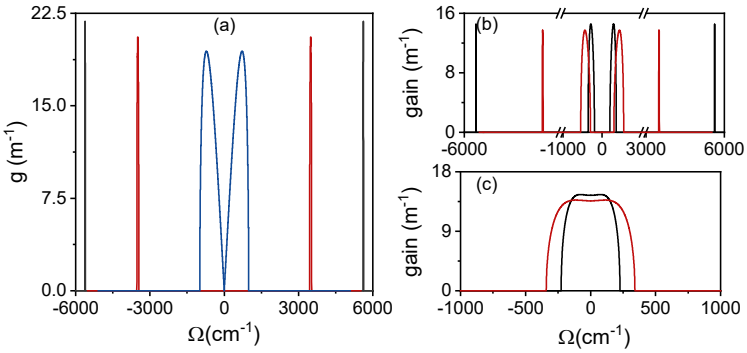

Figure 2.8. Parametric gain as a function of frequency shift of (a) FWM. Parametric gain of PMI when the pump excites the (b)slow and (c) fast axis of the FUT. With pump wavelengths at: λ_1 (black line); λ_2 (red line) and λ_3 (blue line). $P_0=2.5$ *kW;* $\Delta n=10^{-6}$;

Fig. 2.8 shows the parametric gain of FWM/PMI when the test wavelengths (λ_1, λ_2 and λ_3) are considered as the pump wavelength. From Eq. 2.43 we can observe that the gain of the FWM process strongly depends on the linear phase mismatch and its maximum gain is $g_{max} = 2\gamma P_0$, such condition requires the fulfillment of $\kappa = 0$. Note that the spectral bandwidth of the FWM sidebands generated when the fiber is pumped in the normal dispersion regime increases as λ_p approaches λ_{ZDW}. This behavior, shows the dependence of the FWM gain profile on the slope of the net phase mismatch $d\kappa / d\omega$, which is also related to the dispersion of the fiber itself [7].

Figs. 2.8 (b) - (c) shows the PMI gain when the test wavelengths (λ_1 and λ_2) are considered as the pump wavelength. In the wavelength range under study, the calculated power threshold of PMI is about $P_{Th} \sim 1.1$ kW, considering a phase birefringence of 10^{-6}. When PMI is produced by slow-axis pump, the gain profile shows two pairs of sidebands detuned from the pump wavelength (located at $\Omega = 0$). Notice that the outer pair of sidebands produced are spectrally quite narrow. The frequency shift of these outer bands is quite large, and similar to those produced by FWM when the fiber dispersion is normal at the pump wavelength. On the other

hand, when PMI is produced by fast-axis pumping, the gain profile shows a broad band centered at the pump wavelength. It is worth to note that the gain shape for the F-S PMI process depends on P_0. The gain at zero detuning does not vanish regardless the pump power and it eventually can show two gain peaks near the edges provided that P_0 is high enough.

The gain bandwidth of the PMI sidebands exhibits a complex dependence on $d\kappa/d\omega$ slope. In the case of S-F PMI, the bandwidth of the sidebands does not change substantially with λ_p as shown in Fig. 2.8 (b). The opposite happens in the case of F-S PMI, the gain bandwidth increases as λ_p approaches λ_{ZDW} as shown in Fig. 2.8 (c). A complete review of PMI is discussed in Chapter 4.

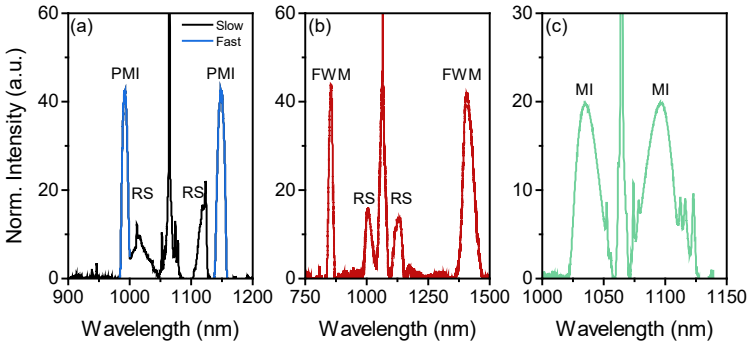

Figure 2.9. Light spectra recorded at the output of three MOFs with different dispersion at the pump wavelength (λ_p = 1064 nm): (a) large normal dispersion ($\lambda_p \sim \lambda_1$); (b) low normal dispersion ($\lambda_p \sim \lambda_2$); (c) anomalous dispersion ($\lambda_p \sim \lambda_3$). Raman Scattering (RS).

In order to illustrate the generation of PMI/FWM and the role of fiber dispersion, in this section we include some experimental results concerning the spectral response of three MOFs with different dispersion regimes at the pump wavelength (λ_p = 1064 nm). The MOFs were designed and fabricated to be able to generate PMI or FWM. Experimental techniques and procedures to excite and characterize such nonlinear effects are discussed in detailed in Chapter 3. Figure

2.9(a) shows PMI sidebands generated under slow-axis pumping produced in a fiber with large normal dispersion. The blue line shows the two inner sidebands, the polarization of which is oriented to the fiber fast-axis. The black line represents the spectral components with polarization aligned to the fiber slow-axis, which includes the remaining pump wave and two band generated by Raman scattering (RS). Notice that spectral bands corresponding to the outer pair of PMI solutions are not shown.

FWM sidebands produced in a MOF with low-normal dispersion are shown in Fig. 2.9(b) and the effect of scalar modulation instability produced in a MOF with anomalous dispersion is shown in Fig. 2.9(c). In both, the different spectral components exhibit the same polarization. The spectral bandwidth of FWM and MI sidebands shows the characteristics previously described according with the dispersion of the fiber. The results shown here are consistent with the predicted by the theoretical model representing the PMI/FWM effect. For the purpose of this thesis, in the simulations included in the following sections of this chapter, we only consider PMI generated by slow-axis pumping, as this is the case capable of producing detuned sidebands and does not present a power condition for it to occur.

2.4 Impact of fiber parameters in FWM/PMI

Having described the FWM/PMI processes, we numerically investigate the dependence of the frequency shift of the FWM/PMI sidebands on the different fiber parameters involved in the process. In the case of PMI, we focus on the inner pair of solutions. In particular, we investigate the impact on the phase-matching condition as a function of the fiber nonlinear parameter, the fiber birefringence and also the fiber dispersion. The aim of this section is to provide the theoretical knowledge on which most of the experimental results included in the thesis are based.

2.4.1 Nonlinear contribution

In the case of optical fibers, the efficiency of nonlinear processes is highly dependent on the nonlinear parameter γ of the fiber, which is related to the nonlinear refractive index n_2 of fused silica and the effective area of the guided mode, A_{eff}. Fused silica exhibits a relatively small nonlinear refractive index compared to other glass fibers [20]. n_2 is an optical quantity intrinsically fixed by the fiber material and its control by an external factor becomes a difficult task. A_{eff} is a quantity that can be adjusted up to a certain extend by fiber design. In this regard, MOF technology allows obtaining fibers with small values of A_{eff} by designing fibers with a small core and large numerical aperture, leading to fibers with large γ parameter.

It has been shown previously that the gain of nonlinear FWM/PMI processes depend on γ and on the total pump power P_0. The phase-matching conditions (Eq. 2.39 and Eq. 2.68) include a nonlinear term also dependent on the product $\gamma \cdot P_0$. In a given fiber, the parameter γ is fixed by the fiber structure, however pump power is a quantity that can be adjusted easily in an experimental implementation. Therefore, we investigate the nonlinear contribution to the phase-matching condition of FWM/PMI when varying the power of the pump injected into a MOF with small mode area. For the calculations, we considered a maximum peak power of 8 kW which is similar to the highest power delivered by the light source used in most of our experiments.

Figure 2.10 shows the dependence of the detuning frequency of FWM/PMI on pump power, for the FUT analyzed in the previous section. Calculations are done for the three test wavelengths λ_1, λ_2 and λ_3. The effective mode area of this fiber for the wavelengths of interest is approximately $Aeff \sim 22\ \mu m^2$. It can be seen that the detuning frequency of both, FWM and PMI increases with increasing pump power.

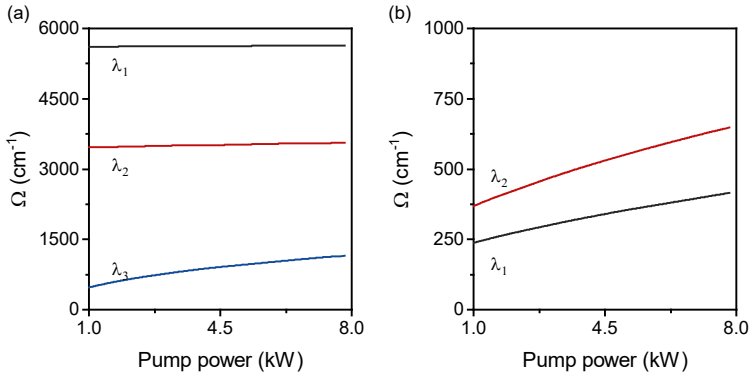

Figure 2.10. Detuning frequency as a function of the pump power of (a) FWM and (b) PMI.

In the case of FWM bands, when the fiber dispersion at the pump wavelength is normal ($\lambda_p < \lambda_{ZDW}$), the frequency shift depends slightly on pump power when λ_p is far from λ_{ZDW} (see for example, $\lambda_p = \lambda_1$), and it increases as λ_p approaches λ_{ZDW} (see for example, $\lambda_p = \lambda_2$). That happens because the linear phase mismatch contribution is significantly larger than the nonlinear term when the dispersion at the pump wavelength is large, thus the effect of pump power changes is minor.

When pumping near zero dispersion, in both normal and anomalous dispersion regimes, the linear phase mismatch contribution is relatively small, so the detuning frequency of the FWM sidebands becomes more dependent on the nonlinear phase mismatch term, thus the sensitivity to changes of pump power is more significant. The PMI detuning frequency exhibits somewhat a similar pump power dependence, where its contribution becomes more relevant when the excitation wavelength λ_p approaches λ_{ZDW}, as shown in Fig. 2.9 (b) when $\lambda_p = \lambda_2$.

2.4.2 Effect of chromatic dispersion variations

The linear term in the phase-matching condition for FWM/PMI, contains the difference between the values taken by the propagation factor for pump, *signal* and

idler wavelengths. The dependence of $\Delta\beta$ on the fiber chromatic dispersion can be easily infer if we approximate the propagation factor by a second-order expansion. Then, the linear phase mismatch can be written as,

$$\Delta\beta = 2\beta_p - \beta_s - \beta_i \approx -\beta_2 \cdot \Phi^2 \qquad (2.84)$$

MOFs are known to exhibit a versatile dispersion design attributed to the structural parameters of their microstructured region. Moreover, the transmission parameters of a MOF can be adjusted after their fabrication stage by different post-fabrication techniques [21–24]. For instance, in different experiments included in this thesis, MOF dispersion was modified after fibers were fabricated by a method based on filling the holes of the fiber with a substance with a given refractive index. This technique, allowed us to modify dynamically the dispersion of the fiber, taking advantage of large thermo-optic coefficient of the substance, by controlling the fiber temperature. In the literature, other different strategies based on infiltrating materials with different properties, as liquid crystals [25] and magnetic solutions [26], have been reported to control the waveguiding properties of the fiber by controlling an external parameter, i.e. temperature, pressure, electric or magnetic fields, etc. [26–29].

In this section, we investigate the dependence of the phase-matching condition of FWM/PMI with fiber dispersion. For these calculations, we consider a FUT with the holes of the microstructure filled with a given refractive index n_H. The fiber dispersion characteristic is modified through changes of n_H. The structural parameter of the fiber taken as FUT for these calculations are the same as in Fig. 2.7. The propagation factor of the fundamental guided mode, mode area and the detuning frequency response of FWM and PMI were calculated for increasing values of n_H starting from $n_H = 1$. In these series of calculations, the pump power and the fiber birefringence were maintained constant.

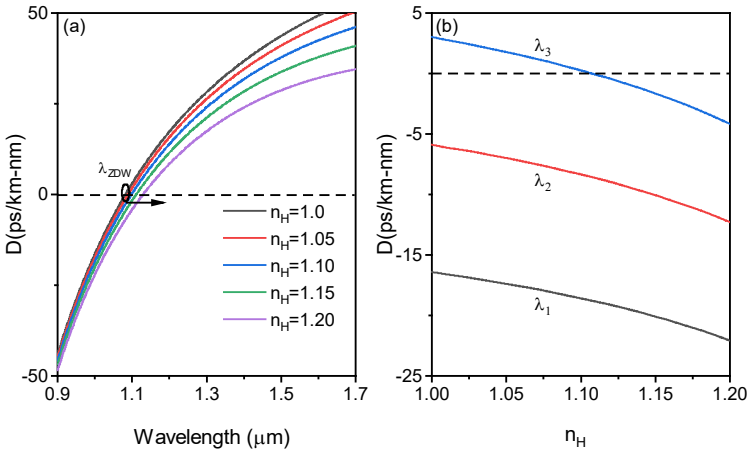

Figure 2.11. (a) Chromatic dispersion as a function of the optical wavelength at different values of n_H. (b) Dispersion at the test wavelengths as a function of n_H. Horizontal dashed line shows the zero of dispersion.

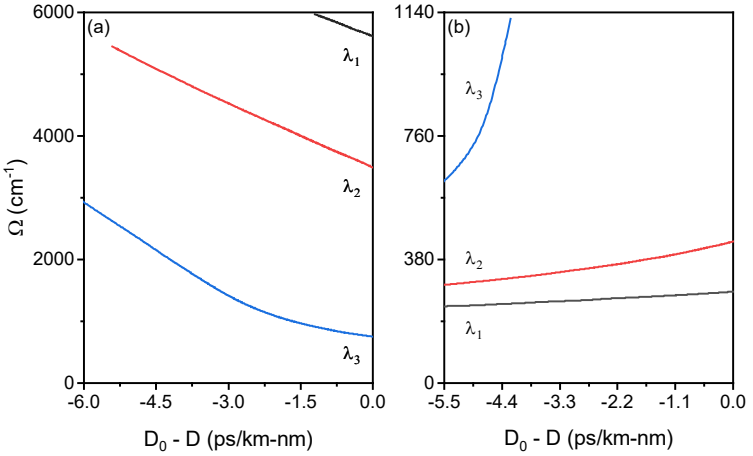

Figure 2.12. Detuning frequency as a function of the dispersion change at the test wavelengths. (a) FWM and (b) PMI.

Figure 2.11 (a) shows that the λ_{ZDW} shifts towards longer wavelengths and the dispersion decreases as the refractive index of the holes is increased. Notice that fiber dispersion decreases in major proportion at longer wavelengths, and the λ_{ZDW}

shifts toward longer wavelengths from 1.08 μm to 1.13 μm within the studied range of the refractive index increment. Figure 2.11 (b) shows the dispersion at the test wavelengths. It can be observed that dispersion at the three test wavelengths varies smoothly with the increment of the refractive index. Notice that dispersion at λ_3 experiences a transition from anomalous to normal dispersion for a refractive index of $n_H = 1.10$.

The detuning frequency as a function of the fiber dispersion change for FWM and PMI is shown in Fig. 2.12. For calculations, we considered the change in chromatic dispersion around the set value D_0, which was evaluated at $n_H=1$. In the case of FWM, the frequency detuning decreases as the dispersion increases, which indicates that the frequency shift of the FWM has a negative slope. The opposite occurs for PMI, where its detuning frequency increases when the fiber dispersion increases, thus showing a frequency shift with a positive slope. Depending on the test wavelength, different characteristics can be observed. For example, the frequency shift can be larger or smaller, in the case λ_2 and λ_3, a large range of frequency shift can be observed in both FWM and PMI, the opposite is observed when considering the wavelength λ_1. This indicates that the frequency shift of FWM and PMI becomes more sensitive to dispersion variations when pumping near the dispersion zero. By considering $\lambda_p = \lambda_3$, the transition between the two dispersion regimes enables PMI to be generated due to normal dispersion at the pump wavelength. For this particular wavelength, the frequency tuning range is the largest for both PMI and FWM.

Numerical results show that a proper design of the MOF dispersion, and the control of the refractive index of the holes can be exploited to achieve large tuning ranges of the sidebands produced by FWM or PMI. In this thesis, we include different experiments based on fibers infiltrated with suitable liquids where large tuning of FWM/PMI sidebands is achieved.

2.4.3 Fiber birefringence

In the case of PMI, a small amount of residual fiber birefringence contributes positively to the frequency shift between the PMI sidebands and the pump, as stated in Eqs. 2.68. In this section, we study numerically the effect of the fiber birefringence on the PMI frequency shift. The FUT assumed for these calculations has the same structural parameters as in Fig. 2.7, with air holes. Pump power and fiber dispersion are assumed as fixed parameters, while birefringence was varied from 0 up to 10^{-4}.

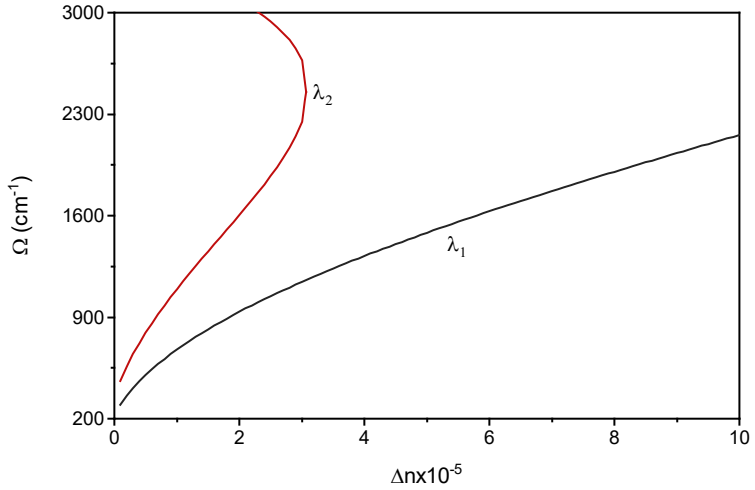

Figure 2.13. Detuning frequency of PMI sidebands as a function of fiber birefringence for λ_1 and λ_2.

Figure 2.13 shows the detuning frequency of the PMI sidebands as a function of birefringence. Note that the detuning frequency increases with increasing fiber birefringence. Therefore, the birefringence adds positively to the PMI frequency shift. When pump wavelength is near the zero-dispersion wavelength (see the case $\lambda_p = \lambda_2$) a large tuning range can be achieved for small variations of birefringence. Additionally, a very interesting feature is shown, the detuning frequency curve bends and a turning point is shown. This indicates that PMI cannot be generated for a

birefringence larger than a certain amount ($\Delta n \sim 3\times10^{-5}$ for this particular case). This indicates that the fiber birefringence plays an important role in the net-phase-mismatch where neither the dispersion nor the nonlinear contribution can compensate for the birefringence contribution, and thus the phase-matching condition is no longer satisfied at this particular pump wavelength. The latter feature was not observed, at least within the birefringence range considered here, when considering a pump wavelength far from the zero of dispersion (see the case $\lambda_p = \lambda_1$).

We would like to emphasize that managing the birefringence of an optical fiber can lead to a simple way to control the spectral position of the PMI sidebands. It is well known that mechanical deformations can be used to induce linear birefringence into an optical fiber [30–32]. Actually, the range of birefringence taken into account in the calculations shown in Fig. 2.13 corresponds to experimental values of induced birefringence reported [30–32].

References

1. I. H. Malitson, "Interspecimen Comparison of the Refractive Index of Fused Silica*,†," J. Opt. Soc. Am. **55**, 1205 (1965).
2. A. W. Snyder and W. R. Young, "MODES OF OPTICAL WAVEGUIDES.," J Opt Soc Am **68**, 297–309 (1978).
3. G. P. Agrawal and M. J. Potasek, "Nonlinear pulse distortion in single-mode optical fibers at the zero-dispersion wavelength," Phys. Rev. A **33**, 1765–1776 (1986).
4. P. N. Butcher and D. Cotter, *The Elements of Nonlinear Optics* (Cambridge University Press, 1990).
5. R. W. Boyd, *Nonlinear Optics* (Elsevier Inc., 2008).
6. C. Li, *Nonlinear Optics: Principles and Applications* (2016).
7. G. P. Agrawal, *Nonlinear Fiber Optics* (Elsevier, 2019).

8. Q. Lin and G. P. Agrawal, "Vector theory of four-wave mixing," J. Opt. Soc. Am. B **21**, 1216–1224 (2004).

9. L. Velázquez-Ibarra, "External control of spontaneous four wave mixing in photonic cyrstal fibers," Universidad de Guanajuato (2013).

10. G. S. He and S. H. Liu, *Physics of Nonlinear Optics* (WORLD SCIENTIFIC, 1999).

11. J. P. Gordon and H. Kogelnik, "PMD fundamentals: Polarization mode dispersion in optical fibers," Proc. Natl. Acad. Sci. U. S. A. **97**, 4541–4550 (2000).

12. R. H. Stolen and J. E. Bjorkholm, "Parametric Amplification and Frequency Conversion in Optical Fibers," IEEE J. Quantum Electron. **18**, 1062–1072 (1982).

13. A. J. Rogers, "*Polarization in optical fibers*," 273 (2008).

14. F. Yaman, Q. Lin, and G. P. Agrawal, "Effects of Polarization-Mode Dispersion in Dual-Pump Fiber-Optic Parametric Amplifiers," IEEE Photonics Technol. Lett. **16**, 431–433 (2004).

15. Q. Lin and G. P. Agrawal, "Effects of polarization-mode dispersion on fiber-based parametric amplification and wavelength conversion," Opt. Lett. **29**, 1114 (2004).

16. C. McKinstrie, S. Radic, and C. Xie, "Parametric instabilities driven by orthogonal pump waves in birefringent fibers," Opt. Express **11**, 2619 (2003).

17. B. Daino, G. Gregori, and S. Wabnitz, "New all-optical devices based on third-order nonlinearity of birefringent fibers," Opt. Lett. **11**, 42 (1986).

18. H. G. Winful, "Polarization instabilities in birefringent nonlinear media: application to fiber-optic devices," Opt. Lett. **11**, 33 (1986).

19. G. Gregori and S. Wabnitz, "New exact solutions and bifurcations in the spatial distribution of polarization in third-order nonlinear optical interactions," Phys. Rev. Lett. **56**, 600–603 (1986).

20. S. R. Friberg and P. W. Smith, "Nonlinear optical glasses for ultrafast optical switches," IEEE J. Quantum Electron. **23**, 2089–2094 (1987).

21. K. Nielsen, D. Noordegraaf, T. Sørensen, A. Bjarklev, and T. P. Hansen, "Selective filling of photonic crystal fibres," J. Opt. A Pure Appl. Opt. **7**, L13–L20 (2005).

22. Y. Huang, Y. Xu, and A. Yariv, "Fabrication of functional microstructured optical fibers

through a selective-filling technique," Appl. Phys. Lett. **85**, 5182–5184 (2004).

23. J. H. Lim, K. S. Lee, J. C. Kim, and B. H. Lee, "Tunable fiber gratings fabricated in photonic crystal fiber by use of mechanical pressure," Opt. Lett. **29**, 331 (2004).

24. C. Kerbage and B. Eggleton, "Numerical analysis and experimental design of tunable birefringence in microstructured optical fiber," Opt. Express **10**, 246 (2002).

25. S.-M. Kuo, Y.-W. Huang, S.-M. Yeh, W.-H. Cheng, and C.-H. Lin, "Liquid crystal modified photonic crystal fiber (LC-PCF) fabricated with an un-cured SU-8 photoresist sealing technique for electrical flux measurement," Opt. Express **19**, 18372 (2011).

26. H. V. Thakur, S. M. Nalawade, S. Gupta, R. Kitture, and S. N. Kale, "Photonic crystal fiber injected with Fe3O4 nanofluid for magnetic field detection," Appl. Phys. Lett. **99**, 161101 (2011).

27. Y. Wang, M. Yang, D. N. Wang, and C. R. Liao, "Selectively infiltrated photonic crystal fiber with ultrahigh temperature sensitivity," IEEE Photonics Technol. Lett. **23**, 1520–1522 (2011).

28. D. J. J. Hu, J. L. Lim, Y. Cui, K. Milenko, Y. Wang, P. P. Shum, and T. Wolinski, "Fabrication and characterization of a highly temperature sensitive device based on nematic liquid crystal-filled photonic crystal fiber," IEEE Photonics J. **4**, 1248–1255 (2012).

29. Y. Huang, Y. Wang, L. Zhang, Y. Shao, F. Zhang, C. Liao, and Y. Wang, "Tunable Electro-Optical Modulator Based on a Photonic Crystal Fiber Selectively Filled with Liquid Crystal," J. Light. Technol. **37**, 1903–1908 (2019).

30. R. Ulrich, S. C. Rashleigh, and W. Eickhoff, "Bending-induced birefringence in single-mode fibers I „," **5**, 273–275 (1980).

31. Z. Zhu and T. G. Brown, "Stress-induced birefringence in microstructured optical fibers," Opt. Lett. **28**, 2306 (2003).

32. S. F. Feldman, D. A. Weinberger, and H. G. Wingful, "Polarization instability in a twisted birefringent optical fiber," Appl. Opt. **32**, 1191–1201 (1993).

Chapter 3

Microstructured optical fibers and experimental procedures

This chapter describes the type of microstructured optical fibers used throughout this research project and their relevance. The modeling of the waveguiding properties of the fibers along with the fabrication technique is addressed. The experimental procedures employed to excite the nonlinear effects in such fibers, as scalar FWM or vector FWM are described. The experimental setup used for the characterization of such nonlinear effects will be described in detail. The post-fabrication technique for controlling the dispersion of a MOF is also included.

3.1 Microstructured optical fibers

Microstructured optical fiber, also known as photonic crystal fiber, is an optical fiber based on the properties of photonic crystals. Since this type of fibers appeared, many forms have been developed in order to optimize different properties [1–6]. In the basic form, the cross-section of a MOF includes a 2D microstructure formed by a periodic lattice of inclusions of a different material than the matrix material, which extend longitudinally along the fiber. These fibers include a defect in the microstructure that acts as the fiber core. In the majority of MOFs, the inclusions that form the periodic microstructure are just air holes. Fig. 3.1 shows a scheme of

the cross-section of common MOFs. The periodicity of the lattice and the diameter of the holes are in the same order of magnitude of the optical wavelength. The propagation of light is determined by the photonic microstructure, which limits the transverse propagation of light by the existence of forbidden bandgaps for certain propagation factors, therefore, the electromagnetic field at those forbidden frequencies are confined into the MOF core [7].

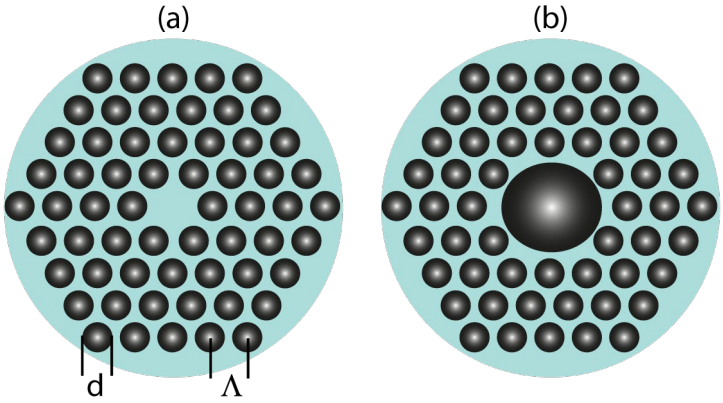

Figure 3.1. Cross section of (a) solid-core MOF and (b) hollow-core MOF. Blue color shows the fused silica material and gray color represent air.

In principle, MOFs can be classified in two families [1]. In the first, the confinement of light occurs when the propagation factor of the guided mode matches with the forbidden bandgap of the 2-D photonic microstructure and, therefore, the guided mode is diffracted by the microstructure and confined into the core region. Typically, such fibers are named as photonic bandgap (PBG) fibers, which the refractive index of the core can be smaller than the "average refractive index" of the photonic microstructure that surrounds the core. In most cases, PBG fibers present a hollow core, normally filled with air (see fig. 3.1(b)), although all-solid PBG have also been demonstrated [8]. The second group of MOFs are known as index-guiding fibers. In these fibers, the refractive index of the core material is

larger than the "average refractive index" of the photonic microstructure. In this case, the confinement of the light occurs similarly as it happens in step-index fibers, in which the confinement of the light is determined by total internal reflection. In most of the cases, such fibers present a solid-core made of the same material than the matrix material of the photonic microstructure.

In the context of silica-based optical fibers, in 1996 J. C. Knight et.al. reported the fabrication of the first single-mode solid-core fiber with a photonic crystal cladding made of air-holes [2]. Since then, MOFs have been widely studied in the past decades because of their unique optical properties, among which the most relevant can be: optical guidance in hollow core fibers, tailoring of fiber chromatic dispersion, endlessly single-mode operation, high birefringence and high nonlinearity [9–16]. In recent years, a number of applications based on MOF technology have been developed. For example, in photonic applications such as fluid refractometry [17], bio-detection [18,19], temperature sensing [20] and gas sensing [21] have been proposed with silica-MOFs as platforms for light-matter interaction. In addition, new designs of MOFs based on soft glasses has been proposed for nonlinear applications as supercontinuum generation [22]. Currently, MOF technology remains an open research topic for the development of waveguides in applications based on the THz frequency range [22, 23].

In the present work, we focus specifically on solid-core silica MOFs with a triangular lattice of air holes with constant diameter. The periodic structure forms the fiber cladding and the omission of the central air-hole forms the fiber core (see Fig. 3.1 (a)). The guiding properties of these type of fibers is determined by the optical properties of the fiber material (pristine SiO_2) along with the photonic structure itself. Therefore, the hole diameter d and the lattice pitch Λ (period of the photonic structure) are the parameters that define the waveguide properties of silica MOFs. In particular, by engineering of d and d/Λ, the chromatic dispersion, which

is a key feature for the generation FWM, can be tailored so that fibers with a wide range of dispersion profiles can be designed and fabricated. Fig. 3.2 shows an example of the chromatic dispersion profile of MOFs with different structural parameters.

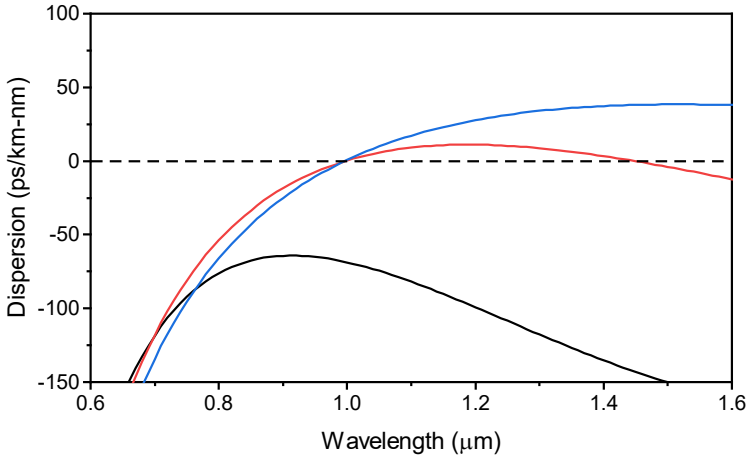

Figure 3.2. Chromatic dispersion as a function of wavelength of MOFs. Fibers structural parameters: $d/\Lambda=0.40$ (fixed), $\Lambda=1.0$ μm *(black line),* $\Lambda=1.5$ μm *(red line)* and $\Lambda=2.0$ μm *(blue line).*

To illustrate the flexibility for the design of chromatic dispersion of MOFs, Fig. 3.2 shows the dispersion profiles of three MOFs with the same d/Λ ratio and slight variations of the pitch length. Different dispersion profiles as a function of wavelength are shown. When $\Lambda=1.0$ μm, normal dispersion is observed over a wide wavelength range. This particular type of fiber is known as all-normal dispersion (ANDi) MOFs. A dispersion profile exhibiting one or two ZDW are shown for pitch values of 1.5 μm and 2.0 μm, respectively.

In principle, solid-core MOFs can eventually be designed to present several advantages that can be exploited for the generation of nonlinear effects, e.g., small effective area which enables strong optical field density, and unprecedented

flexibility for chromatic dispersion design. Such features make this type of fibers an excellent platform for the development of nonlinear optics. Therefore, in the present work, we exploit the potential advantages of MOFs to design and fabricate fibers with chromatic dispersion suitable for scalar and vector FWM generation. In the following, we will describe the fabrication method employed to obtain the MOFs that were used throughout this thesis.

3.2 MOFs fabrication method

The development of nonlinear MOFs with suitable optical properties for FWM generation are part of the main objectives of this research project. The MOFs used during the experiments have been fabricated in the facilities of the University of Valencia, specifically at the Laboratory of Fiber Optics (LFO). The method used for the fabrication of a MOF involves two steps: (i) First, the MOF is designed according to the requirements of the particular application that is aimed to be investigated. For this purpose, we employ a software developed at the LFO to model the waveguide properties of MOFs in order to obtain the structural parameters required. (ii) Once the structural parameters of the MOF are set, the fibers were fabricated. Then, the cross-section of the fibers fabricated were characterized by scanning electron microscopy (SEM). Fibers that fulfilled the design parameters were then chosen and used in experiments. Each step is described below.

3.2.1 Waveguiding modeling of MOFs

Due to the complexity of the transverse refractive index distribution of a MOF, accurate theoretical evaluation of the waveguiding properties becomes a difficult task. With the advent of MOFs, several modeling techniques have been proposed to describe the chromatic dispersion, mode effective area and waveguide losses of these

fibers. Among them, the most relevant are the effective index method (EIM) [25–28] and full-vector method [29–32]. Knight et.al. [25], proposed a simple method, which is based on the approximation of a solid-core MOF to a step-index fiber. Then, the propagation constant of the guided mode can be easily derived with the well-known general dispersion relation of the step-index fiber [33]. In this method the main task is to derive the so-called fundamental space-filling effective refractive index of the photonic structure, which is then taken as the effective refractive index of the cladding of a step-index fiber. The proper value of core radius of the equivalent step-index fiber is an issue that raised certain discussion in the community, and various options have been proposed [10, 24, 33, 34]. In this approximation, the microstructured region is assumed that has infinite extent in the transversal direction, whereas a realistic MOF has finite number of holes rings. This has two main consequences, the modeling loses accuracy to describe the fiber properties, and second, confinement losses due to the finite number of periods is not described [36]. Saitoh et.al., [27], proposed semi-empirical analytical relations for the dispersion of the fundamental mode of solid-core microstructure silica fibers with triangular lattice of air-holes, this method is based on a compilation of several numerical simulations of MOFs based on other numerical approaches. The proposed relations describe with good accuracy the chromatic dispersion of fibers with pitch lengths between 1 μm and 3 μm and ratio d/Λ between 0.2 and 0.8.

In our work, we use a software named *Itera*, developed to evaluate the propagation of light in complex two-dimensional structures with a non-trivial spatial distribution of the refractive index. *Itera* allows calculating the linear guiding properties of the modes supported by the MOF. The mode solver method for MOFs was developed by E. Silvestre et.al [37], and it is based on the full-vector method (FVM) proposed in [29]. *Itera* solves the wave equation following the constraints of Maxwell's equations, in which the transverse electric and magnetic fields are evaluated considering the anisotropy in the dielectric tensor. It is known that fused

silica can be considered as an isotropic material, however, the transverse components of the dielectric tensor experience effective anisotropy induced by interfaces separating different isotropic materials, which is the case for the photonic structure of a MOF. Due to the complexity of the differential wave equations, an iterative Fourier method is employed to evaluate the eigenvalues equations that describes the electromagnetic field in the MOF. This method takes advantage of the different representations of the spaces to express the differential wave equation as a diagonalizable system in the form of algebraic equations.

According to the designation of the structural parameters of a MOF, *Itera* can simulate the realistic fiber geometry along with the refractive index distribution to provide the waveguiding properties of a MOF. As a result, the propagation factors of the guided modes β and their group velocities $(\beta_1)^{-1}$ are obtained with high accuracy, furthermore, *Itera* can provide fiber parameters as phase birefringence and mode-field diameter which are relevant to accurately describe the generation of vector-FWM in optical fibers. We would like to highlight that *Itera* can also evaluate complex transverse geometries of a MOF, where the exact refractive index distribution can be obtained through SEM images of the MOFs cross sections, i.e. fibers with non-homogenous hole diameters and/or pitch lengths.

Fig. 3.3 shows the waveguiding properties of different MOFs. The comparison between modeling the dispersion properties of MOFs using EIM [28] and *Itera* is shown in Fig 3.3(a). The difference between the two methods can be seen. It is known that the main source of EIM error arises from the core radius (r_c) designation [38], $r_c=\Lambda - d/2$ [28] was assumed for fundamental mode calculations. *Itera* (FVM) exhibits better accuracy for the determination of the guided modes, as it was corroborated in [15, 29] with excellent agreement between experimental results and theoretical calculations. Figures 3.3 (b) and (c) shows the group index and the effective area of the fundamental mode for different MOFs. A_{eff} is a quantity

related to the area that the fields of a guided mode effectively cover the cross section of an optical fiber. In the context of MOFs, A_{eff} depends on wavelength, and on the structural parameters of the fiber.

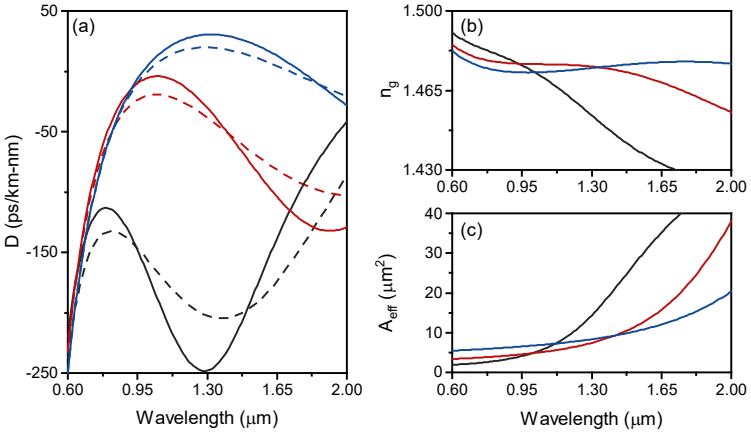

Figure 3.3. (a) Chromatic dispersion, (b) group refractive index and (c) effective mode area for MOFs with structural parameters: d/Λ=*0.40* (fixed), Λ=*1.0* μm *(black line),* Λ=*1.5* μm *(red line)* and Λ=*2.0* μm *(blue line).* Solid lines are numerical results obtained from *Itera* and dashed lines from an effective index method [28].

3.2.2 Description of MOFs fabrication technique and system

Since the first report of MOFs fabrication [2], several techniques have arisen in the subsequent years to fabricate such type of fibers. Among the most remarkable, we can mention the extrusion technique [39] and *stack-and-draw* technique [2, 40]. Such techniques are preferred according, generally, to the type of material with which the fiber will be made. For example, the extrusion technique is preferred for microstructured fibers made of soft glasses or polymers due to the low temperatures for plastic deformation of those materials (150 °C - 550 °C). On the other hand, for fibers made of glasses with a high melting point as silica (~2000 °C), the *stack-and-draw* technique has established itself as the standard technique for manufacturing this

type of fibers. The fibers used in this research project were all fabricated following this method.

The *stack-and-draw* technique requires the use of an optical fiber drawing tower. The system that we employed to fabricate our MOFs is based on a drawing tower commonly used for the fabrication of standard optical fibers that has been modified accordingly to fulfill the specific requirements for the fabrication of MOFs. The system comprises two main subsystems: (i) A high temperature furnace with the devices and controls required for its operation, and (ii) a set of mechanical and electronic devices necessary to align and monitoring the drawing process of capillaries and fiber preforms. Fig. 3.4 shows the schematic of the fiber drawing tower employed for MOFs fabrication.

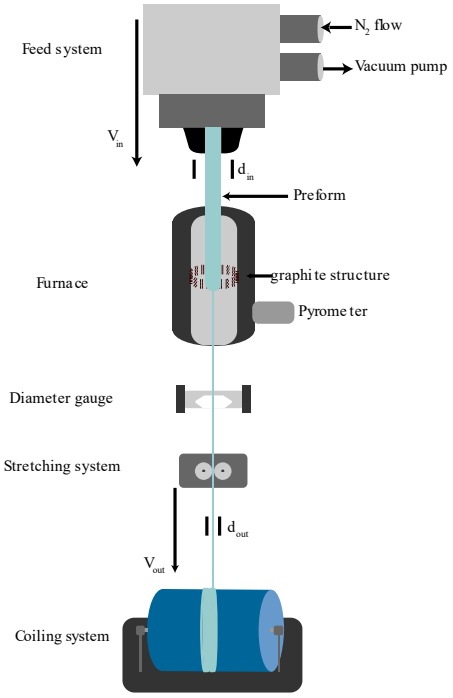

Figure 3.4. Schematic of the optical fiber drawing tower for MOFs manufacturing.

The drawing tower allows to reduce the diameter of a glass rod from cm to μm through the heating and stretching system. The glass rods are introduced into the furnace with an X-Y alignment holder that allows the alignment between the glass rod and the furnace. The X-Y holder is designed so that it allows applying a gas pressure or to create vacuum within some specific parts of the glass structure. This is required in some stages of the fiber fabrication procedure, as it is described below. The furnace is cylindrical with two circular openings at the top and bottom, the openings act as inlet and outlet stages for the glass rod, respectively. The maximum diameter of the inlet opening is 2 cm.

The furnace consists of a tubular graphite element of low electrical resistivity, capable of conducting more than 2000 A. The heat is produced by the graphite element through Joule effect. The furnace is capable of reaching temperatures above the melting point of fused silica. The temperature is controlled by the electric current applied to the graphite element and a pyrometer is used to measure the temperature in the furnace. During the heating stage, an inert atmosphere is required to prevent degradation of the graphite element due to oxidation at high temperatures, so that, a flow of argon gas is injected into the inner region of the furnace, which flows out the furnace through the openings.

Under the furnace, at a certain distance a diameter gauge is located which allows the diameter of the stretched glass rod to be measured in real time. The operating principle of the device is based on the measurement of the diffraction pattern produced by the stretched glass rod when it is illuminated with a laser beam. The device is capable of measuring diameters from 30 μm to 5 mm with an accuracy of ± 1 μm. Below the diameter gauge is the stretching system for preforms and capillaries. The system consists of two wheels coated with silicone rubber that act simultaneously on the glass rod, pulling down the glass rod to reduce its diameter.

The wheels act mechanically through two motors at variable speeds between 0.5 m/min and 2.5 m/min.

At the bottom of the drawing tower is located a cylindrical drum with a diameter of 30 cm. During the fabrication stage of the fibers the drum is used to pull and coil the fiber in the drum itself. The soft curvature of the drum permits to coiled the fiber without coating polymer avoiding cracks or defects. The drum axially spins, the rotation is given by the mechanical action of a motor with a maximum speed of 12 m/min. The pulling speed of the fiber is controlled with the speed of the drum.

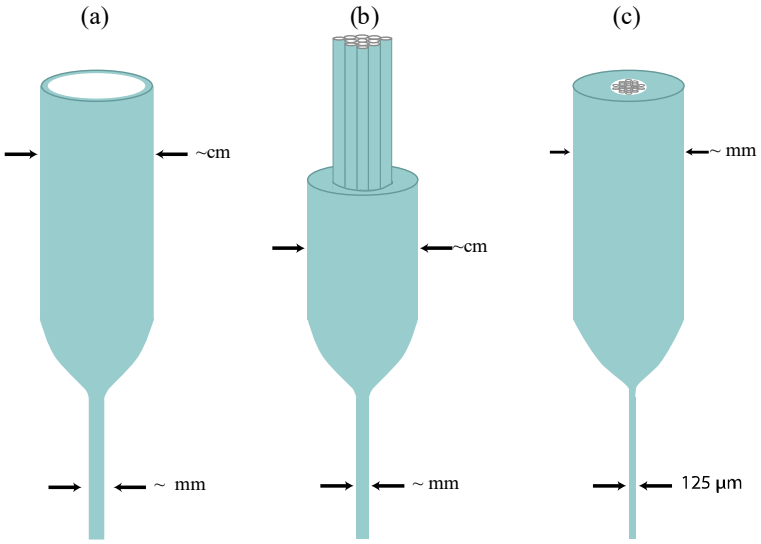

Figure 3.5. Schematic of (a) capillary, (b) preform, and (c) MOF drawing.

As mentioned before, all the fibers used in this thesis were made of silica. In particular, the glass used was *Suprasil-F300* commercialized by Heraeus Inc., which is the most widely used for optical fiber technology due to its low concentration of OH^- ions (< *1 ppb*). The MOF fabrication procedure can be summarized in four stages. In the first one, the capillaries and the glass rods required to form the cross-section of the fiber are fabricated. To obtain the capillaries, a glass tube of about ~

2 cm diameter is introduced into the furnace and once the temperature for plastic deformation of silica (~1800 °C) is reached, then the tube is pulled-down to decrease its diameter to a few mm, as shown in Fig. 3.5 (a). The outer diameter of the capillaries can be controlled by adjusting the rate at which the tube is pulled in and out of the furnace. In the case of capillaries, the wall thickness is set by the wall thickness of the pristine tube. Let d_{ti} and d_{to} be the inner and outer diameter of the tube, respectively, then the tube is introduced into the furnace at the velocity v_{in} and extracted at a velocity v_{out}. The inner diameter d_{ci} and outer diameter d_{co} of the capillary can be derived according to mass conservation as follows,

$$\left({d_{to}}^2 - {d_{ti}}^2\right)v_{in} = \left({d_{co}}^2 - {d_{ci}}^2\right)v_{out} \qquad (3.1)$$

Eq. 3.1 can be adapted for the case of solid glass rods by making the inner diameter of the tube tend to zero.

The second stage consists of the stacking and arrangement of the capillaries and solid canes in order to form the desired cross-section of the MOF. Given the dimensions of the capillaries/rods, the cross-section of such arrangement is in the order of few centimeters. At this stage, various configurations of the MOF cross-section can be designed. For example, depending on the thickness or diameter of some capillaries, fibers of non-uniform geometry can be fabricated. In addition, MOFs with several cores, or fibers with doped cores can also be fabricated.

The third stage consists of packing the capillary/rod arrangement and stretching it to obtain the fiber preform. A tube with a suitable wall thickness and diameter (compatible with the size of the capillary/rod lattice) is used as a jacket to hold the capillary/rod lattice. The jacket prevents lattice deformation during the stretching process and adds silica to the fiber. The wall thickness of jacket must be adequate to obtain fibers with the desired dimensions, ideally ~125 μm in diameter. The whole structure including the silica jacket and the capillary/rod arrangement is

heated in the drawing tower furnace and drawn using the wheels to obtain the fiber preform, whose diameter is typically of a few millimeters. Fig. 3.5 (b) shows the schematic showing the before and after manufacturing of the fiber preform. During this drawing stage, vacuum is created between the jacket and the arrangement to help closing the space between them and also the small air gaps between adjoining capillaries. The resulting preform has the cross-section of the target fiber, but with dimensions scaled by several orders of magnitude (between ~10 and ~30 times larger).

The fourth stage consists of obtaining the target fiber from the preform by stretching it. Then, the preform is inserted in the drawing tower furnace and it is stretched using the fiber coiling drum to obtain the target MOF. The diameter of the fiber and, thus, the period of the microstructure Λ is controlled by the preform feeding speed and the drawing speed. According to the lattice period, an additional silica jacket might be necessary to obtain fibers with a diameter compatible with the available optical fiber devices. During the fiber drawing stage, the pressure inside the holes is controlled by pumping an inert gas, typically N_2. This is done to avoid the collapse of the air holes due to the radial force induced by surface tension when the silica has reached the plastic deformation temperature.

The fiber coating is applied at a later stage after the fibers are manufactured. An acrylate fiber coating, UV curable is used. The polymer coating is added to the fiber in a pulling fiber rig that includes the polymer applicator and an UV lamp. The end of the fiber is removed from the spool drum where it was coiled in fiber fabrication stage, let the fiber pass through a pin hole base with a diameter of 250 μm. On this base the polymer is applied, and then the fiber coated with uncured polymer passes through the UV lamp located after the polymer applicator in order to cure the polymer. Finally, the fiber is wound onto a fiber reel.

We would like to emphasize that this fabrication method allows us to obtain several families of MOFs from a given preform. For example, by applying pressure to the holes, their diameter can be controlled and, therefore, several families of MOFs with different air-filling ratio at a fixed lattice period can be fabricated. On the other hand, the lattice period can be controlled by slightly adjusting the diameter of the fiber.

3.2.3 Fabricated MOFs

During this research project several MOFs were fabricated to carry out the experiments for the generation of FWM. In this section, we summarize the type of fiber used throughout this thesis. In particular, three families of MOFs were fabricated with different dispersion properties: (1) MOFs exhibiting all-normal dispersion (ANDi) over a wide wavelength range, (2) MOFs with low normal dispersion at the experimental pump wavelength, and (3) MOFs with anomalous dispersion.

(i) ANDi MOFs

ANDi fibers were fabricated to investigate the generation of vector-FWM processes. In fibers with such chromatic dispersion, scalar cases of FWM are forbidden and only vector-FWM can be produce. As a reference, the structural parameters required to obtain single-mode air-filled MOFs with ANDi profile are approximately $\Lambda \sim 1.0$ μm, and $d/\Lambda \sim 0.5$. Such small dimensions, with hole diameter in the nm scale, demand tight control of the fiber fabrication conditions. Due to the small pitch and moderate air-filling fraction, confinement losses is an important issue in this fibers [41]. In order to reduce it to practical levels, the ANDi MOFs were fabricated with 7 hexagonal ring periods of air holes. Figure 3.6 shows cross-section images of two ANDi fibers obtained with a scanning electron microscope (SEM).

The structural parameters of the fabricated MOFs are measured from SEM images with an accuracy of 5%.

(ii) Low normal dispersion and anomalous dispersion MOFs

To explore the generation of scalar/vector FWM spectral sidebands in both dispersion regimes, two families of MOFs were fabricated. In the first case, air-filled MOFs with low normal dispersion at the experimental pump wavelength (λ=1064 nm) were fabricated. The structural parameters of fibers fabricated with this dispersion feature ranged from Λ~2.5 μm to Λ~4.0 μm, with d/Λ from ~0.35 to ~0.5. Figure 3.7 (a) shows the SEM image of the cross-section of an air-filled MOF with low normal dispersion and five periods. In particular, the dispersion of this fiber at 1064 nm was -3.1 ps/km-nm.

In this thesis, we have carried out experiments intended to the generation of scalar and vector FWM in MOFs with the holes filled with different optical liquids. The dispersion requirements for these fibers to produce such effects must be fulfilled once the fiber was infiltrated with the liquid. So, the fibers were designed following this criterion. Since the refractive indices of the filling liquids are higher than that of air (approximately n_{liquid}~1.3), the designed MOFs resulted with larger air-filling fractions (d/Λ~0.6). These fibers exhibited anomalous dispersion at the experimental pump wavelength before the fiber was infiltrated with the liquid, and the required normal dispersion after infiltration of the liquid into the fiber holes. Figure 3.7 (b) shows the SEM image of the cross section of an air-filled MOF with anomalous dispersion that was used for such experiments.

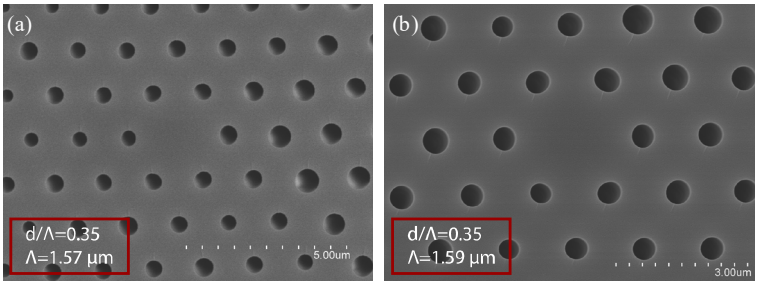

Figure 3.6. SEM images of the cross-section of ANDi MOFs. The inset shows the structural parameters of the fibers.

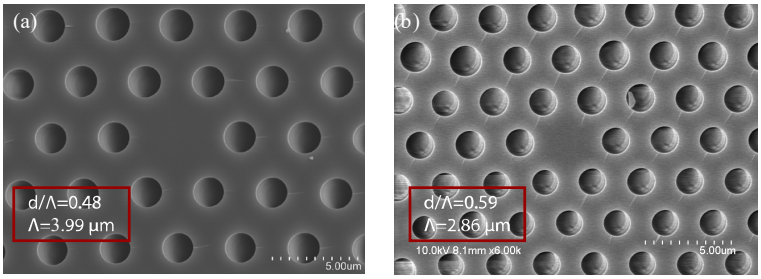

Figure 3.7. SEM images of the cross section of MOFs with (a) low normal dispersion and (b) anomalous dispersion. The inset shows the structural parameters of the fibers.

3.3 Experimental procedures

3.3.1 Experimental setup

Fig. 3.8 shows the general experimental setup used throughout this work for exciting and characterizing FWM sidebands produced in MOFs. The experimental arrangement comprises of a diode-pumped passively Q-switched Nd: YAG microchip laser (TEEM Photonics SNP-20F-100) that emits pulses at 1064 nm wavelength of 700 ps duration (FWHM), peak power of ~ 11 kW, and a repetition rate of 19.1 kHz. This laser was used as the pump for the nonlinear experiments. The spectral bandwidth is narrower than 30 pm (FWHM). Inset of Fig. 3.8 shows

the temporal shape of the pump pulses. The laser emission is linearly polarized, with a polarization extinction (PER) of 32 dB. A half-wave plate (HWP) was positioned at the laser output, in order to rotate the polarization plane of the launched pump beam with respect to the fiber principal axes. The pump beam was launched into the fibers under test (FUT). An XYZ alignment stage and aspheric lenses of different focal length were used to launch the laser beam into the FUT, with an efficiency ranging from 40-50 % depending on the fiber. The typical fiber length used in the experiments was ~1 m.

A linear polarizer was used in most of the experiments to characterize the polarization state of the output light. The light leaving the FUT at the tip end was collected and recorded with an optical spectrum analyzer (OSA) (Yokogawa AQ6370C), typically with a spectral resolution of 0.2 nm. The optical power transmitted through the FUT was measured with a power meter (PM). According to each experiment, the MOFs were subjected to different physical tests (e.g., axial tension, bending, heat), and, therefore, minor modifications in the experimental setup had to be addressed.

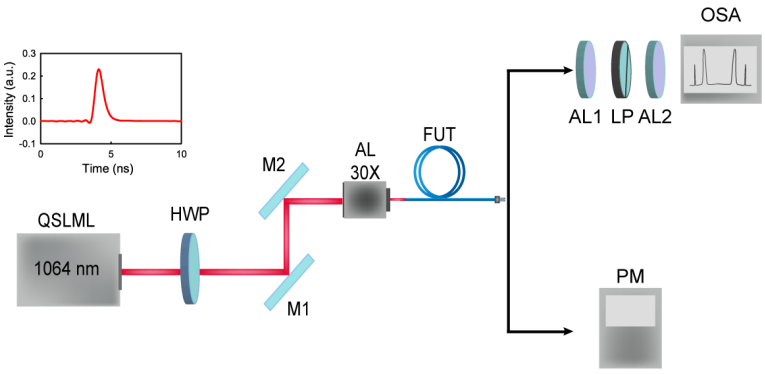

Figure 3.8. Experimental arrangement. QSLML: Pump laser; HWP: half-wave plate; M1 and M2: dichroic mirrors; FUT: fiber under test; AL: aspheric lens (x30); LP: linear polarizer; MMF: multimode collecting fiber; OSA: optical spectrum analyzer. Inset shows the temporal shape of the pump pulses.

3.3.2 Liquid infiltration technique for MOFs

In many of the experiments of this thesis, we require fine tuning of the chromatic dispersion of a MOF to control the spectral position of the FWM sidebands. In MOFs with air-filled holes, the dispersion is fixed by their structural parameters and there is no relevant contribution to the fiber dispersion by inducing changes in the optical properties of the fused silica through a physical quantity (e.g., heat, strain, pressure). However, when the fiber holes are filled with a substance with suitable optical properties, an additional degree of freedom is obtained to adjust the fiber dispersion at a post-fabrication stage. In particular, we used heavy water, pure ethanol, and ethanol-water mixtures to effectively adjust the dispersion of the MOFs.

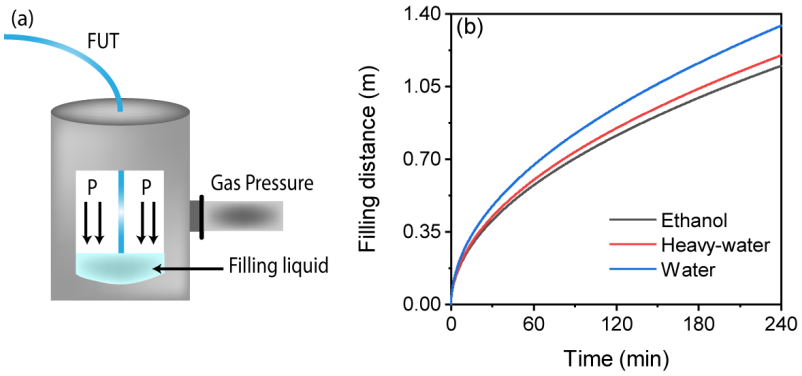

Figure 3.9. (a) Schematic diagram for liquid MOF filling by gas pressure. (b) Filling distance as a function of time of a capillary with hole diameter of 1.5 μm when filled with water (blue) and ethanol (red).

The infiltration of such liquids into the holes of a MOF was performed by capillary force and gas pressure. A tip of the fiber was placed in a pressure chamber inside the filling liquid, as shown in the schematic in Fig. 3.9 (a). By applying gas (N_2) pressure (about 8 bar) to the chamber, the liquid flows into the holes of the

fiber and after a certain time the liquid reaches the outer tip of the fiber. To calculate the time needed to fill a MOF of length ~1 m we have followed the theoretical modeling reported in [42], which describes the filling rate of a capillary of a few micrometers in diameter when liquids with viscosity and surface tensions similar to water are infiltrated through pressure. Figure 3.9 (b) shows the filling distance as a function of time for a MOF with 1.5 μm diameter holes. Typically, it took 4 hours to completely fill the holes of most of the MOFs employed for this thesis.

References

1. J. C. Knight, "Photonic crystal fibres," Nature **424**, 847–851 (2003).

2. J. C. Knight, T. A. Birks, P. S. J. Russell, and D. M. Atkin, "All-silica single-mode optical fiber with photonic crystal cladding," Opt. Lett. **21**, 1547 (1996).

3. T. M. Monro, K. M. Kiang, J. H. Lee, K. Frampton, Z. Yusoff, R. Moore, J. Tucknott, D. W. Hewak, H. N. Rutt, and D. J. Richardson, "High nonlinearity extruded single-mode holey optical fibers," in *Conference on Optical Fiber Communication, Technical Digest Series* (2002), Vol. 70.

4. V. V. R. Kumar, A. George, W. Reeves, J. Knight, P. Russell, F. Omenetto, and A. Taylor, "Extruded soft glass photonic crystal fiber for ultrabroad supercontinuum generation," Opt. Express **10**, 1520 (2002).

5. B. Temelkuran, S. D. Hart, G. Benoit, J. D. Joannopoulos, and Y. Fink, "Wavelength-scalable hollow optical fibres with large photonic bandgaps for CO2 laser transmission," Nature **420**, 650–653 (2002).

6. M. van Eijkelenborg, M. Large, A. Argyros, J. Zagari, S. Manos, N. Issa, I. Bassett, S. Fleming, R. McPhedran, C. M. de Sterke, and N. A. P. Nicorovici, "Microstructured polymer optical fibre," Opt. Express **9**, 319 (2001).

7. P. S. J. Russell, D. M. Atkin, T. A. Birks, and P. J. Roberts, Chapter: Bound Modes of Two-Dimensional Photonic Crystal Waveguides. In, Rarity, J.G. and Weisbuch, C. (eds) *Quantum Optics in Wavelength Scale Structures*. Kluwer Academic Press, 203–218 (1996).

8. F. Luan, A. K. George, T. D. Hedley, G. J. Pearce, D. M. Bird, J. C. Knight, and P. S. J. Russell, "All-solid photonic bandgap fiber," Opt. Lett. **29**, 2369 (2004).

9. R. F. Cregan, B. J. Mangan, J. C. Knight, T. A. Birks, P. S. J. Russell, P. J. Roberts, and D. C. Allan, "Single-mode photonic band gap guidance of light in air," Science (80-.). **285**, 1537–1539 (1999).

10. J. C. Knight, T. A. Birks, R. F. Cregan, P. S. J. Russell, and J. P. De Sandro, "Large mode area photonic crystal fibre," Electron. Lett. **34**, 1347–1348 (1998).

11. T. A. Birks, J. C. Knight, and P. J. St Russell, "Endlessly single-mode photonic crystal fiber," Opt. Lett. **22**, 961 (1997).

12. A. Ferrando, E. Silvestre, J. J. Miret, and P. Andrés, "Nearly zero ultraflattened dispersion in photonic crystal fibers," Opt. Lett. **25**, 790 (2000).

13. J. K. Ranka, R. S. Windeler, and A. J. Stentz, "Visible continuum generation in air–silica microstructure optical fibers with anomalous dispersion at 800 nm," Opt. Lett. **25**, 25 (2000).

14. W. Reeves, J. Knight, Ps. Russell, and P. Roberts, "Demonstration of ultra-flattened dispersion in photonic crystal fibers," Opt. Express **10**, 609 (2002).

15. A. Ortigosa-Blanch, A. Díez, M. Delgado-Pinar, J. L. Cruz, and M. V. Andrés, "Ultrahigh birefringent nonlinear microstructured fiber," IEEE Photonics Technol. Lett. **16**, 1667–1669 (2004).

16. K. Saitoh and M. Koshiba, "Highly nonlinear dispersion-flattened photonic crystal fibers for supercontinuum generation in a telecommunication window," Opt. Express, Vol. 12, Issue 10, pp. 2027-2032 **12**, 2027–2032 (2004).

17. N. Ayyanar, G. Thavasi Raja, Y. S. Skibina, Y. E. Monfared, A. A. Zanishevskaya, A. A. Shuvalov, and G. A. Yu, "Hollow-Core Microstructured Optical Fiber Based Refractometer: Numerical Simulation and Experimental Studies," IEEE Trans. Nanobioscience 1–1 (2022).

18. R. Otupiri, E. K. Akowuah, and S. Haxha, "Multi-channel SPR biosensor based on PCF for multi-analyte sensing applications," Opt. Express **23**, 15716 (2015).

19. M. Biplob Hossain, M. Shafayet Hossain, S. M. Riazul Islam, M. Nazmus Sakib, K. Ziaul Islam, M. Amzad Hossain, M. Sanwar Hossain, A. S. M. Sanwar Hosen, and G. Hwan Cho, "Numerical development of high performance quasi D-shape PCF-SPR biosensor: An

external sensing approach employing gold," Results Phys. **18**, 103281 (2020).

20. Y. Yu, X. Li, X. Hong, Y. Deng, K. Song, Y. Geng, H. Wei, and W. Tong, "Some features of the photonic crystal fiber temperature sensor with liquid ethanol filling," Opt. Express **18**, 15383 (2010).

21. S. H. Kassani, R. Khazaeinezhad, Y. Jung, J. Kobelke, and K. Oh, "Suspended ring-core photonic crystal fiber gas sensor with high sensitivity and fast response," IEEE Photonics J. **7**, (2015).

22. G. Sobon, M. Klimczak, J. Sotor, K. Krzempek, D. Pysz, R. Stepien, T. Martynkien, K. M. Abramski, and R. Buczynski, "Infrared supercontinuum generation in soft-glass photonic crystal fibers pumped at 1560 nm," Opt. Mater. Express **4**, 7 (2014).

23. Z. Du, Y. Zhou, S. Luo, Y. Zhang, J. Shao, Z. Guan, H. Yang, and D. Chen, "Highly birefringent hollow-core anti-resonant terahertz fiber with a thin strut microstructure," Opt. Express **30**, 3783 (2022).

24. G. K. M. Hasanuzzaman, S. Rana, and M. S. Habib, "A Novel Low Loss, Highly Birefringent Photonic Crystal Fiber in THz Regime," IEEE Photonics Technol. Lett. **28**, 899–902 (2016).

25. J. C. Knight, T. A. Birks, P. S. J. Russell, and J. P. de Sandro, "Properties of photonic crystal fiber and the effective index model," J. Opt. Soc. Am. A **15**, 748 (1998).

26. M. Koshiba and K. Saitoh, "Applicability of classical optical fiber theories to holey fibers," Opt. Lett. **29**, 1739 (2004).

27. K. Saitoh and M. Koshiba, "Empirical relations for simple design of photonic crystal fibers," Opt. Express **13**, 267 (2005).

28. Y. F. Li, C. Y. Wang, and M. L. Hu, "A fully vectorial effective index method for photonic crystal fibers: Application to dispersion calculation," Opt. Commun. **238**, 29–33 (2004).

29. A. Ferrando, E. Silvestre, J. J. Miret, P. Andrés, and M. V. Andrés, "Full-vector analysis of a realistic photonic crystal fiber," Opt. Lett. **24**, 276 (1999).

30. K. Saitoh and M. Koshiba, "Full-vectorial imaginary-distance beam propagation method based on a finite element scheme: Application to photonic crystal fibers," IEEE J. Quantum Electron. **38**, 927–933 (2002).

31. F. Brechet, J. Marcou, D. Pagnoux, and P. Roy, "Complete Analysis of the Characteristics of

Propagation into Photonic Crystal Fibers, by the Finite Element Method," Opt. Fiber Technol. **6**, 181–191 (2000).

32. S. Johnson and J. Joannopoulos, "Block-iterative frequency-domain methods for Maxwell's equations in a planewave basis," Opt. Express **8**, 173 (2001).

33. K. Okamoto, *Fundamentals of Optical Waveguides* (Elsevier Inc., 2006).

34. M. Koshiba and K. Saitoh, "Applicability of classical optical fiber theories to holey fibers," Opt. Lett. **29**, 1739 (2004).

35. T. A. Birkst, D. Mogilevtsev, J. C. Knight, P. S. J. Russell, J. Broeng, P. J. Roberts, J. A. West, D. C. Allan, and J. C. Fajardo, "The analogy between photonic crystal fibres and step index fibres," in *OFC/IOOC 1999 - Optical Fiber Communication Conference and the International Conference on Integrated Optics and Optical Fiber Communication* (Optica Publishing Group, 1999), Vol. 4, pp. 114–116.

36. T. P. White, R. C. McPhedran, C. M. de Sterke, L. C. Botten, and M. J. Steel, "Confinement losses in microstructured optical fibers," Opt. Lett. **26**, 1660 (2001).

37. E. Silvestre, T. Pinheiro-Ortega, P. Andrés, J. J. Miret, and A. Ortigosa-Blanch, "Analytical evaluation of chromatic dispersion in photonic crystal fibers," Opt. Lett. **30**, 453 (2005).

38. K. N. Park and K. S. Lee, "Improved effective-index method for analysis of photonic crystal fibers," Opt. Lett. **30**, 958 (2005).

39. H. Ebendorff-Heidepriem and T. M. Monro, "Extrusion of complex preforms for microstructured optical fibers," Opt. Express **15**, 15086 (2007).

40. G. Barton, M. A. Van Eijkelenborg, G. Henry, M. C. J. Large, and J. Zagari, "Fabrication of microstructured polymer optical fibres," Opt. Fiber Technol. **10**, 325–335 (2004).

41. D. M. Atkin, J. C. Knight, P. S. J. Russell, and T. A. Birks, "All-silica single-mode optical fiber with photonic crystal cladding: errata," Opt. Lett. Vol. 22, Issue 7, pp. 484-485 **22**, 484–485 (1997).

42. K. Nielsen, D. Noordegraaf, T. Sørensen, A. Bjarklev, and T. P. Hansen, "Selective filling of photonic crystal fibres," J. Opt. A Pure Appl. Opt. **7**, L13–L20 (2005).

Chapter 4

Polarization Modulation Instability

In the present chapter we will describe in detail the nonlinear effect of polarization modulation instability (PMI) in optical fibers. We report our results on the generation of PMI in weakly birefringent solid-core MOFs. The study addresses PMI generation in MOFs with different chromatic dispersion profiles, paying attention to the dependence of PMI on fiber dispersion. We report the experimental study of PMI effect that was investigated in a wide collection of air-filled, ethanol-filled, and heavy-water-filled MOFs with different structural parameters and dispersion characteristics, including all-normal dispersion (ANDi) fibers, and fibers with one, or two zero dispersion wavelengths. Theoretical simulations of PMI in those fibers is also included.

This chapter is organized as follows: First, PMI in optical fibers and its main physical aspects and characteristics are described for air-filled and liquid-filled solid core MOFs. In section 4.2, a detailed experimental study of PMI in air-filled ANDi MOFs with different dispersion characteristics is given, the characterization of the polarization of PMI sidebands is addressed. In section 4.3, the frequency shift of PMI in a large collection of liquid-filled MOFs with different chromatic dispersion characteristics at the pump wavelength is studied experimentally.

4.1 General aspects of PMI

In the context of optical fibers, PMI is a nonlinear parametric process that affects the polarization state of light that propagates through the fiber [1–3]. Our work focuses on degenerate PMI in optical fibers, in which two photons of the same frequency with linear polarization oriented to one of the principal fiber axes are annihilated to give rise to two new photons with different frequencies, same linear polarization state, but orthogonal with respect to pump photons. In single-mode optical fibers, PMI is generated through the coherent coupling of the two polarized eigenmodes HE_{11x} and HE_{11y}, whose propagation factors are slightly different due to unintentional residual linear birefringence present in the fiber. Typical values of residual phase-birefringence, Δn, of non-polarization maintaining fibers are in the order of 10^{-7} - 10^{-5}. It is worth to mention that PMI effect also can occur in isotropic fibers with almost zero birefringence [4].

Some remarkable aspects of this nonlinear effect are: (i) the polarization state of the light generated through PMI is orthogonal to the polarization state of the pump signal, (ii) modulation instability can occur even when the fiber is pumped in the normal dispersion regime, and (iii) the contribution of the phase birefringence to the linear phase mismatch plays a major role in the phase-matching condition. In addition, PMI features in optical fibers are quite different depending on the polarization of the pump, in particular for linear polarization, on whether the pump is polarized along the slow or the fast axis of the fiber. Figure 4.1 shows an example of the gain profile of PMI for both, slow- or fast-axis excitation. In the first case (slow-axis pumping), PMI generates detuned sidebands separated from the pump frequency from low pump power levels (see Fig. 4.1 (a)). For fast-axis pumping, a low-power threshold (P_{Th}) exists. Recalling from Chapter 2, the power threshold is given by,

$$P_{Th} = \frac{3 \cdot \Delta n \cdot A_{eff}}{2 \cdot n_2} \qquad (4.1)$$

where Δn is the fiber birefringence, $Aeff$ is the effective mode area, and n_2 is the nonlinear refractive index.

PMI can be generated when the pump power $P_0 > P_{Th}$, the gain profile only shows sidebands detuned from the pump when $P_0 > 2 \cdot P_{Th}$, nevertheless, the gain at zero detuning does not vanish regardless of the pump power level, as shown in Fig. 4.1 (b). Additionally, in Fig 4.1(a) it can be observed that the peak gain of PMI sidebands for slow-axis pump shifts slightly with pump power.

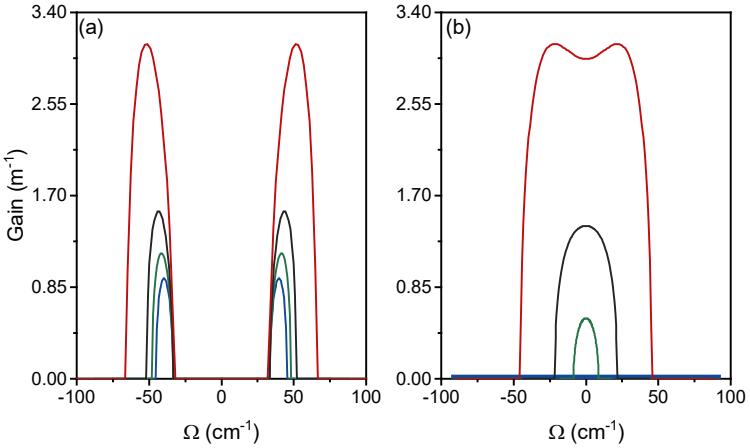

Figure 4.1. Gain profile of PMI sidebands produced by (a) slow-axis pump and (b) fast-axis pump, for different pump power levels: $0.85 \cdot P_{Th}$ (blue line), $1.1 \cdot P_{Th}$ (green line), $1.5 \cdot P_{Th}$ (black line) and $3 \cdot P_{Th}$ (red line). $P_{Th}=70$ *W*. Calculations are done for the fiber reported in [2].

One of the motivations of this thesis was to investigate the potential of PMI as a physical mechanism to generate few-wavelength light sources based on optical fibers. Generation of light spectral bands well separated in wavelength from the pump was aimed for this type of application. According to the main properties of PMI, the option consisting of pumping with a linearly polarized beam with

polarization oriented along the slow axis of the fiber satisfies this criterion to a greater extent. Thus, the work carried out in this thesis related to PMI was mainly focused on this pump option. Hereinafter, when PMI effect is mentioned it will refer to the specific case of slow-axis PMI.

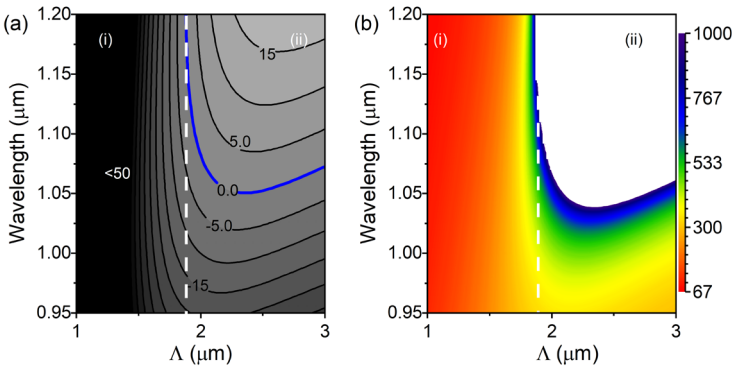

Figure 4.2. (a) Chromatic dispersion as a function of wavelength and fiber pitch for air-filled MOFs. Numbers indicates dispersion levels in ps/km·nm. White dashed line indicates pitch of 1.8 Λ μm. (b) Frequency shift map of PMI; color bars are detuning frequency values in cm^{-1}. Parameters used in the simulations: $d/\Lambda = 0.36$, $P_0 = 3$ *kW*.

Frequency detuning of PMI sidebands strongly depends on the fiber birefringence, but also on the chromatic dispersion of the fiber, which becomes particularly notable for low values of dispersion [3]. The chromatic dispersion of air-filled MOFs can be tailored through the design of the fiber structural parameters. Several combinations of d and Λ can be suitable for attaining given dispersion requirements. Figure 4.2(a) shows the theoretical calculation of chromatic dispersion for air-filled MOFs, as a function of the optical wavelength and the fiber pitch. The linear properties of the fibers were calculated using the full-vector method described in Chapter 3. A fixed value of $d/\Lambda = 0.36$ was used in these simulations. The blue level curve in Fig. 4.2(a) indicates zero of dispersion. For this particular air-filling fraction, we can distinguish two different dispersion regimes: (i) when $\Lambda < 1.8$ μm, the dispersion is normal over a wide wavelength range, MOFs presenting such

dispersion profile are commonly named as ANDi fiber. (ii) When $\Lambda > 1.8$ μm, the dispersion profile shows at least one ZDW. In the first regime, fibers with Λ approaching 1.8 μm shows low dispersion values within the wavelength range under study, and decreasing significantly as Λ becomes smaller.

According with the dispersion features described above, the dependence of PMI phase-matching condition on chromatic dispersion is theoretically investigated. The PMI parametric wavelengths (Stokes and anti-Stokes) were obtained by solving numerically Eq. 2.68 together with the energy conservation condition. Figure 4.2 (b) shows a frequency shift map of the PMI process as a function of the optical pump wavelength and fiber pitch. Additional parameters used in PMI simulation are the following: pump power of $P_0 = 3\ kW$, phase birefringence $\Delta n = 10^{-6}$, and nonlinear refractive index $n_2 = 2.7 \cdot 10^{-20}\ m^2/W$. In the case of ANDi fibers, i.e., dispersion region (i), PMI is generated in all cases. For low Λ values, the frequency shift is relatively small, and it shows small dependence on the pump wavelength. The frequency shift increases with increasing the fiber pitch, and/or the dispersion at the pump wavelength increases. In dispersion region (ii), the result is more complex. For Λ slightly above 1.8 μm and pump wavelengths in which the dispersion is higher and near to zero (pump wavelength near to λ_{ZDW}), PMI experiences a large frequency shift. Additionally, there is a forbidden region (white region in Fig. 4.2 (b)) where no phase-matching solutions for PMI can exist.

In fibers exhibiting both, anomalous and normal dispersion regimes, PMI presents a cut-off wavelength, beyond which the phase-matching condition is no longer fulfilled. This occurs when the dispersion mismatch together with the contribution of nonlinear mismatch cannot compensate the term of phase-birefringence of the phase-matching condition. Physically, the maximum pump wavelength or cut-off of PMI occurs when the group velocity of the anti-Stokes photon matches with the group velocity of the Stokes photons [5]. In this case, the

group index (n_g) of the Stokes and anti-Stokes photons satisfies the following expression,

$$\frac{\partial n(\omega)}{\partial \omega}\Big|_{\omega=\omega_S} \cdot \omega_S + n(\omega_S) = \frac{\partial n(\omega)}{\partial \omega}\Big|_{\omega=\omega_{AS}} \cdot \omega_{AS} + n(\omega_{AS}) \qquad (4.2)$$

where n is the effective mode index and ω_S and ω_{AS} are the frequencies of the Stokes and anti-Stokes photons, respectively.

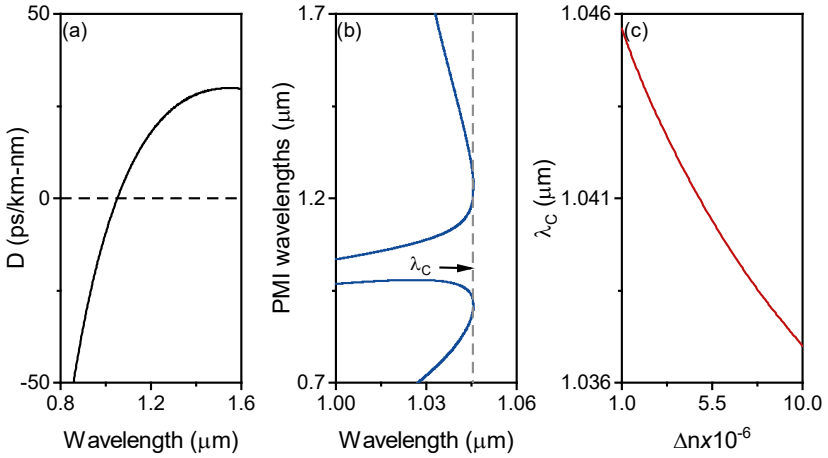

Figure 4.3. (a) Chromatic dispersion as a function of wavelength. (b) PMI wavelengths as a function of pump wavelength. In the simulation was assumed a pump power of $P_0 = 1$ *kW* and fiber birefringence of $\Delta n = 10^{-6}$, the vertical dashed line indicates the cut-off wavelength. (c) Cut-off wavelengths as a function of phase-birefringence.

In order to give some physical insights of the cut-off wavelength of PMI, we calculated the maximum pump wavelength at which PMI can occur for a given air-filled MOF with d/Λ=0.36 and Λ=2.5 μm. The chromatic dispersion for this fiber is shown in Fig. 4.3 (a). The simulations results shown a λ_{ZDW} = 1051 nm for this fiber. The calculated phase-matching curves of PMI are shown in Fig. 4.3 (b). For calculations of PMI wavelengths, we considered a pump power of $P_0 = 1$ *kW* and a phase-birefringence of $\Delta n = 10^{-6}$, the cut-off wavelength (λ_C) of PMI occurs at

λ_C = 1045 nm, as depicted by the vertical dashed line in Fig 4.3 (b). No solutions for PMI phase-matching were found for wavelengths $\lambda_P > \lambda_C$.

The dependence of PMI cut-off on the fiber birefringence is studied. The cut-off wavelength as a function of phase birefringence was calculated using Eq. 4.2 together with the PMI phase-matching condition (Eq. 2.68). Figure 4.3 (c) shows the cut-off wavelengths when varying the birefringence from 10^{-6} to 10^{-5}. It can be observed that λ_C varies smoothly with birefringence and shifts to shorter wavelengths when increasing the fiber birefringence. This indicates that residual fiber birefringence not only contributes to the PMI frequency shift, but also it determines the largest pump wavelength at which this nonlinear effect can be generated in an optical fiber.

It is known that the dispersion of a standard MOF is not only designated by the refractive index of fused silica, but is also due to the geometry of the microstructure itself. Therefore, great flexibility in MOF chromatic dispersion fabrication designs can be achieved. However, the dispersion of the pristine fibers cannot be easily modified after fabrication. Filling the holes with optical materials has been demonstrated to be a useful post-fabrication technique for changing the guiding properties of MOFs. Additionally, it enables fine tuning of the chromatic dispersion by exploiting the optical sensitivity of the filling materials with external parameters, as, for example, temperature. In this thesis, several experiments were performed using such hybrid MOFs. Furthermore, several applications related to the nonlinear properties of liquid-filled MOFs have been reported in the past [6–8].

We extended the theoretical study on the general aspects of PMI to solid-core MOFs with holes filled with ethanol (EtOH) and with heavy-water (D_2O). Following the procedure described above, the linear properties of the fibers were first calculated using a fully-vector method described in Chapter 3. Then, PMI parametric wavelengths (Stokes and anti-Stokes) were calculated numerically. When filling the

holes of a MOF with materials different from air, the chromatic dispersion of the filled fiber changes with respect to the dispersion of the pristine fiber. This occurs due to the increase of the refractive index in the fiber microstructure, and the dispersion properties of the filling material itself. For our experiments, we chose EtOH and D_2O owing to their refractive index (lower than silica) and relative low absorption in the infrared region. Refractive index characteristics of both liquids used for the theoretical simulations are taken from [9]. The wavelength dependence on the refractive index of EtOH and D_2O was taken into account in the calculations.

Figure 4.4 (a) and 4.5 (a) show dispersions maps calculated for fibers filled with EtOH and D_2O, respectively. A value of $d/\Lambda = 0.56$ was chosen for D_2O-filled fibers, and $d/\Lambda = 0.58$ for EtOH-filled fibers. These parameters correspond to the mean values of structural parameters of fibers used in the experiments.

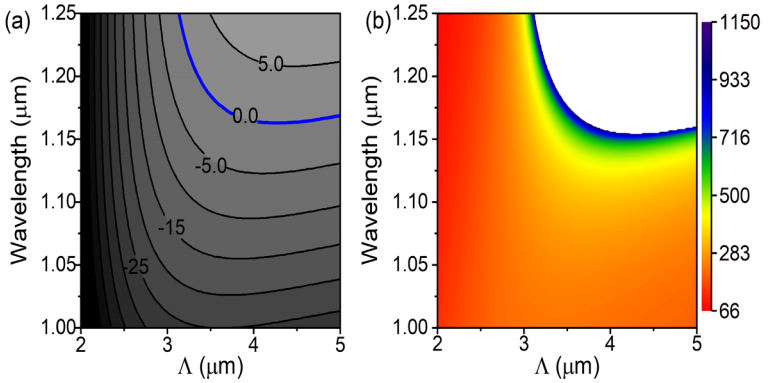

Figure 4.4. (a) Chromatic dispersion as a function of optical wavelength and fiber pitch for EtOH-filled MOFs. Numbers indicates dispersion levels in ps/km·nm. (b) Frequency shift map of PMI; color bars are detuning frequencies values in cm^{-1}. Parameters used in the simulations: $d/\Lambda=0.58$. $P_0=3$ *kW*.

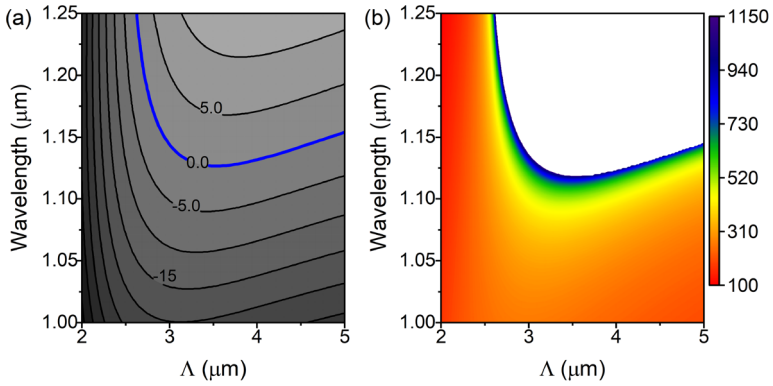

Figure 4.5. (a) Chromatic dispersion as a function of optical wavelength and fiber pitch for D_2O-filled MOFs. Numbers indicates dispersion levels in ps/km·nm. (b) Frequency shift map of PMI; color bars are detuning frequencies values in cm^{-1}. Parameters used in the simulations: $d/\Lambda=0.56$. $P_0=3$ *kW*.

When holes in the same MOF are filled with either D_2O or EtOH it results in large dispersion differences due to the different refractive index of these substances, therefore, the comparison between the PMI frequency shift maps of EtOH and D_2O filled MOFs is inadequate for fibers with same air-filling fractions and pitch lengths. In order to provide a clear view of the dispersion and frequency shift maps of PMI in EtOH-filled and D_2O -filled MOFs, the air-filling fraction used in the calculations was assumed to be slightly different, while the considered pitch length range was within the pitch lengths of the fibers used in the experiments.

According with the air-filling fraction used for dispersion maps of the EtOH-filled and D_2O-filled MOFs, two dispersion regimes can be observed (similarly to those previously described with air-filled MOFs). When $\Lambda < 3.1$ μm and $\Lambda < 2.6$ μm for EtOH-filled and D_2O-filled MOFs, respectively, all-normal dispersion is observed. In contrast, when Λ is larger than those values, dispersion profile shows at least one ZDW, in both cases. Figure 4.4 (b) and 4.5 (b) show the corresponding frequency shift maps for PMI. The shift of zero dispersion that EtOH-filled and D2O-filled fibers exhibit also causes the movement of the forbidden region of PMI

to longer wavelengths and larger pitch lengths. As in the case of air-filled MOFs described in the previous section, larger frequency shift occurs as the dispersion at the pump wavelength approaches the zero value. It can be seen that PMI frequency detuning is small when the dispersion is large and when the fiber shows an ANDi profile.

4.2 PMI in ANDi-MOFs with air holes

An ANDi MOF is a fiber whose dispersion remains normal in wide wavelength range. In the last years, the potential of ANDi MOFs as nonlinear media has been widely investigated. Most of the interest on ANDi fibers comes from their ability for the generation of coherent, octave-spanning, and re-compressible supercontinuum (SC) light [10–13]. In ANDi fibers the noise induced by MI/FWM to an optical pulse is suppressed since the phase matching condition is not accomplish because the linear phase mismatch cannot compensate for the nonlinear term for any wavelength. [11]. In recent works, however, it was found that polarization induced noise can degrade the coherence of ANDi femtosecond supercontinuum [14, 15]. PMI assisted by the weak unintentional birefringence of the fibers has been identified as the origin of such coherence degradation. Here, we report the experimental investigation of PMI effect in weakly birefringent ANDi MOFs with quasi-CW pumping at 1064 nm. As mentioned above, PMI in ANDi MOFs has been observed previously in the femtosecond pump regime. We investigated this effect using long pump pulses, (essentially, a quasi-continuous pump), as the nonlinear dynamic of PMI is somewhat different.

First, we investigated theoretically the different vector FWM processes that can occur in a weakly-birefringent ANDi MOF with $\Lambda = 1.5\ \mu m$, $d/\Lambda = 0.42$. Figure 4.6 (a) shows the chromatic dispersion of the fiber, it can be seen that the fiber dispersion exhibits a convex profile with an all-normal dispersion within the

wavelength range of study. The maximum of the dispersion curve (MDW) happens at *1060 nm*, with a value of dispersion of *8 ps/nm·km*. The phase-matching equations and the energy conservation relation were used to calculate the spectral shift between the pump wavelength and the parametric wavelengths. Figure 4.6 (b) and (c) shows the parametric wavelengths as a function of pump wavelength, for different pump powers. Linearly polarized light with polarization orientation aligned to the principal axes of the fiber, fast and slow, was considered.

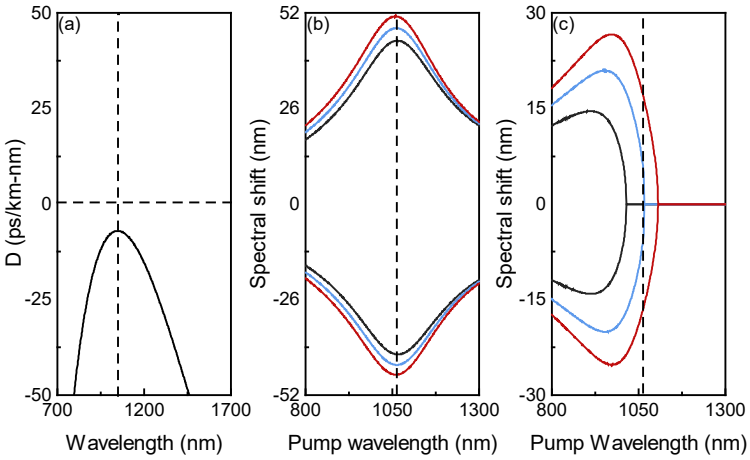

Figure 4.6. (a) Chromatic dispersion vs. wavelength for a weakly birefringent MOF. Parametric wavelengths for (b) slow-axis pumping PMI, and (c) fast-axis pumping PMI at different pump powers, P0 = 1.5·PTh (black), P0 = 2·PTh (blue), and P0 = 2.5·PTh (red), being PTh = 2.6 kW. Fiber parameters: Λ = 1.5 μm, d/Λ = 0.42, Δn = 1×10−6. Vertical dashed line indicates the MDW (1060 nm).

As expected, no solutions were found for scalar FWM/MI, only PMI effect can occur in such fibers. In the case of slow-axis pumping PMI (see Fig. 4.6 (b)), the largest wavelength shift is obtained when the fiber is pumped at the wavelength that matches the MDW. The closer is the dispersion to zero at the MDW, the wider is the wavelength spacing of the PMI sidebands for that pump wavelength. The calculated bands for slow-axis pump shift slightly with pump power. The results for

fast-axis pump PMI are somehow more complex (see Fig. 4.6 (c)). In the parametric calculations we considered $P_{Th} = 2.6\ kW$ as constant. It is known that P_{Th} increases with increasing the wavelength, since effective mode area increases in the same fashion. Therefore, a cutoff for fast-axis PMI occurs for certain wavelengths when the condition $P_0 > 2 \cdot P_{Th}$ is not accomplished, as shown in Fig. 4.6 (c).

4.2.1 MOFs characteristics

A range of air-filled MOFs were designed and fabricated to present a convex-ANDi profile in a broad wavelength range. Figure 4.7 (b) shows the scanning electronic microscope (SEM) images of the cross section of the fibers used in the experiments. The structural parameters of the fibers were obtained from the SEM images and are summarized in Table 4.1. Figure 4.7 (a) shows the chromatic dispersion as a function of wavelength of the studied ANDi-MOFs. Table 4.1 also includes the theoretical calculations of dispersion values, MDW, and effective mode area of the fundamental mode at 1064 nm. In most of the fibers, the MDW is close to the experimental wavelength and has a relatively small dispersion value (close to the zero of dispersion). In contrast, large normal dispersion at the pump wavelength is observed in A-MOF1 and the MDW was estimated at a shorter wavelength.

Table 4.1 Characteristics of air-filled fibers.

Fiber	Λ (μm)	d/Λ	D (ps/nm km)†	MDW (μm)	A_{eff} (μm²)†
A-MOF1	1.0	0.52	-100	0.836	9.4
A-MOF2	1.57	0.35	-19.9	1.049	7.2
A-MOF3	1.59	0.35	-20.8	1.054	7.5
A-MOF4	1.60	0.36	-11.5	1.07	6.7
A-MOF5	1.57	0.37	-13.1	1.058	6.5

†calculated at 1064 nm

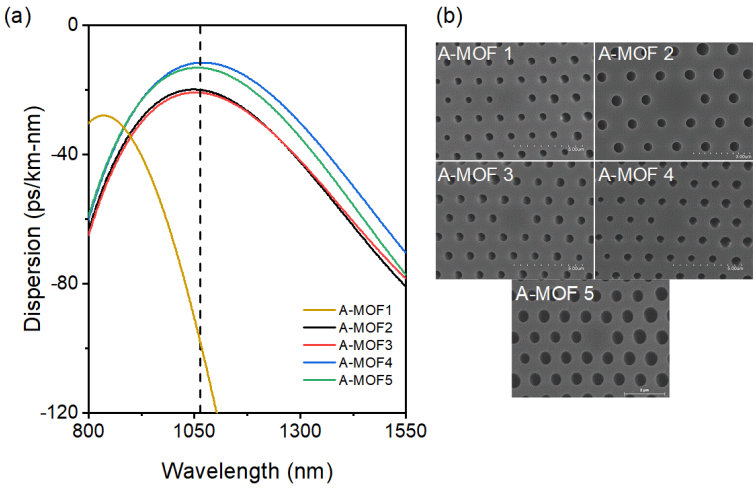

Figure 4.7. (a) Chromatic dispersion of air-filled MOFs. Dashed vertical black line indicates the experimental pump wavelength. (b) SEM images of air-filled MOFs cross-section.

4.2.2 Experimental procedure

We carried out several experiments to investigate PMI generation in air-filled ANDi MOFs with quasi-CW pump. In particular, the experimental characterization of PMI sidebands produced with fibers A-MOF1 and A-MOF2 is described in detailed in the following. The fibers are single-mode at the wavelength range of the experiments. The chromatic dispersion of the fibers was measured experimentally using the interferometric method described in [16]. Figure 4.8 shows the chromatic dispersion as a function of wavelength for the two fibers. Simulation results are also included, relatively good agreement between theoretical calculations and experimental data was obtained. The dispersion of the two fibers shows the typical convex profile of ANDi fibers with normal dispersion for all wavelengths. The MDW values are 836 nm and 1049 nm, for A-MOF1 and A-MOF2, respectively. The experimental values of dispersion at the experimental pump wavelength i.e., 1064 nm, are summarized in Table 4.2.

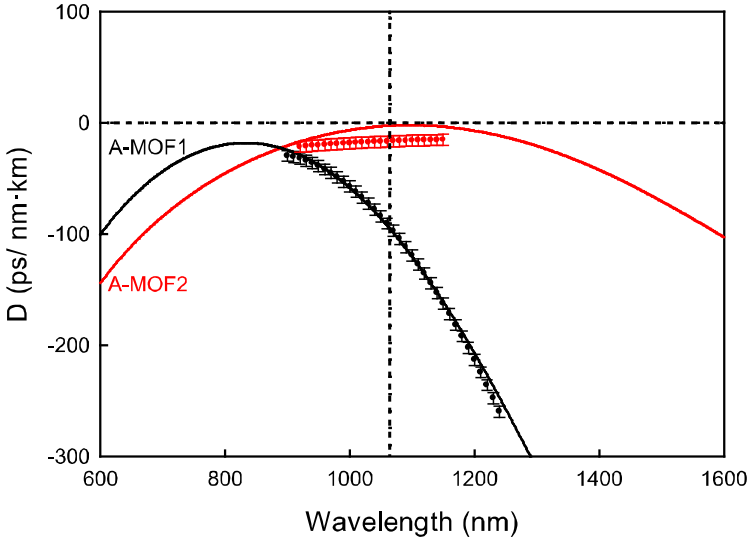

Figure 4.8. Chromatic dispersion vs. wavelength of the fibers used in the experiments. Dots are experimental measurements and solid lines are theoretical calculations.

Table 4.2. Experimental chromatic dispersion and group birefringence at 1064 nm.

Fiber	D (ps/nm km)	Δn_g (× 10^{-5})
A-MOF1	-100	1.2
A-MOF2	-21	1.1

In principle, MOFs with regular triangular lattice of identical, circular air holes are non-birefringent fibers. However, realistic fibers exhibit a small amount of residual birefringence due to imperfections in the resulting microstructure caused during the fabrication stage, and the finite number of air holes rings. The group birefringence Δn_g of both fibers was characterized using the technique described in [17]. Results are summarized in Table 4.2. In both fibers, Δn_g is in the order of 10^{-5}, which is compatible with values of unintentional birefringence in non-polarization maintaining fibers.

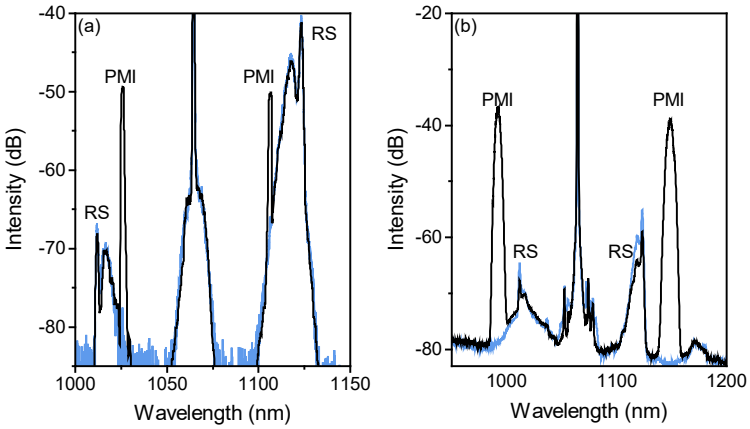

Figure 4.9. Light spectra for two orthogonal polarizations orientations of the pump: (black) pump polarization aligned to the slow axis of the fiber, and (blue) pump polarization aligned to the fiber fast axis. (a) A-MOF1, $P_0 = 3.2$ *kW* peak power. (b) A-MOF2, $P_0 = 2.5$ *kW* peak power. RS: Raman scattering.

Experiments to investigate the generation of PMI in these fibers were carried out following the experimental procedure described in Chapter 3. In this case, the fiber length used in the experiments was ~1 m. The optical spectrum exiting the fibers was analyzed for different pump powers and polarization orientations of the pump. Figure 4.9 (a) shows an example for two orthogonal orientations of the pump polarization, and identical pump power. Along with the pump laser centered at 1064 nm, one can observe several nonlinear features. For both HWP angles, Stokes and anti-Stokes Raman scattering was generated. In the case of A-MOF1, two sidebands centered at 1026 nm and 1105 nm, are shown when pump polarization was aligned with the slow axis fiber. Similarly, in fiber A-MOF2 a pair of narrow sidebands centered at 991 nm and 1148 nm was observed (see Fig. 4.9 (b)). These sidebands result from the PMI process excited by slow axis pumping. This was confirmed experimentally by studying the polarization state of the PMI sidebands. Additionally, when pump polarization was rotated by 90º so that the polarization

was aligned with the fiber fast axis, the PMI sidebands vanished and only RS sidebands and residual pump were observable.

We studied in detail the polarization of the PMI sidebands by analyzing the polarization of the light exiting the fibers by using a broadband bulk linear polarizer. We proceeded as follows: before the insertion of the polarizer, the orientation of the HWP was adjusted to launch the pump with polarization aligned to the slow axis of the fibers, therefore high amplitude PMI sidebands were generated. Then, the pump power launched into the fiber and the orientation of the HWP were kept fixed during the rest of the experiment. The polarizer was inserted at the fiber exit. The light transmitted through the polarizer was collected by a multimode fiber and recorded with an optical spectrum analyzer. Light spectra were recorded for different orientations of the polarizer axis. The transmission of the different spectral components varied with the orientation of the polarizer. Figure 4.10 shows the output spectrum from fibers A-MOF1 and A-MOF2, obtained when the polarizer was oriented so that the amplitude of the PMI bands was the maximum (black line). Starting from this orientation, rotation of the polarizer induced the reduction of the amplitude of the PMI bands and, simultaneously, the increase of the amplitude of the rest of spectral components i.e., pump and Raman sidebands. The blue line corresponds to 90° rotation of the polarizer from the initial position. For both fibers, the PMI bands were completely filtered, while the rest of spectral components, including the pump laser line and Raman bands, increased in amplitude few tens of dB. This result confirms that the polarization of the PMI bands is orthogonal to the polarization of the pump laser (and also to the Raman scattering bands since they have the same polarization as the pump), as it corresponds to the PMI process.

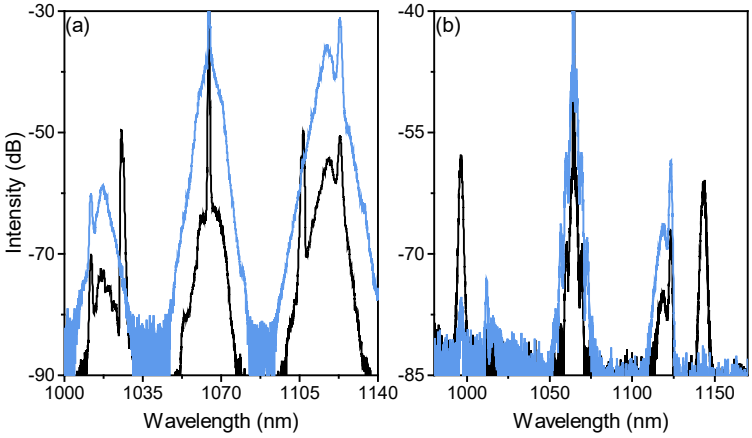

Figure 4.10. Spectra of light leaving the fibers after passing through the polarization analyzer. Two different orientations of the polarizer are shown: (black) polarizer axis adjusted to obtain the best PMI amplitude, i.e., oriented to slow-axis, and (red) polarizer axis rotated 90° with respect to the previous orientation, i.e., oriented to fast-axis. Fibers: (a) A-MOF1 and (b) A-MOF2.

We experimentally studied the spectral shift of PMI sidebands induced by pump power variations. Figure 4.11 (a) and (b) shows the spectrum around the PMI bands generated in A-MOF1, as a function of the input pump power (average values). The HWP was adjusted to optimize PMI bands. As expected, all the frequencies generated by the different nonlinear mechanisms increase in amplitude. Additionally, we can notice that, unlike Raman features, the PMI bands shift slightly. PMI bands shifts away from the pump wavelength as the pump power increases, few nanometers for the pump wavelength range of the experiments. Figure 4.11 (c) summarizes the shift of the Stokes and anti-Stokes PMI wavelengths as a function of pump power. Theoretical calculations of pump power induced wavelength shift of PMI sidebands is depicted by solid lines in Fig. 4.11 (c). The calculated spectral shift of PMI sidebands increases linearly with pump power, as it was observed in the experiments. However, small difference between theoretical calculations and experimental data is observed. The PMI bands shift with pump power as a result of

the contribution of the nonlinear term into the phase mismatch, which adds up to the frequency shift of PMI. Additionally, for large normal dispersion at the pump wavelength, being the case of the fiber A-MOF1, PMI frequency shift dependence on pump power is particularly small, what it was observed in the experiments. When increasing the delivered peak pump power up to *3.2 kW* (*42 mW*, average power) the PMI bands shifts only few nm (~9 nm). PMI was not observed in any of the two fibers for fast-axis pumping. This agrees with what it is expected since estimated values of P_{Th} are *9.4 kW* and *6.4 kW* for A-MOF1 and A-MOF2, respectively, and in our experimental arrangement the largest value of peak power that could be launched into the fiber was around 6 kW, which is below for such P_{Th} values.

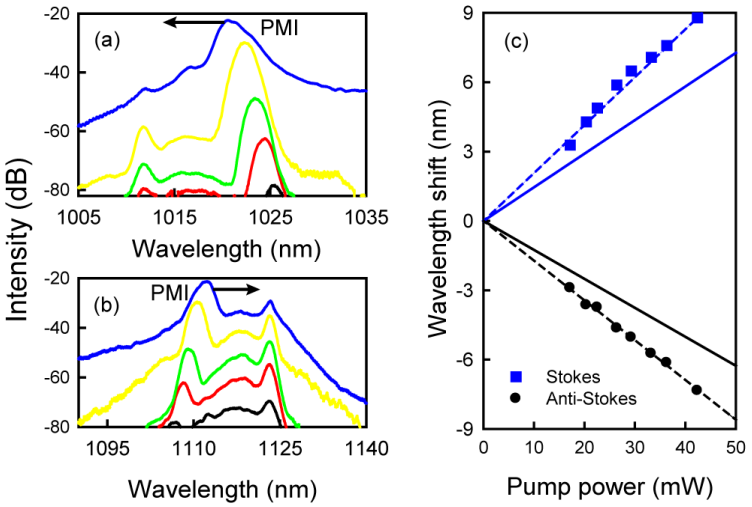

Figure 4.11. (a)-(b) Spectrum of light at the wavelength range around the PMI anti-Stokes and Stokes bands, respectively, for increasing pump power. (c) Wavelength shift as a function of average pump power. Dots are experimental data and solid lines are theoretical calculations. Dashed lines are a guide to the eye.

Figure 4.12 shows the theoretical calculations of the spectral shift between the pump wavelength and PMI wavelengths as a function of pump wavelength, for fiber

A-MOF1 and A-MOF2. Slightly different phase birefringence values were considered for the calculations of the phase-matching wavelengths. The experimental PMI Stokes and anti-Stokes wavelengths, obtained for pump wavelength of 1064 nm are also included. Best agreement between theoretical calculations and experimental data is achieved for $\Delta n = 1.8\times10^{-5}$ and $\Delta n = 4.5\times10^{-6}$, for A-MOF1 and A-MOF2, respectively. Notice that the phase birefringence values obtained from the fitting differ from the experimental values of group birefringence included in Table 4.1, since phase birefringence and group birefringence are not exactly the same parameter. The corresponding polarization beatlength calculated from the phase birefringence are 5.9 cm and 23.6 cm, for A-MOF1 and A-MOF2, respectively. Assuming a group velocity of 2.0×10^{8} m/s the pump pulse spatial width is about 14 cm, which is in the same order of magnitude of the fibers beat length.

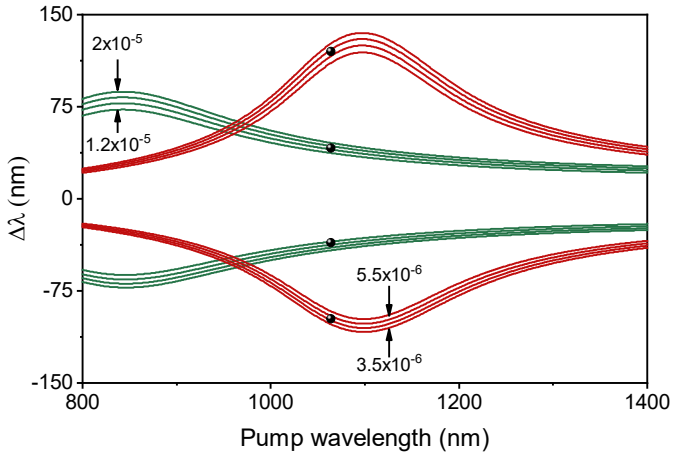

Figure 4.12. Wavelength shift of PMI Stokes and anti-Stokes bands as a function of pump wavelength, for A-MOF1 (green) and A-MOF2 (red). Solid lines are theoretical calculations, and dots are experimental data. Phase birefringence values used in theoretical calculations are indicated.

The rest of air-filled ANDi MOFs were characterized following the procedure described above. All fibers can produce PMI sidebands when pumped at 1064 nm,

as was expected according to their dispersion design. Furthermore, the PMI effect was experimentally corroborated by studying the polarization state between the polarization of PMI sidebands and the polarization of the pump. Figure 4.13 shows the resulting optical spectra from each fiber sample. Table 4.3 summarizes the spectral position (and frequency shift) of PMI bands generated in the studied fibers.

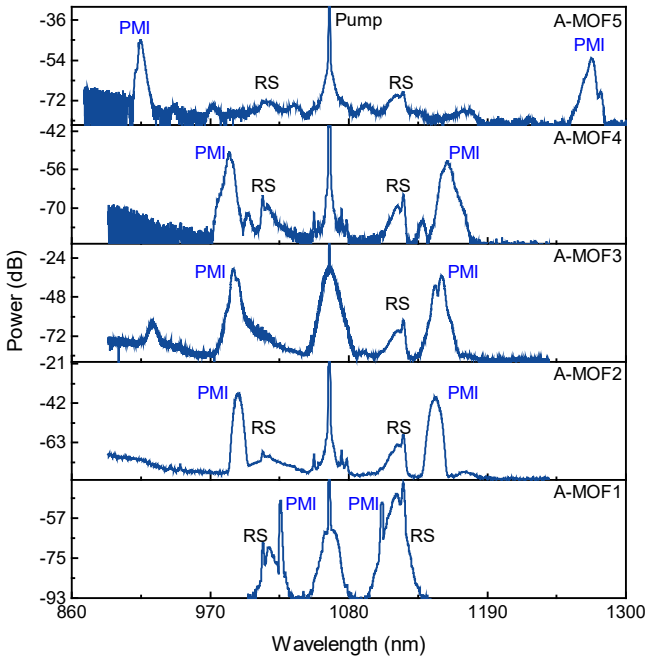

Figure 4.13. PMI spectra generated in air-filled ANDi MOFs. Raman scattering (RS).

Table 4.3. Wavelength and frequency shift of PMI bands generated in air-filled ANDi MOFs. Best fit of modal birefringence.

Fiber	Anti-Stokes (nm)	Stokes (nm)	Frequency shift (cm^{-1})	Δn
A-MOF1	1026	1105	353	1.8×10^{-5}
A-MOF2	991	1148	686	4.5×10^{-6}
A-MOF3	988	1154	727	1.72×10^{-5}
A-MOF4	985	1158	760	9.56×10^{-6}
A-MOF5	915	1273	1535	6.41×10^{-5}

The wavelengths at which the bands were generated varied accordingly with the dispersion characteristics and residual birefringence of each fiber. It can be said that the experimental results point out the effect of fiber dispersion. Large PMI frequency shift was attained when the pump wavelength was close to the MDW, and the dispersion at the pump wavelength was as small as possible (close to zero). In our experiments, the largest PMI frequency shift (1535 cm^{-1}) was attained with fiber A-MOF5 with anti-Stokes and Stokes bands centered at 915 nm and 1273 nm, respectively. When the pump wavelength is far from the MDW, so that the fiber dispersion at the pump wavelength is larger (absolute dispersion value), the frequency shift becomes smaller. As a representative example, fiber A-MOF1 generated PMI bands centered at 1026 and 1105 nm, which corresponds to a frequency shift of 353 cm^{-1}.

In general terms, experimental results can be described appropriately with theoretical calculations of PMI wavelengths, when considering the fiber properties. Figure 4.14 shows the theoretical results of PMI frequency shift as function of pump wavelength for the different fibers, along with the experimental data. Good agreement between theoretical calculations of PMI frequency shift and experimental data is achieved. Phase birefringence from Table 4.3 was considered. The comparison between the results obtained for A-MOF4 and A-MOF5 points out the contribution of phase-birefringence to the PMI frequency shift. Both fibers exhibit similar values of dispersion at the pump wavelength but phase-birefringence of A-MOF5 is larger and that leads to a larger PMI frequency shift.

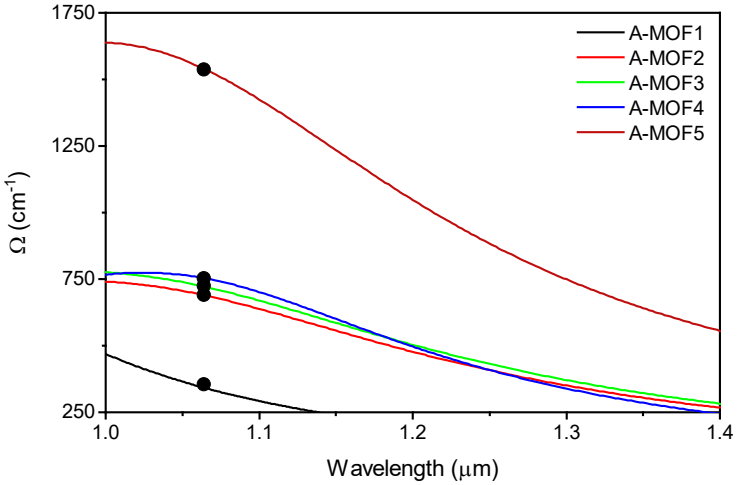

Figure 4.14. PMI frequency shift as a function of pump wavelength calculated for air-filled ANDi MOFs. P_0=*2.5 kW*. Dots are experimental data.

In the experiments, it was not observed any feature that would indicate the generation of scalar FWM/MI with the fiber under study, which is in agreement with theoretical models that predict that no phase-matching for scalar FWM/MI is accomplished in weakly-birefringent ANDi fibers. In principle, two PMI process are possible. However, fast-axis PMI presents a power threshold that was not reached according with the fibers' properties.

4.3 PMI generation in liquid-filled MOFs

In the present section we will show the generation of widely spaced PMI sidebands produced in a wide collection of liquid-filled MOFs. The contribution of chromatic dispersion and birefringence to the net linear phase mismatch of PMI is investigated in MOFs with one (or two) zero dispersion wavelengths. Suitable manufacturing parameters are given for fibers with λ_{ZDW} near 1064 nm. In particular, we report theoretical simulations and detailed experimental study of PMI effect,

investigated in a collection of EtOH-filled, and D_2O-filled MOFs with different structural parameters and chromatic dispersion properties.

4.3.1 MOFs characteristics

Fibers used in the experiments were designed and fabricated to present low dispersion at the experimental wavelength of 1064 nm in order to achieve large frequency shift of PMI sidebands. A wide collection of fibers was fabricated following the *stack-and-draw* technique, after the fibers were fabricated, they were infiltrated, either with EtOH or with D_2O through capillarity force and gas pressure. All fibers were single-mode at the experimental wavelength range. In particular, the studied fibers were fabricated with at least one ZDW near the pump wavelength. Physical and waveguiding characteristics of the fibers are described below.

(i) EtOH-filled MOFs

A collection of MOFs with the appropriate dispersion characteristics for PMI generation with the holes filled with EtOH were designed and fabricated. Figure 4.15 (b) shows their SEM images taken before EtOH infiltration. Table 4.4 gives the structural parameters of the fibers. The guiding characteristics were calculated considering the refractive index of EtOH and including its wavelength dispersion [9].

Table 4.4. Characteristics of the EtOH-filled fibers.

Fiber	Λ (μm)	d/Λ	D (ps/nm km)†	MDW (μm)	λ_{ZDW} (μm)	A_{eff} (μm²)†
E-MOF1	2.66	0.43	-34.1	1.3	-	20.1
E-MOF2	2.76	0.54	-19.1	1.32	-	12.3
E-MOF3	2.83	0.57	-16.1	1.344	-	11.6
E-MOF4	2.90	0.59	-13.7	-	1.208	11.2
E-MOF5	2.92	0.60	-13.4	-	1.2	11.2
E-MOF6	3.97	0.75	-8.4	-	1.12	13.1

†calculated at 1064 nm

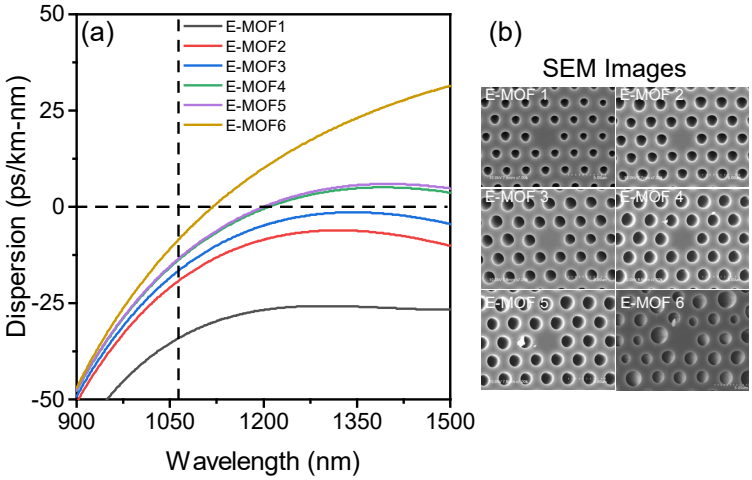

Figure 4.15. (a) Chromatic dispersion of MOFs with holes filled with EtOH. (b) SEM images of the fibers. Dashed vertical black line indicates the experimental pump wavelength.

Figure 4.15 (a) shows the dispersion profile of the six fibers investigated. All of them exhibit normal dispersion at the experimental wavelength. According with their dispersion characteristics, different types of fiber were obtained. Three fibers showed an ANDi profile (E-MOF1, E-MOF2 and E-MOF3), with different values of dispersion at the MDW and increasing values of dispersion at 1064 nm. Two fibers (E-MOF4, E-MOF5) showed a dispersion profile that shows two ZDWs, the first near to 1200 nm and second close to 1600 nm, quite far from the pump wavelength. These two fibers have very similar characteristics, although not identical. The results of both fibers have been included to show that PMI frequency shift can be very sensitive to the fiber properties. Finally, we included in this study one MOF (E-MOF6) with a dispersion profile showing just one ZDW, at $\lambda_{ZDW} = 1117\ nm$ which is in the vicinity of the pump wavelength, and a small value of normal dispersion at the pump wavelength. It is noteworthy that the chromatic dispersion of all these six fibers having air in the holes was anomalous at the pump wavelength, with the λ_{ZDW} quite below the pump wavelength.

(ii) D_2O-filled MOFs

Figure 4.16 (b) shows SEM images of the cross-section of the fibers that were selected for infiltration with D_2O. Table 4.5 gives their fibers structural parameters, as well as the chromatic dispersion and effective area at 1064 nm. The guiding properties were calculated taking into account the refractive index of D_2O and its wavelength dispersion [9]. Figure 4.16(a) shows their dispersion characteristics. All of them exhibited normal dispersion at the pump wavelength. One MOF (D-MOF1) showed an ANDi profile with the MDW at 1360 nm, and the dispersion profile of the rest of MOFs showed one ZDW at different values of wavelength, from 1092 nm to 1140 nm, and increasing dispersion values at 1064 nm, from -9.1 ps/nm km to -3.9 ps/nm km.

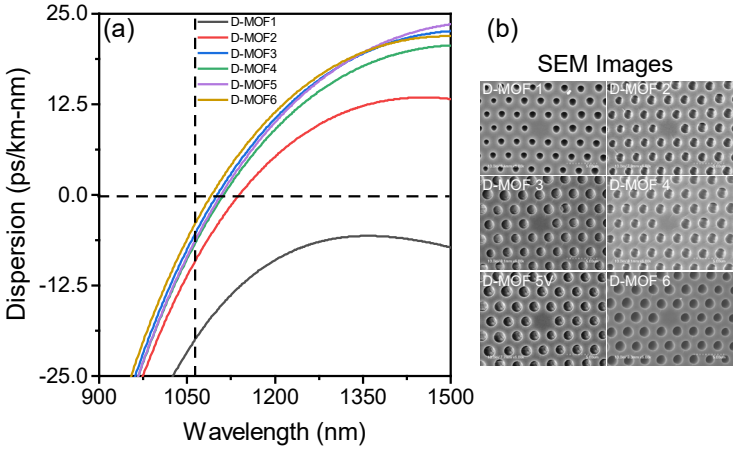

Figure 4.16. (a) Chromatic dispersion of MOFs with holes filled with D_2O. (b) SEM images of D_2O-filled MOFs cross-section. Dashed vertical black line indicates the experimental pump wavelength.

Table 4.5. Characteristics of D_2O-filled fibers.

Fiber	Λ *(μm)*	*d*/ Λ	D (ps/nm km)†	λ_{ZDW} (μm)	A_{eff} (μm²)†
D-MOF1	2.68	0.44	-19.9	-	15.0
D-MOF2	2.78	0.54	-9.1	1.14	10.9
D-MOF3	2.86	0.59	-5.3	1.102	9.9
D-MOF4	2.92	0.56	-6.6	1.112	11.2
D-MOF5	2.95	0.58	-6.2	1.107	10.8
D-MOF6	2.76	0.62	-3.9	1.091	9.0

†calculated at 1064 nm

4.3.1 Experimental characterization

The nonlinear characterization of the fibers was carried out with the experimental setup described in Chapter 3. The spectral bands produced in the fibers under study were characterized following the experimental procedure described in section 4.2. All fibers were able to produce PMI sidebands when pumped at 1064 nm, as it was expected according to their dispersion design. Figure 4.17 shows the resulting optical spectra from each fiber sample. Fiber sections of length of ~1m were used in the experiments. Notice that high orders of PMI were generated in some fibers. Table 4.6 summarizes the spectral position (and frequency shift) of first-order PMI bands generated in the fibers.

In the case of liquid-filled MOFs with ANDi profile, similar results were obtained to those reported in section 4.1. In particular, when the pump wavelength was far from the MDW, so that the fiber dispersion at the pump wavelength is larger (absolute dispersion value), the frequency shift becomes smaller. As a representative example, fiber D-MOF1 generated PMI bands centered at 1031 and 1100 nm, which corresponds to a frequency shift of 303 cm^{-1}, which was the smallest obtained in the experiments.

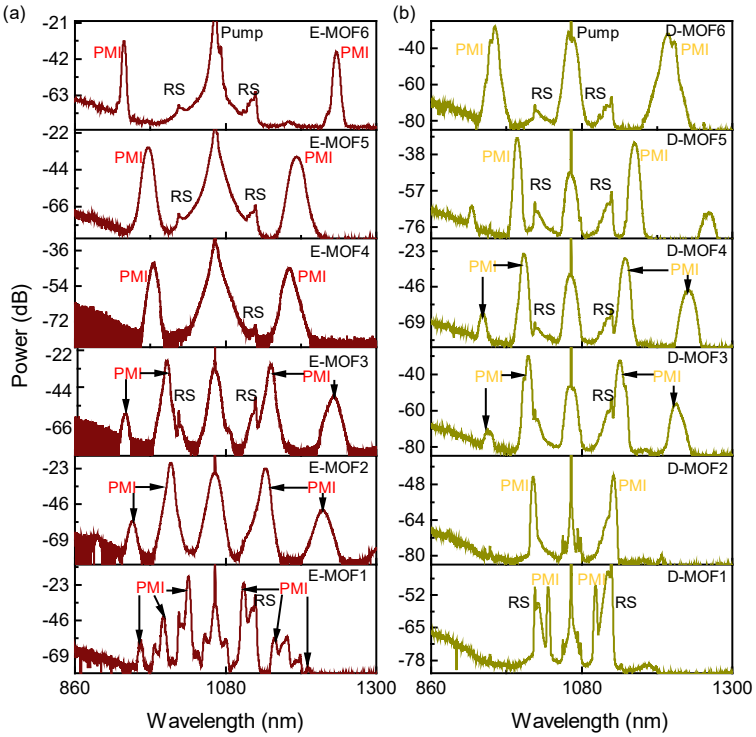

Figure 4.17. PMI spectra generated in (a) EtOH-filled MOFs and (b) D_2O-filled MOFs.

The frequency shift of PMI generated in fibers with conventional dispersion profiles can also be very large when the pump wavelength is close to a ZDW and, therefore, the dispersion is low. From our experiments, we can investigate the generation of PMI in fibers with one ZDW with different chromatic dispersion at the pump wavelength. For example, the results obtained from the sequence of fibers E-MOF4, E-MOF5 and E-MOF6, with dispersion values increasing from -13.7 ps/(nm-km) to -8.4 ps/(nm-km), show PMI frequency shift clearly increases as the dispersion value increases, from 874 cm^{-1} in the case of E-MOF4 to 1343 cm^{-1} for E-MOF6.

Table 4.6. Wavelength and frequency shift of PMI bands generated in EtOH- and D_2O-filled MOFs. Modal birefringence.

Filling substance	Fiber	Anti-Stokes (nm)	Stokes (nm)	Frequency shift (cm^{-1})	Δn
EtOH	E-MOF1	1025.4	1106	352.3	6.28×10^{-6}
	E-MOF2	1000	1138.2	608.3	1.03×10^{-5}
	E-MOF3	993.7	1146.6	672.7	1.05×10^{-5}
	E-MOF4	974.1	1173.7	874	1.60×10^{-5}
	E-MOF5	965.2	1185.8	961	1.80×10^{-5}
	E-MOF6	931.7	1242	1342.7	2.24×10^{-5}
D_2O	D-MOF1	1031	1100	303.3	1.55×10^{-6}
	D-MOF2	1009.2	1126.7	518.7	1.91×10^{-6}
	D-MOF3	1002	1136	591.3	7.0×10^{-7}
	D-MOF4	995	1144	652.7	3.40×10^{-6}
	D-MOF5	985.6	1157.8	757	3.79×10^{-6}
	D-MOF6	952.8	1206.1	1103	5.21×10^{-6}

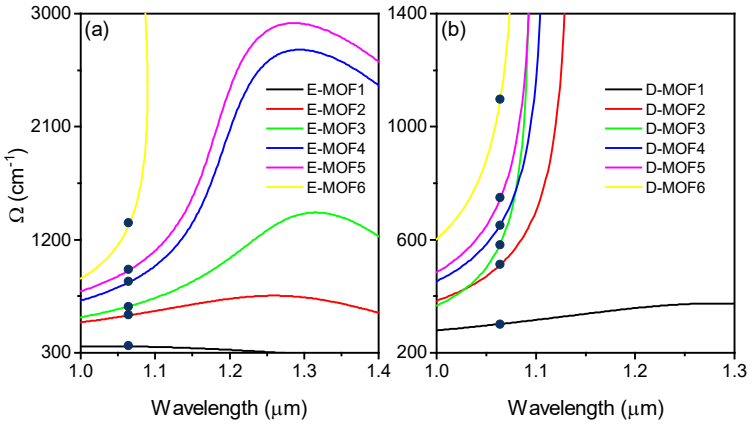

Figure 4.18. PMI frequency shift as function of pump wavelength calculated for (a) EtOH-filled MOFs and (b) D_2O-filled MOFs. Dots are experimental data. $P_0 = 3$ *kW* for both, EtOH-filled MOFs and D_2O-filled MOFs.

The wavelengths at which the bands were generated varied accordingly with the dispersion characteristics and residual birefringence of each fiber. Fiber

birefringence values stated in Table 4.6 were obtained from fitting the theoretical calculations of frequency shift to the experimental results. The resulting values of birefringence range from 10^{-5} to 10^{-7}, which are compatible with residual phase birefringence values in solid core MOFs. Figure 4.18 shows the theoretical results of PMI frequency shift as function of pump wavelength for the different fibers, along with the experimental data.

Again, we can notice that, in some fibers with similar values of dispersion, PMI produces bands with quite different frequency shifts. For example, the frequency shift in ANDi fibers A-MOF1 (see Table 4.3) and D-MOF1 is 686 cm^{-1} and 303 cm^{-1}, respectively. Similarly, it happens for some fibers filled with D_2O. Residual phase birefringence is at the origin of this apparent discrepancy. As stated before, phase birefringence plays a major role in the phase matching condition of PMI effect and adds positively to the frequency shift. The larger the birefringence, the more it contributes to the frequency shift.

Regarding the bandwidth of the PMI sidebands, we observed that fibers with large normal dispersion can produce PMI sidebands with spectral bandwidths narrower than fibers with low normal dispersion. For instance, anti-Stokes bands generated in D-MOF1 and D-MOF6 exhibits a bandwidth of 2.8 nm and 9.7 nm, respectively. Bandwidth was measured at full-width at half maximum (FWHM) and same pump power. It is known that, higher slopes of the linear mismatch term (dispersion contribution) induced spectral broadening of PMI/FWM sidebands, especially for low dispersion at the pump wavelength (near to the ZDW), being the case of fiber D-MOF6. The contrary occurs in fibers with large normal dispersion, which is the case of the studied D_2O-filled ANDi fiber. We investigated this effect theoretically. We calculated the gain spectrum of PMI for both fibers. We have followed the approach for PMI gain described in [18], where PMI gain was derived as a function of the net-phase mismatch equation. This approximation takes into

account higher order dispersion terms, which is required to model accurately ANDi fibers. In comparison, the gain expression derived in Chapter 2 (Eq. 2.81) only considered β_2, therefore, such expression loses accuracy when it is applied to fibers with small β_2 or complex dispersion profiles. Figure 4.19 shows the calculated gain spectrum of anti-Stokes sidebands generated in fibers D-MOF1 and D-MOF6. It can be observed that the gain bandwidth for both fibers is in reasonably good agreement with the experimental values. For gain calculations we considered the experimental pump wavelength and pump power (2.8 kW).

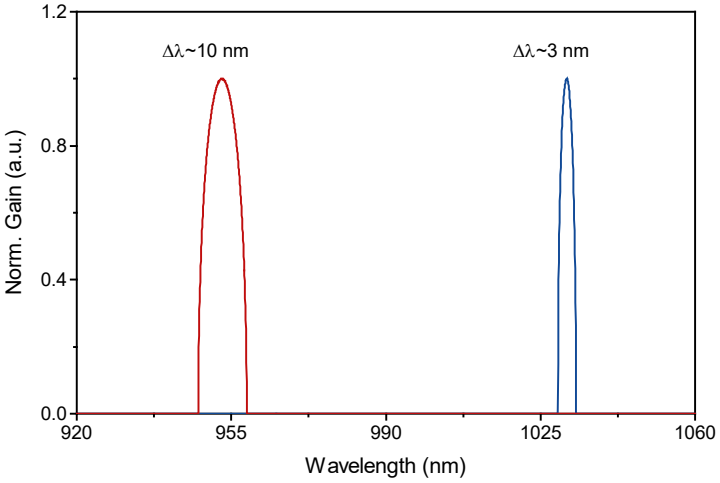

Figure 4.19. Normalized gain spectrum of anti-Stokes sidebands for fibers: D-MOF1 (blue line) and D-MOF6 (red line).

In general, the spectral bandwidth of PMI sidebands is determined by fiber birefringence and dispersion. However, in the case of fibers D-MOF1 and D-MOF6 the phase birefringence values are in the same order of magnitude, and therefore, the difference in gain bandwidth is mainly attributed to the different dispersion.

As mentioned before, in fibers with one ZDW, the PMI effect exhibits a cut-off wavelength, often close to the λ_{ZDW} so that PMI can no longer occur for pump wavelengths above it. Large frequency shifts can be attained by pumping near the

wavelength at which the cut-off takes place, as it happens for fibers E-MOF6 and D-MOF6. Operating near the PMI cut-off might have also some drawbacks: the large frequency shift slope is likely to cause the generation of broader bands than expected in realistic fibers due to the lack of perfect fiber uniformity along the fiber.

In the case of fibers with two relatively close ZDWs and ANDi MOFs, both showing convex dispersion profile, the largest frequency shift is attained when the pump wavelength is close to the MDW. Phase matching can occur regardless of the pump wavelength in the first type, even under anomalous dispersion pumping. However, it is important to remark that additional four-wave mixing processes, in particular, scalar FWM and modulation instability, can happen in fibers with dispersion profiles showing one or two ZDWs, while they are forbidden in ANDi fibers.

In summary, we have reported a detailed study regarding PMI generation in a wide collection of fibers. Air-filled, EtOH-filled and D_2O-filled fibers featuring different chromatic dispersion characteristics have been investigated using long pump pulses at 1064 nm. It has been shown that PMI frequency shift can be very large in ANDi fibers with low dispersion values when they are pumped close to the MDW. Large frequency shift is also observed in MOFs with dispersion profiles with one ZDW (or two ZDW) that were pumped near the ZDW.

References

1. S. Wabnitz, "Modulational polarization instability of light in a nonlinear birefringent dispersive medium," Phys. Rev. A **38**, 2018–2021 (1988).

2. G. Millot, E. Seve, S. Wabnitz, and M. Haelterman, "Observation of induced modulational polarization instabilities and pulse-train generation in the normal-dispersion regime of a birefringent optical fiber," J. Opt. Soc. Am. B **15**, 1266 (1998).

3. G. P. Agrawal, *Nonlinear Fiber Optics* (Elsevier Inc., 2019).

4. P. Kockaert, M. Haelterman, S. Pitois, and G. Millot, "Isotropic polarization modulational instability and domain walls in spun fibers," Appl. Phys. Lett. **75**, 2873–2875 (1999).

5. M. Xie, Y. Seok Lee, R. Tannous, G.-L. Long, and T. Jennewein, "Roles of fiber birefringence and Raman scattering in the spontaneous four-wave mixing process through birefringent fibers," Opt. Express **29**, 31348 (2021).

6. L. Velázquez-Ibarra, A. Díez, E. Silvestre, and M. V. Andrés, "Wideband tuning of four-wave mixing in solid-core liquid-filled photonic crystal fibers," Opt. Lett. **41**, 2600 (2016).

7. J. R. Ott, M. Heuck, C. Agger, P. D. Rasmussen, and O. Bang, "Label-free and selective nonlinear fiber-optical biosensing," Opt. Express **16**, 20834 (2008).

8. M. H. Frosz, A. Stefani, and O. Bang, "Highly sensitive and simple method for refractive index sensing of liquids in microstructured optical fibers using four-wave mixing," Opt. Express **19**, 10471 (2011).

9. S. Kedenburg, M. Vieweg, T. Gissibl, and H. Giessen, "Linear refractive index and absorption measurements of nonlinear optical liquids in the visible and near-infrared spectral region," Opt. Mater. Express **2**, 1588 (2012).

10. A. M. Heidt, A. Hartung, G. W. Bosman, P. Krok, E. G. Rohwer, H. Schwoerer, H. Bartelt, J. Herrmann, U. Griebner, N. Zhavoronkov, A. Husakou, D. Nickel, J. C. Knight, W. J. Wadsworth, P. S. J Russell, and G. Korn, "Supercontinuum generation in photonic crystal fiber," Rev. Mod. Phys **78**, 1135–1184 (2010).

11. A. M. Heidt, "Pulse preserving flat-top supercontinuum generation in all-normal dispersion photonic crystal fibers," J. Opt. Soc. Am. B **27**, 550 (2010).

12. L. E. Hooper, P. J. Mosley, A. C. Muir, W. J. Wadsworth, and J. C. Knight, "Coherent supercontinuum generation in photonic crystal fiber with all-normal group velocity dispersion," Opt. Express **19**, 4902–4907 (2011).

13. I. A. Sukhoivanov, S. O. Iakushev, O. V. Shulika, E. Silvestre, and M. V. Andrés, "Design of All-Normal Dispersion Microstructured Optical Fiber on Silica Platform for Generation of Pulse-Preserving Supercontinuum under Excitation at 1550 nm," J. Light. Technol. **35**, 3772–3779 (2017).

14. I. B. Gonzalo, R. D. Engelsholm, M. P. Sørensen, and O. Bang, "Polarization noise places severe constraints on coherence of all-normal dispersion femtosecond supercontinuum

generation," Sci. Rep. **8**, (2018).

15. A. M. Heidt, J. S. Feehan, J. H. V. Price, and T. Feurer, "Limits of coherent supercontinuum generation in normal dispersion fibers," JOSA B, Vol. 34, Issue 4, pp. 764-775 **34**, 764–775 (2017).

16. P. Hlubina, M. Szpulak, D. Ciprian, T. Martynkien, and W. Urbanczyk, "Measurement of the group dispersion of the fundamental mode of holey fiber by white-light spectral interferometry," Opt. Express **15**, 11073 (2007).

17. R. B. (Richard B. . Dyott, *Elliptical Fiber Waveguides* (Artech House, 1995).

18. R. J. Kruhlak, G. K. Wong, J. S. Chen, S. G. Murdoch, R. Leonhardt, J. D. Harvey, N. Y. Joly, and J. C. Knight, "Polarization modulation instability in photonic crystal fibers," Opt. Lett. **31**, 1379 (2006).

Chapter 5
Tuning of PMI sidebands

In many applications based on FWM, the ability to tune the wavelength of generated light is a prime requirement. In the last years, different strategies have been followed to tune the bands produced by scalar FWM, for instance, by tuning the pump laser wavelength [1]. In this chapter, we will describe effective tuning techniques that allow to control the frequency shift of the PMI sidebands over a wide spectral range in standard optical fibers and MOFs. The tuning techniques presented in this chapter are based on the control of fiber parameters through physical factors such as temperature or mechanical stress. These external factors are related to linear variations of phase birefringence induced by the elasto-optic effect, and to simultaneous variations of the fiber dispersion and birefringence induced by the thermo-optic effect. In addition, we experimentally demonstrate that thermal control of fiber parameters can lead to large frequency tuning range of high amplitude PMI bands for adequate dispersion values.

5.1 PMI wavelength control through the elasto-optic effect

5.1.1 Theoretical description

Elasto-optic effect (EOE) is a well-studied effect in optical fibers, this effect describes the changes in the optical properties of a material when it is subjected to

mechanical stress. In the most common applications with dielectric materials, EOE is used to described the relative variation of the refractive index of a material under deformations. Refractive index perturbation can be derived through variations of material impermeability (δb) induced by strain (S). A tensor formalism is required to describe the impermeability perturbation. Owing to the tensor symmetry of impermeability and strain [2], EOE can be described as below,

$$b_i(S) = b_i^0 + \delta b_i(S) = b_i^0 + \sum_j^6 p_{ij} S_i \qquad (5.1)$$

where bi *(i, j=1, 2, … 6)* are the elements of the impermeability tensor, b_i^0 is the impermeability tensor of the unperturbed material (which is related to the inverse of dielectric permittivity). The impermeability tensor perturbation induced by strain is a function of the strain-optic tensor p_{ij}. For an isotropic material, p_{ij} can be written as follows [3],

$$p_{ij} = \begin{pmatrix} p_{11} & p_{12} & p_{12} & & & & \\ p_{12} & p_{11} & p_{12} & & & & \\ p_{12} & p_{12} & p_{11} & & & & \\ & & & p_{44} & & & \\ & & & & p_{44} & & \\ & & & & & p_{44} & \end{pmatrix} \qquad (5.2)$$

The elements not stated in Eq. 5.2 are zero. For fused silica, strain-optic coefficients values are $p_{11} = 0.121$, $p_{12} = 0.270$ and $p_{44}=1/2(p_{11} + p_{12})$ [4]. In order to derive the permeability variation, the strain tensor must be expressed according with the form of the mechanical deformation. In different experiments of this work, the spectral position of PMI sidebands was actively controlled trough variations of phase birefringence induced by (1) fiber bending or (2) by strain applied to coiled fibers. In the following sections, derivation of phase birefringence induced by those two particular perturbations is addressed.

(i) Linear birefringence induced by fiber bending

In single-mode fibers, weak or residual birefringence can arise from two possible factors, first, from deviation of core geometry produced during fiber fabrication; and second, from mechanical stress through EOE. The last includes bending-induced birefringence. In [5], the authors pointed out that bending-induced birefringence is essentially a second-order stress effect. It results of lateral compressive stress that arises from bent fiber under large deformations (i.e., large bending radii). Figure 5.1 shows a schematic of stress induced by fiber bending. In the transversal plane (x, y) the stress σ_z exerts a tensile stress in outer layers from $x > 0$ and σ_z exerts a compression of inner layers from $x < 0$. Therefore, outer layers exert a stress $-\sigma_x$ in radial direction to the inner layers. In the core region, the stress $-\sigma_x$ is different from zero, actually it is maximum, consequently linear birefringence is produced.

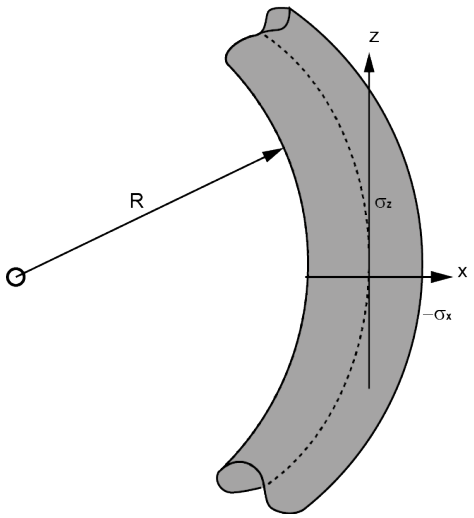

Figure 5.1. Geometry of a bent fiber.

For these calculations, the optical fiber was considered to be made of an elastically homogeneous and isotropic material. Thus, stress tensor can be easily transformed to strain through Hooke's law, and considering the stress subjected to the condition $r/R << 1$ [4], where r is the fiber radius and R is the bending radius of curvature. The stress σ_i can be written as below,

$$\sigma_1 = \left(\frac{1}{R}\right)^2 \frac{E}{2}\left(x^2 - r^2\right), \quad \sigma_2 = 0, \quad \sigma_3 = \frac{E}{R}x \tag{5.3}$$

where E is the Young's modulus. It results that only $\sigma_1(x)$ is the responsible for linear birefringence induced by bending in single mode fibers. Once the stress components are determined, phase birefringence can be derive considering the difference of the propagation constant of the fundamental mode, $HE_{11,}$ between both polarizations, $\Delta\beta = \beta_x - \beta_y \approx k_0\,(\delta n_x - \delta n_y)$, with k_0 the wavenumber in vacuum and δn_i the variation of the refractive index along the i-axis in the core region due to the bending effect. The lateral stress σ_1 is maximum at the core region, δn_i can be evaluated through EOE by $\delta n_i = (n^3/2) \cdot \sum p_{ij} S_i$ and considering the transformation $S_1 = (\sigma_1 - v(\sigma_2 + \sigma_3)) \cdot 1/E$ and $S_2 = (\sigma_2 - v(\sigma_1 + \sigma_3)) \cdot 1/E$, where v is Poisson's ratio. Birefringence can be expressed as,

$$\Delta\beta = -\frac{1}{4} k_0 n^3 \left(p_{11} - p_{12}\right)(1+v)\left(\frac{r}{R}\right)^2 \tag{5.4}$$

The expression in Eq. 5.4 together with the approach reported [6] were used to estimate the phase-birefringence contribution produced by fiber bending used in the experiments. The expression for bending-induced birefringence reported in [6] follows the theoretical procedure detailed here. In their approach, the phase-birefringence expression includes the dependence on normalized frequency (V) in order to consider the guiding properties of the bent fiber.

(ii) Birefringence induced by tensioned – coiled fibers

It is known that by symmetry, birefringence in an optical fiber is unsensitive to deformations in axial direction when fiber is submitted to a purely axial strain S_z. On the other hand, high birefringence can be induced to optical fibers by simply coiling the fiber with axial tension on a cylinder, as it was demonstrated in [7]. In their work, it was reported that small beat lengths (up to 2 cm) can be achieved in ordinary fibers with circular core by coiling and tensioning the fibers around a cylinder with small radius.

In order to estimate the birefringence induced in a tension-coiled fiber, we follow the theoretical procedure described in [7]. The transverse stress related to a tension-coiled fiber can be approximated to that in a freely bent slab guide with a circumscribed fiber with a thin core region, the slab width is *2r* that is equal to the fiber diameter, as shown in Fig. 5.2.

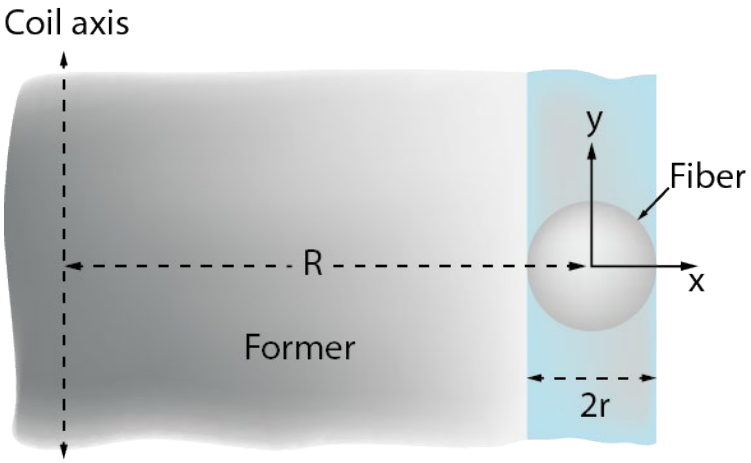

Figure 5.2. Geometry of a tension-coiled fiber.

The transversal stress (σ_x, σ_y) on the slab axis causes the variation of fiber refractive index. Therefore, birefringence can be derived considering the change in

the refractive index due the elasto-optic effect. Following the procedure described in bending-induced birefringence and considering $r/R << 1$ and an isotropic and elastically homogeneous medium, birefringence induced by transversal stress can be written as,

$$\Delta\beta = -\frac{1}{2E} k_0 n^3 \left(p_{11} - p_{12}\right)\left(\sigma_x - \sigma_y\right) \qquad (5.5)$$

To calculate the stress difference in Eq. 5.5, we recall the average longitudinal stress σ_z, when the slab/fiber is coiled in the circular holder. It results in a first order strain $E \cdot S_z = \sigma_z + (E/R) \cdot x$, that induces equal contractions in the transversal plane of the slab/fiber, therefore, the components of strain tensor are linearly related as $S_x = S_y = -v \cdot S_z$. Nevertheless, it turns out that birefringence is independent of the first-order transversal strain, since its influence cancels in Eq. 5.5. The latter indicates that birefringence in a tensioned-coiled slab/fiber is mainly affected by second-order elastic effects (which is similar to bending-induce birefringence) produced by longitudinal stretching. In [7], the second-order stress difference $\sigma_x^{(2)} - \sigma_y^{(2)}$ is estimate to be $(3 \cdot v - 2) \cdot (1 - v)^{-1} \cdot (r/R) \cdot E \cdot S_z$. Therefore, birefringence in a tensioned-coiled fiber is derived as,

$$\Delta\beta = \frac{k_0 n^3}{2}\left(p_{11} - p_{12}\right)\frac{(1+v)(2-3v)}{(1-v)}\left(\frac{r}{R} \cdot S_z\right) \qquad (5.6)$$

From Eq. 5.6, it can be seen that, birefringence in a tension-coiled fiber is closely related to the birefringence induced when a fiber is bent freely (i.e., without axial tension). However, when a fiber is subjected simultaneously to bending and tension, a second-order mixing of the first-order bending and tensile stress effects occurs, producing a second-order birefringence that is proportional to the product of $1/R$ and S_z. Therefore, if either curvature or axial strain vanishes, birefringence in tensioned-coiled fiber also vanishes.

5.1.2 Experimental characterization

As indicated in Chapter 2, frequency tuning of PMI sidebands can be achieved by controlling the parameters of an optical fiber, essentially chromatic dispersion and/or fiber phase-birefringence. In this section, spectral tuning of PMI sidebands is demonstrated by properly controlling the phase birefringence of an optical fiber. Mechanical deformations of a fiber, such as pure fiber bending or stretching and bending, were employed to induce birefringence variations in the optical fiber.

(i) PMI frequency shift induced by fiber bending.

These experiments were carried out with single-mode step-index fibers, in particular we used the fiber SM980 from Fibercore Ltd. The fiber parameters provided by the manufacturer are included in table 5.1. This fiber was chosen because it features very low bend losses. In addition, it exhibits normal dispersion at the experimental wavelength, therefore, the generation of PMI can be produced in such fibers.

Table 5.1. Fiber parameters and cylinder diameters and curvature.

Fiber SM980		Curvatures		
		Cylinder	Diameter (cm)	1/R (m^{-1})
Diameter (μm)	125.4	C_1	6.5	30.8
Core radius (μm)	2.2	C_2	4	50.0
N.A.	0.17	C_3	3	66.7
Cut-off wavelength (nm)	970	C_4	1	200
α(@980 nm) (dB/km)	1.5	C_5	0.7	285.7

Fiber sections with a length of 1.5 m were coiled into five cylinders of different diameter (see Table 5.1). We kept the polymer coating of the fiber and no tension was applied to the fibers during the coiling stage in order produce birefringence induced by pure bending. Experiments of PMI generation of each coiled-fibers were

carried out following the experimental arrangement described in chapter 3. Measurements of optical spectra were performed with a fixed pump power level (1.07 kW peak power) in order to avoid PMI spectral shift contributions produced by pump power fluctuations. The pump polarization orientation was adjusted to excite the slow-axis eigenmode. PMI was observed from the fibers that were coiled on the cylinders. In contrast, PMI generation was not observed when the experiment was performed with sections of loose fibers (uncoiled), as it is depicted in Fig. 5.3. The latter can be due to the low residual birefringence of that fiber, in conjunction with the large chromatic dispersion at the pump wavelength. Under such conditions, PMI is generated with detuning frequency close to zero and PMI bands can be easily overlapped by other nonlinear effects such as self-phase modulation.

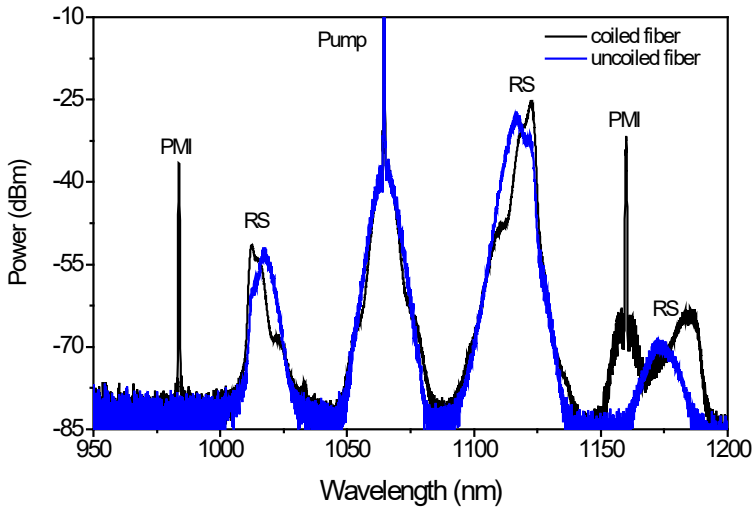

Figure 5.3. Output spectra for a coiled-fiber on C5 (black trace) and uncoiled fiber (blue trace). PMI sidebands centered at 983 nm (anti-Stokes) and 1160 nm (Stokes). RS: Raman scattering.

Experimental results of PMI spectral evolution against birefringence induced by fiber bending is depicted in Fig. 5.4(a). It can be observed that PMI spectral shift increases as the curvature *(1/R)* increases. Within the range of curvature of the

experiment, from 31 m^{-1} to 286 m^{-1}, PMI frequency shift varies linearly with *(1/R)*. PMI anti-Stokes sideband shifts from 1052 nm to 983 nm, while the Stokes band shifts from 1077 nm to 1160 nm. In addition, it can be observed the PMI gain bandwidth decreases with increasing *(1/R)*, in particular, the bandwidth of PMI bands (measured at -3 dB from the maximum amplitude) produced with $(1/R) = 31$ m^{-1} was 1.4 nm and the bandwidth produced with $(1/R) = 286$ mm^{-1} is 0.4 nm.

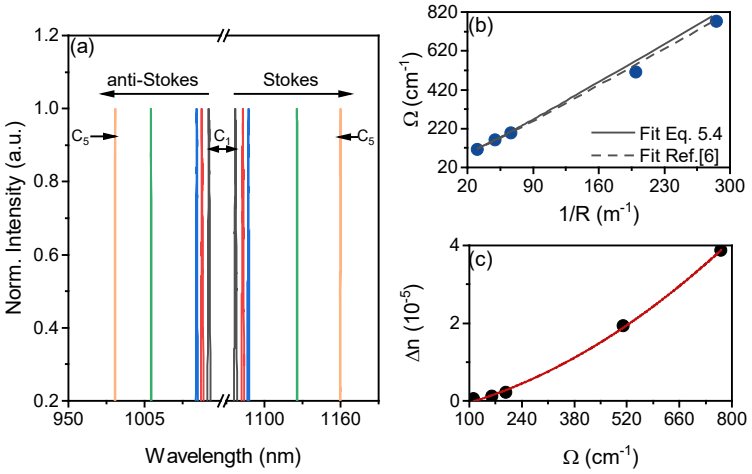

Figure 5.4. (a) PMI bands normalized in amplitude for different curvatures (values stated in table 5.1). (b) PMI frequency shift as function of 1/R. Dots are experimental data, and lines are calculations using birefringence values of bent fibers obtained using Eq. 5.4 (dashed line) and from [6] (solid line). (c) Phase-birefringence as a function of PMI frequency shift.

We performed numerical calculations of the frequency shift of PMI in fibers subjected to bending. PMI frequency shift in bent fibers can be calculated by taking into account the birefringence induced by bending (for example, using Eq.5.4) and setting the birefringence into the PMI phase-matching condition. The propagating factor of the fundamental mode of the step-index fiber required to evaluate the phase-matching condition was calculated by solving the Maxwell's equations with

the corresponding boundary conditions [8]. Figure 5.4(b) shows the comparison between experimental data and PMI frequency shift calculations when fibers are subjected to different curvatures. Good agreement between calculations and experimental results is obtained.

The results shown in Fig. 5.4 demonstrate that fiber birefringence can be estimated by means of PMI frequency shift measurement. The fiber employed in the experiments exhibit a high normal dispersion value at the pump wavelength $D = -36.8\ ps/km{\cdot}nm$. According with theory, when PMI is generated in fibers with high normal dispersion values, phase-birefringence is the main contribution to the frequency shift of PMI, in comparison, the contributions of chromatic dispersion and pump power affects the PMI frequency shift in a minor way. Figure 5.4(c) shows the phase-birefringence as a function of the PMI frequency shift. Equation 5.4 has been used to estimate the phase-birefringence from the bending radius. The quadratic trend was expected, since the PMI frequency shift is linearly dependent on r/R and the dependence of Δn on r/R is quadratic. The experimental values were fitted to a second order polynomial, $\Delta n = a{\cdot}\ \Omega^2 + b{\cdot}\Omega + c$. Fitting parameters are provided in table 5.2.

Table 5.2. Fitting parameters for birefringence vs. PMI frequency shift

a (cm^2)	*b* (*cm*)	*c*	*Correlation Coef.* (r^2)
4.39799×10^{-11}	2.02176×10^{-8}	-2.94066×10^{-6}	0.998

(ii) PMI frequency shift in tensioned-coiled fibers

The frequency shift between PMI sidebands and the pump light was investigated in a tensioned-coiled fiber. The birefringence induced in a tensioned-coiled fiber was varied by applying different amounts of tension to the fiber coil, and the response of PMI bands was investigated.

Experiments were carried out with the single-mode step-index fiber SM980 described in the previous section. Fibers sections of length 1.3 m were coiled onto two semi-cylinders with a radius of 8.6 mm. The coating polymer was kept for the experiments and no tension was applied to the fiber during the coiling stage. One semi-cylinder was attached to a linear translation stage driven by a micrometer. The remaining semi-cylinder was fixed to the optical table, as shown in Fig.5.5.

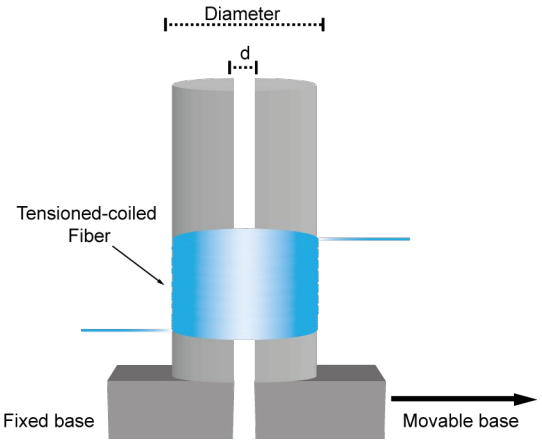

Figure 5.5. Schematic of the fiber tensioned and coiled on two half cylinders, axial tension applied through a movable base.

Strain is applied to the fiber by means of the translation stage by displacing the half-cylinder. The distance d (see Fig. 5.5) is proportional to the relative elongation of the fiber considering the condition of $d<<r_0$ (i.e., maintaining the shape of a cylinder), being r_o the radius of the cylinder when both bases are face-to-face (at $d=0$). By considering $R_c = r_o + d/2$ as the radius of coiled-fiber for each position of the translation stage, then the axial strain can be derived considering the effective fiber coiling length $L_{eff} = 2 \cdot m \cdot \pi \cdot r_0$, where m is the number of turns of the fiber coil. Hence, the axial strain can be written as,

$$S_z = \frac{\Delta L}{L_{eff}} = \frac{d}{2r_0} \qquad (5.7)$$

Spectral characterization of tuning of PMI sidebands was carried out. Pump power of 1.2 kW was injected into the fiber and kept fixed during the experiments. The polarization of the pump was adjusted to match the slow-axis of the coiled fiber. Measurements of the PMI bands were recorded as a function of the distance *d*.

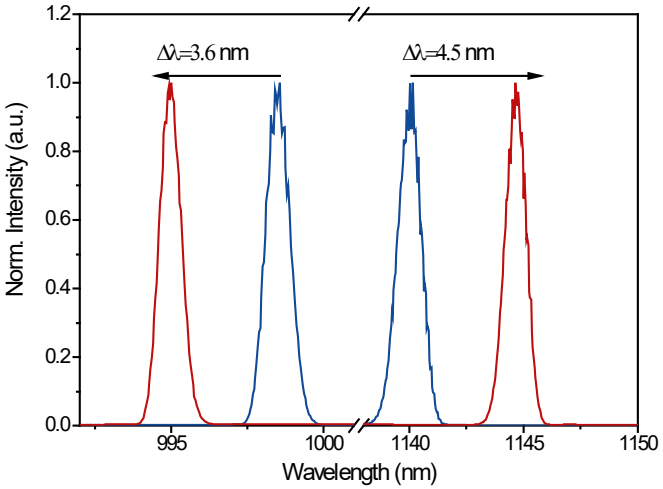

Figure 5.6. Light spectrum at the coiled fiber output for: (blue) non-tensioned fiber, and (red) axially strained fiber at 0.34 %.

With $d = 0$, i.e. without axial tension, PMI was generated by pure bending effect. The spectral position of PMI bands was measured at 998 nm (anti-Stokes) and 1140 nm (Stokes) when fiber is free of tension. The estimated phase-birefringence induced by bending curvature was 2.6×10^{-5}. Figure 5.6 shows the PMI bands when axial strain of 0.0034 was applied to the fiber. The PMI frequency shift increases, then, the anti-Stokes band shift toward shorter wavelengths while Stokes band shift toward longer wavelength.

We measured in detail the optical response of PMI sidebands was as a function of strain. Optical spectra were recorded with a distance step $d = 5$ μm. Figure 5.7

shows the tuning range of PMI sidebands as a function of axial strain. A tuning frequency range from 621 cm^{-1} to 726 cm^{-1} is achieved. By translating the half-cylinder to the initial position in which no axial strain is applied to the fiber, PMI sidebands shifts again to the spectral position induced by pure bending. The latter demonstrated that the tuning technique developed in this work is reproducible.

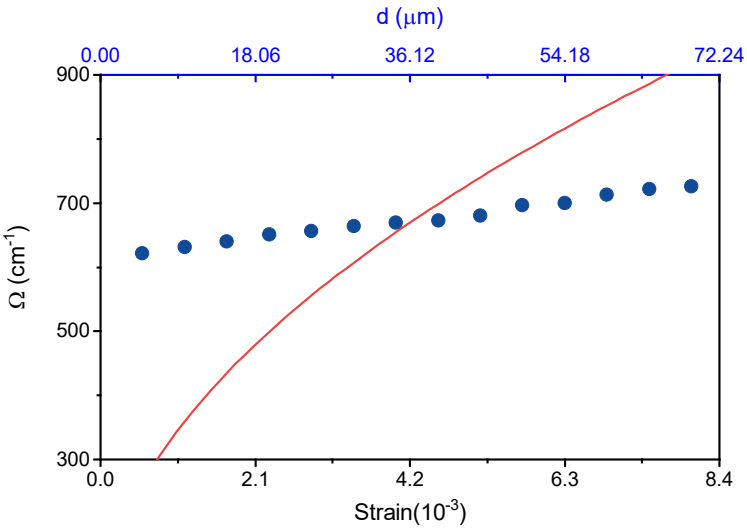

Figure 5.7. PMI frequency shift as a function of axial strain, dots are experimental data and solid line calculations.

PMI frequency shift can be calculated theoretically by setting the birefringence from Eq. 5.6 into the PMI phase-matching equation. Numerical results are included in Fig. 5.7. Theoretical calculations of PMI frequency shift show large discrepancy with the measured values of frequency shift, and predict a much larger sensitivity than observed experimentally. The main source of error is attributed to the determination of the birefringence induced by tensioned-coiled fiber. Equation 5.6 was derived for coiled-fibers with no polymer coating. Therefore, in our experiments the elastic contribution of the polymer coating of the coiled fiber was not considered for the calculation of the induced birefringence. In such way, the elasticity of the

coating polymer severely damps the effective axial strain induced by the translation base. This issue has also been reported in birefringence modulators based on fibers coils strained by cylindrical piezoelectric actuators [9]. In our experiments, we kept the fiber coating to dampen the internal lateral tension intrinsically induced by the small curvature of the cylindric mold in which the fiber is wound, since such internal lateral tension is large enough to cause cracks or break the fiber.

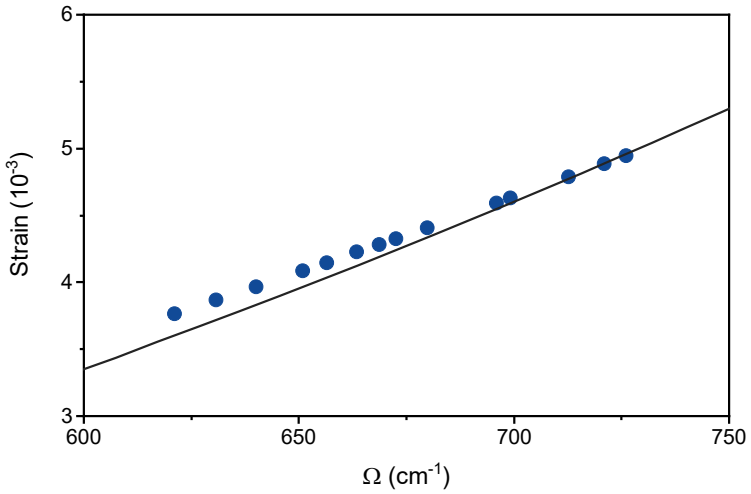

Figure 5.8. Axial strain as a function of PMI frequency shift. Dots are experimental data and solid line calculations.

The true experimental strain applied to the silica fiber can be estimated as follows. In the previous section, we established the relationship between PMI frequency shift and fiber birefringence by fitting the experimental values of phase birefringence as a function of PMI frequency shift values. By considering that the PMI frequency shift becomes more sensitive to the variations of phase birefringence under the condition of large normal dispersion at the pump wavelength, the effective axial strain applied to the tension-coiled fiber can be evaluated. For this purpose, we consider the birefringence fitting of Table 2 along with Eq. 5.6 to determine the experimental values of the axial strain.

The effective strain applied to the fiber obtained after this correction vary from $(3.8\pm0.1)\times10^{-3}$ to $(5.0\pm0.2)\times10^{-3}$. Results are shown in Fig. 5.8 (b). The contribution of birefringence induced by pure fiber bending on the cylindric mold (when no axial strain is applied) is neglected in axial strain calculations. Reasonably good agreement is obtained between the measured frequency shift and theoretical calculations when corrected axial stress values are considered.

The frequency tuning range of PMI sidebands achieved in our experiments range from 621 cm^{-1} to 726 cm^{-1} in a strain span ranging from 3.8×10^{-3} to 5.0×10^{-3}. In [10], a similar technique was used to control the PMI sidebands, in it the tuning range of PMI from 116 cm^{-1} to 233 cm^{-1} was attained, which is similar to the tuning range shown here. Nevertheless, the relationship between axial strain and PMI frequency was not mentioned in the experiments.

The comparison between the frequency tuning range of PMI sidebands achieved in the present work and those reported in the literature based on fiber birefringence variations are shown in Table 5.3. The PMI sideband tuning ranges achieved in the present work are similar to those previously reported in the literature.

Table 5.3. Comparison of tuning range of PMI sidebands-by achieved by different.

Present work			**Literature**		
Tuning method	Frequency shift (cm^{-1})		Tuning method	Frequency shift (cm^{-1})	
	from	to		from	to
Fiber bending	111	779	Fiber bending [11]	320	1057
			Fiber bending [12]	~	333
Tensioned-coiled fiber	621	726	Tensioned-coiled fiber [10]	117	233

5.2 PMI wavelength control through thermo-optic effect

In the present section we report the wideband tuning of high amplitude spectral bands generated through PMI in MOFs through the thermo-optic effect. As it has been explored with theoretical calculations in Chapter 2 and experimentally demonstrated in Chapter 4 and in section 5.1 of this chapter, PMI phase-matching condition is sensitive to variations of guiding parameters of the fiber, as dispersion and birefringence, and also on pump power.

In principle, the guiding properties of solid-core MOFs with air-holes are quite insensitive to changes of temperature [13, 14]. One of the reasons is that MOFs are made of a single material and thermo-optic coefficient of silica is very low. In order to enhance the temperature sensitivity of MOFs, we proposed the use of MOFs infiltrated with liquids. The large thermo-optic coefficient (TOC) of the mentioned filling liquids, allows producing significant changes of the fiber properties by moderate changes of the fiber temperature. In particular, a change of fiber temperature produces changes in both, chromatic dispersion and birefringence, leading to strong tunability of PMI in this hybrid fibers. Recently, the tuning of sidebands produced by scalar FWM was demonstrated in liquid-filled MOFs [15, 16]. Tuning of the FWM sidebands was achieved by controlling the chromatic dispersion of a hybrid MOF by taking advantage of the large TOC of the infiltrating liquids. In this sense, we followed the technique described in [15] to tune the sidebands produced by PMI over a wide wavelength range through thermal heating.

5.2.1 Simultaneous variations of dispersion and birefringence induced by thermal heating

Is well known that PMI wavelengths presents strong dependence for slight variations of fiber chromatic dispersion and fiber birefringence, when pumping near

to ZDW [17]. In this section, we demonstrate experimentally broadband tuning of widely spaced PMI bands generated by pumping in normal dispersion near the ZDW, by simultaneous variation of fiber dispersion and birefringence. Experiments were carried out with ethanol-filled and heavy-water-filled MOFs. Such liquids were selected due to its large TOC, low absorption at the experimental wavelength and adequate refractive index (lower than fused silica).

The fibers used in the experiments were designed and fabricated to produce widely space PMI bands when the microstructure was infiltrated with the corresponding liquid, and pumped at 1064 nm wavelength. Ethanol and heavy water exhibit a negative TOC; thus, the refractive index of such liquids will decrease with increasing temperature. Then, a change of temperature modifies the refractive index of the liquid, which leads to modifications of the properties of the microstructure that surrounds the fiber core. As a result, the guiding properties of the fiber are sensitive to temperature variations, in particular, chromatic dispersion and birefringence can be modified through changes of temperature.

Table 5.4. Structural parameters for ethanol-filled fibers and heavy-water-filled fibers.

Fiber	Liquid	Λ (μm)	d/Λ
E-MOF	Ethanol	3.97	0.75
HW-MOF	Heavy-water	2.8	0.62

Figure 5.9 shows the dispersion properties at room temperature (21 °C) of two MOFs used in the experiments, whose structural parameters are included in table 5.4. Calculations were performed both, with holes empty and filled with ethanol/heavy-water. Theoretical modeling of the MOFs was performed by considering the real spatial refractive-index distribution obtained from scanning electron microscope images of the fibers' cross-sections. Propagating constant of the fundamental mode, phase-birefringence and effective area were calculated. The

wavelength dispersion of refractive indices of silica, ethanol and heavy-water [18] were considered in the simulations. An effective area of 13.2 μm² and 10 μm² was calculated at room temperature for fibers E-MOFs and HW-MOF, respectively. Fibers exhibit a small residual phase birefringence due to slight imperfections of the fiber microstructure of $\Delta n=2.0\cdot10^{-5}$ and $\Delta n=5.6\cdot10^{-6}$ for the E-MOF and HW-MOF, respectively. For E-MOF fiber, the ZDW shifts from 1023 nm to 1119 nm after ethanol infiltration, and the chromatic dispersion at 1064 nm switches from anomalous to normal. Similar behavior occurs for HW-MOF fiber, the ZDW shifts from 963 nm to 1091 nm after heavy-water infiltration.

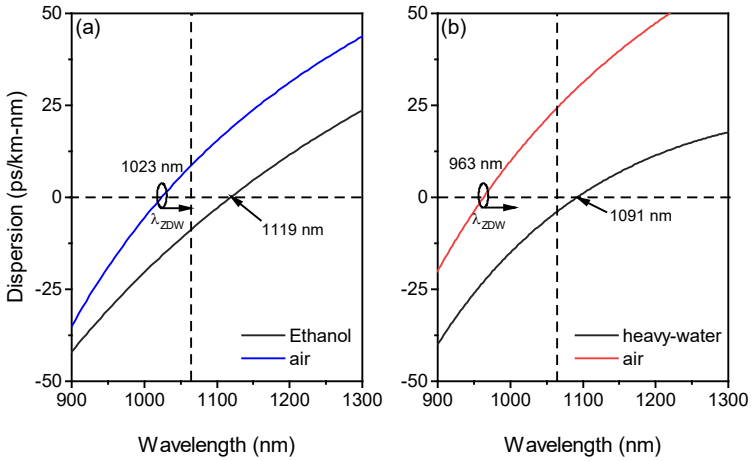

Figure 5.9. Chromatic dispersion as a function of wavelength for: (a) E-MOF before (blue line) and after (black line) ethanol infiltration, and (b) HW-MOF before (red line) and after (black line) heavy-water infiltration. Vertical dashed line indicates pump wavelength at 1064 nm.

First, we investigated theoretically the dependence of the fiber guiding properties on temperature. Figure 5.10 shows the calculations of guiding properties as a function of temperature, of the two MOFs. The thermo-optic coefficient of ethanol and heavy-water used in the calculations were $-3.99\times10^{-4}°C^{-1}$ [19] and -

$6.6 \cdot 10^{-5}$ °C^{-1} [20], respectively. The thermo-optic properties of silica (TOC value $8.6 \cdot 10^{-6}$ C^{-1} [21]) were also taken into consideration, although its contribution to the chromatic dispersion and birefringence of the fibers for the experimental range of temperatures was very small and it could have been neglected (an increment of temperature ΔT=80°C causes a change of $\Delta D \sim 10^{-4}$ and $\Delta n \sim 10^{-7}$). For both type of fibers, the ZDW shifts towards shorter wavelengths when increasing the temperature, as shown in Figs. 5.10 (a)-(d). Consequently, the chromatic dispersion at 1064 nm increases (see Figs. 5.10 (b)-(e)). The phase birefringence increases with increasing the fiber temperatures as a result of the increment of the refractive index contrast between the silica and the microstructured region of the fiber (see Figs. 5.10 (c)-(f)). Notice that ethanol TOC ($\sim 10^{-4}$) is one order of magnitude larger than heavy-water's TOC ($\sim 10^{-5}$), nevertheless, guiding properties of the filled-fibers varies with temperature in the same order magnitude.

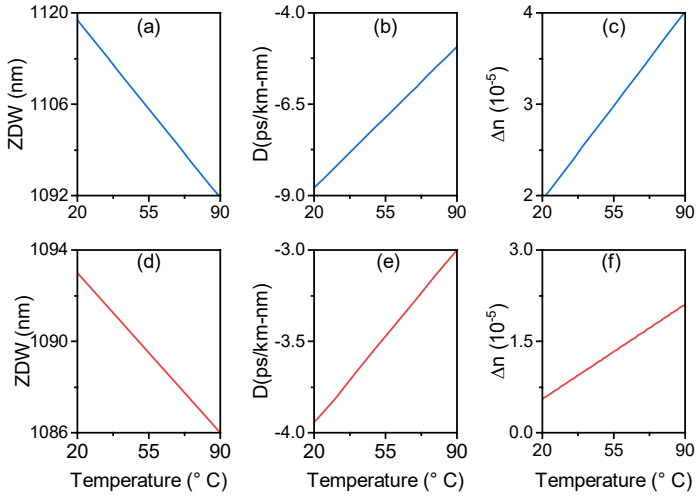

Figure 5.10. Guiding properties of (blue) E-MOF and (red) HW-MOF as a function of temperature. (a, d) ZDW, (b, e) chromatic dispersion and (c, f) phase-birefringence at 1064 nm.

When E-MOF and HW-MOFs fibers are empty (air holes), no PMI can be generated at a pump wavelength of 1064 nm. Instead scalar MI can be generated due to anomalous dispersion at the pump wavelength. When the fiber holes are filled with the liquids, the pump wavelength is in the vicinity of the ZDW for both fibers. This can lead to the generation of widely-spaced PMI bands by exciting the fibers at the experimental wavelength. We theoretically studied the dependence of PMI wavelengths on temperature changes for E-MOF and HW-fibers. Figure 5.11 shows theoretical calculations of PMI wavelengths for the investigated fibers as a function of pump wavelength, for different temperatures. Phase birefringence changes, as well as, dispersion changes induced by temperature variation are included in the calculations of PMI wavelengths.

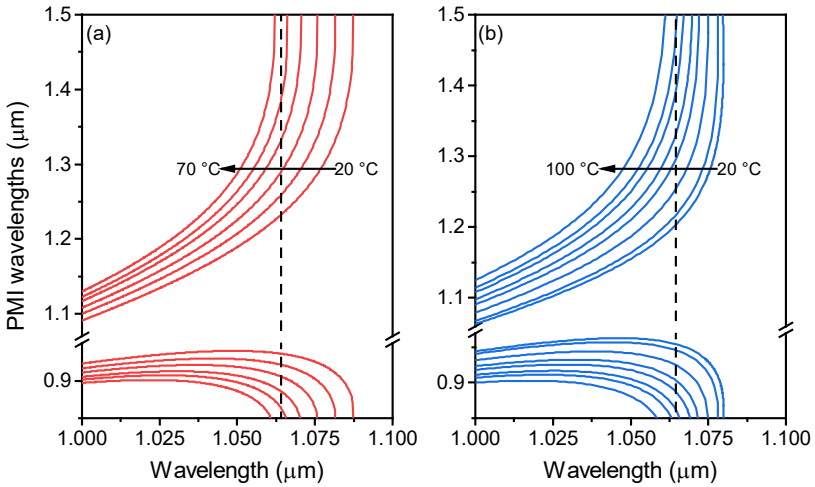

Figure 5.11. Calculations of PMI parametric wavelengths as a function of pump wavelength, for different temperatures: (a) E-MOF and (b) HW-MOF. Temperature step between consecutive curves is 10 °C. Vertical dashed line indicates the experimental pump wavelength. $P_0=1$ kW.

As the temperature increases, the PMI wavelengths shift away from the pump wavelength indicating that PMI frequency shift increases with temperature. Due to

the curve bending, there is a threshold temperature above which no solutions are found for a given pump wavelength. For the particular case of the fibers investigated and a pump wavelength of 1064 nm, threshold is reached at temperatures of 65 °C and 95 °C for fiber E-MOF and HW-MOF, respectively.

5.2.2. Experimental characterization

PMI generation and characterization as a function of temperature for fibers infiltrated with ethanol and heavy-water was performed. Fiber sections with length of 1 m were infiltrated with ethanol or heavy-water by capillary force and air pressure, as described in Chapter 3. Then, to avoid liquid evaporation, the fibers were fusion spliced to a single-mode fiber section at one end, and to a multimode fiber section at the remaining end. The single-mode fiber acts as power injection fiber and multi-mode fiber acts as power collection fiber. Injection fiber was shortened to few cm to avoid undesirable nonlinear effects produced in such fiber. The temperature of the infiltrated MOFs was varied by immersing them into a temperature-controlled thermal bath with a temperature accuracy of ± 1°C.

Figure 5.12 shows the light spectra from two investigated fibers, an ethanol-filled fiber and a heavy-water-filled, recorded at room temperature (21 ºC) with the pump polarization matching the slow axis of the fibers. The structural parameters of these two fibers are the same as fibers E-MOF and HW-MOF, and are given in table 5.4. In both fibers, PMI bands are widely-spaced and they exhibit high amplitude. In the case of the E-MOF, the PMI bands are centered at 937 nm (anti-Stokes) and 1231 nm (Stokes), with an amplitude of 63 dB measured with respect to the OSA background noise. A peak gain of $g_{peak}=17.2\ m^{-1}$ was theoretically estimated (as described in Chapter 4) for this particular fiber. In the case of the HW-MOF, PMI bands are centered at 954 nm (anti-Stokes) and 1200 nm (Stokes), with an amplitude of 48 dB and a peak gain of $g_{peak}=10.7\ m^{-1}$ was theoretically estimated.

In Fig. 5.12, some other spectral components can be observed that correspond to Raman scattering (RS) that it is also generated. Notice that, in addition to the Raman-scattered photons generated from the 1064 nm pump, we can observe Raman bands produced by the PMI bands themselves; this indicates that the intensity of the PMI bands is remarkably high. To give some physical insights about the power carried by the PMI bands observed in our experiments, we calculated the Raman power threshold (P_{Th}) for each fiber following the Raman theory described in [22]. Assuming optimum transmission conditions (loses-free fiber $\alpha \approx 0$), the effective area of the mode at the PMI wavelengths and considering a Raman gain coefficient of silica $g_R = 10^{-13}\ m \cdot W^{-1}$, the power threshold can be calculated. The resulting Raman power threshold are $P_{Th} \sim 1.6\ kW$ and $P_{Th} \sim 0.9\ kW$ for fibers E-MOF and HW-MOF respectively. This implies that the real power of PMI bands is even higher since fiber losses were not considered in the calculations.

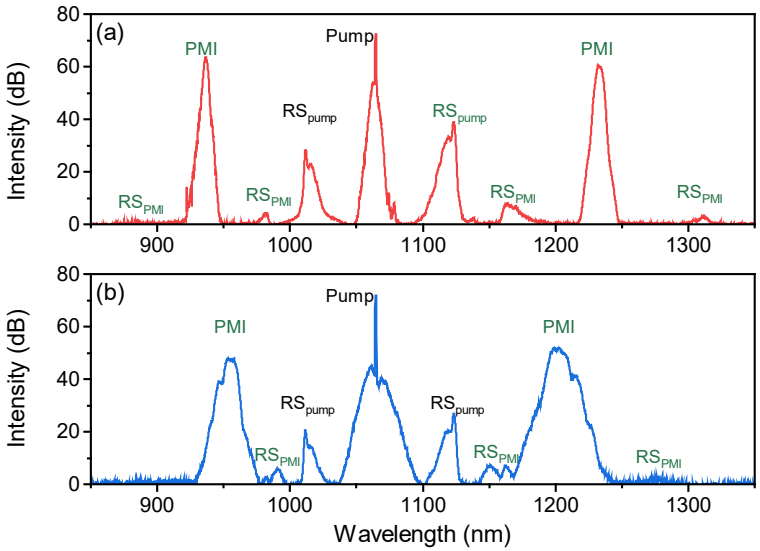

Figure 5.12. Output light spectrum of (a) ethanol-filled MOF (P_0=4.5 kW) and (b) heavy-water-filled MOF (P_0=2.13 kW). RS_{pump} and RS_{PMI} correspond to Raman scattering generated by the 1064 nm laser pump and by the PMI bands, respectively.

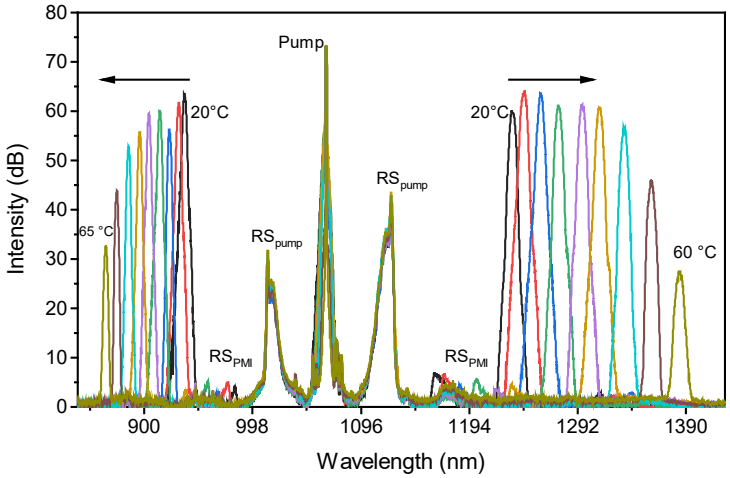

Figure 5.13. Output light spectra of the ethanol-filled MOF for different temperatures, from 21°C to 65 °C in temperature steps of 5 °C. Pump peak power: 5.4 kW.

The optical spectrum at the output light of the fibers was recorded as a function of temperature, with a temperature step of 5 °C. During the experiments, the pump power was kept fixed to avoid the wavelength shift produced by pump power fluctuations. In particular, the pump power launched into the fibers was 5.4 kW (peak power) for the ethanol-filled fiber and 2.2 kW for the heavy-water-filled fiber. Figure 5.13 shows the evolution of the optical spectrum when increasing the temperature of the ethanol-filled fiber in a temperature range from 20 ºC to 65 ºC. Notice that the spectral bands due to the Raman scattered photons from the 1064 nm pump do not change substantially with temperature. As the temperature increases, the anti-Stokes PMI band shifts towards shorter wavelengths, from 937 nm to 863 nm, and the PMI Stokes band shifts towards longer wavelengths, from 1231 nm to 1387 nm. Such tuning range corresponds to a variation of frequency shift between the pump and the PMI sidebands from 1274 cm^{-1} to 2189 cm^{-1}. The amplitude of the PMI bands tends to decrease for higher temperatures values. PMI was not observed experimentally for temperatures above 65 °C, as it was predicted by the theoretical modeling (see Fig. 5.11 (a)).

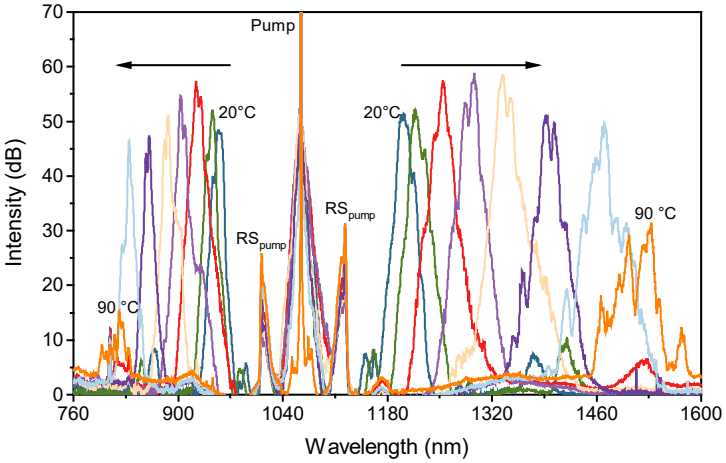

Figure 5.14. Output light spectra of the HW-MOF for different temperatures, from 20°C to 90 °C in temperature steps of 10 °C. P_0 = *2.2 kW*.

The results obtained with the heavy-water-filled fiber are shown in Fig. 5.14. For this fiber, a larger tuning range of PMI sidebands was achieved. The anti-stokes band shift to shorter wavelengths from 954 nm to 821 nm, and the stokes band shifts to longer wavelengths from 1200 nm to 1533 nm, as shown in fig.5.14 (b). Such tuning range corresponds to a variation of the frequency shift between pump and a PMI sideband from 1084 cm^{-1} to 2786 cm^{-1}. PMI was not observed experimentally for temperatures above 95 °C, in accordance with the theoretical modeling.

Comparison of experimental PMI wavelengths with theoretical calculations is shown in Fig. 5.15, for both fibers. Good agreement was obtained when the temperature dependence of both, birefringence and chromatic dispersion was considered. The calculation taking only into account the effect of chromatic dispersion is included in Fig. 5.15 (dashed lines). The disagreement with the experimental results is quite large even for small variations of phase birefringence (see Fig. 5.15 (b)), which highlights the relevance of phase birefringence in PMI process when the pumping wavelength is near to the ZDW. The latter is also shown

by the results reported in this section, in which the tuning range of PMI sidebands produced in heavy water-filled MOFs (ZDW=1091 nm) is almost twice the tuning range achieved with ethanol-filled MOFs (ZDW=1119 nm), despite the fact that TOC of ethanol is several times larger than TOC of heavy water.

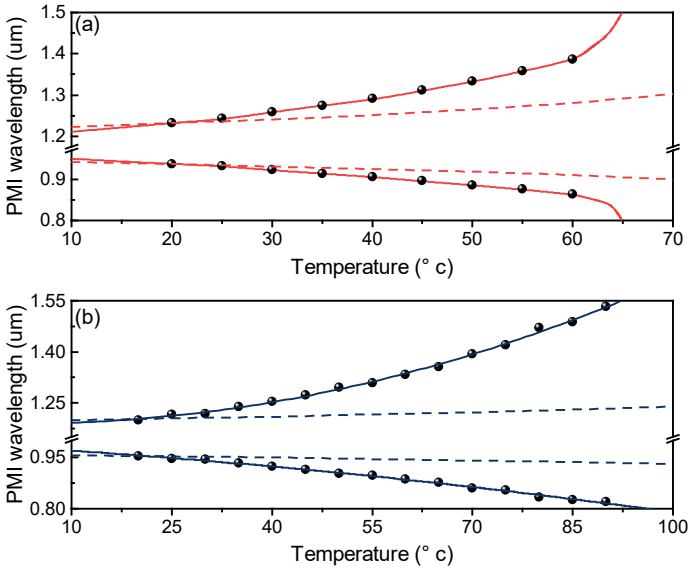

Figure 5.15. PMI wavelengths as a function of temperature for (a) ethanol-filled MOF and (b) heavy-water-filled MOF. Dots are experimental data, and lines are theoretical calculations. Dashed lines show calculations in which the temperature dependence of phase birefringence is neglected.

To our knowledge, the frequency tuning range of PMI sidebands attained in the experiments with heavy-water-filled MOFs is the largest reported for optical fibers at a fixed pump wavelength. It is true that the frequency tuning range of PMI reported in [17], is slightly larger than mentioned above, nevertheless in their experiments, a tunable laser wavelength for pumping together with PMI assisted by seeded light source was required to obtain measurable PMI sidebands, while in our case, high-amplitude PMI sidebands were produced simply by pumping such fibers with fixed wavelength pump laser with no requirement of seed signal source.

References

1. M. Baumgartl, M. Chemnitz, C. Jauregui, T. Meyer, B. Dietzek, J. Popp, J. Limpert, and A. Tünnermann, "Fiber optical parametric frequency conversion: Alignment and maintenance free all-fiber laser concept for CARS microscopy," CLEO Sci. Innov. CLEO_SI 2012 **20**, 4484–4493 (2012).

2. J. F. Nye and P. P. L. J. F. Nye, *Physical Properties of Crystals: Their Representation by Tensors and Matrices*, Oxford Science Publications (Clarendon Press, 1985).

3. M. H. Sadd, "Elasticity: Theory, Applications, and Numerics," Elast. Theory, Appl. Numer. (2009).

4. D. R. Lide, *CRC Handbook of Chemistry and Physics*, 84 edition (CRC Press, 2003).

5. R. Ulrich, S. C. Rashleigh, and W. Eickhoff, "Bending-induced birefringence in single-mode fibers," **5**, 273–275 (1980).

6. J. I. Sakai and T. Kimura, "Birefringence and Polarization Characteristics of Single-Mode Optical Fibers under Elastic Deformations," IEEE J. Quantum Electron. **17**, 1041–1051 (1981).

7. S. C. Rashleigh and R. Ulrich, "High birefringence in tension-coiled single-mode fibers," Opt. Lett. **5**, 354 (1980).

8. K. Okamoto, *Fundamentals of Optical Waveguides* (Elsevier Inc., 2006).

9. A. R. Boyain, A. Diez, J. L. Cruz, L. Martínez-León, and M. V. Andrés, "Low-frequency and high-frequency all-fiber modulators based on birefringence modulation," Appl. Opt. Vol. 38, Issue 30, pp. 6278-6283 **38**, 6278–6283 (1999).

10. S. G. Murdoch, R. Leonhardt, and J. D. Harvey, "Tuneable THz beat frequency generation in optical fibers," Opt. Commun. **130**, 25–28 (1996).

11. N. Shibata, M. Ohashi, K. Kitayama, and S. Seikai, "Evaluation of bending-induced birefringence based on stimulated four-photon mixing," Opt. Lett. **10**, 154 (1985).

12. S. G. Murdoch, R. Leonhardt, and J. D. Harvey, "Polarization modulation instability in weakly birefringent fibers," Opt. Lett. **20**, 866 (1995).

13. A. Ortigosa-Blanch, A. Díez, M. Delgado-Pinar, J. L. Cruz, and M. V. Andrés,

"Temperature independence of birefringence and group velocity dispersion in photonic crystal fibres," Electron. Lett. **40**, 1327–1329 (2004).

14. A. Kudlinski, R. Habert, M. Droques, G. Beck, L. Bigot, and A. Mussot, "Temperature dependence of the zero dispersion wavelength in a photonic crystal fiber," IEEE Photonics Technol. Lett. **24**, 431–433 (2012).

15. L. Velázquez-Ibarra, A. Díez, E. Silvestre, and M. V. Andrés, "Wideband tuning of four-wave mixing in solid-core liquid-filled photonic crystal fibers," Opt. Lett. **41**, 2600 (2016).

16. L. Velazquez-Ibarra, A. Diez, E. Silvestre, and M. V. Andres, "Tunable Four-Wave Mixing Light Source Based on Photonic Crystal Fibers with Variable Chromatic Dispersion," J. Light. Technol. **37**, 5722–5726 (2019).

17. R. J. Kruhlak, G. K. Wong, J. S. Chen, S. G. Murdoch, R. Leonhardt, J. D. Harvey, N. Y. Joly, and J. C. Knight, "Polarization modulation instability in photonic crystal fibers," Opt. Lett. **31**, 1379 (2006).

18. S. Kedenburg, M. Vieweg, T. Gissibl, and H. Giessen, "Linear refractive index and absorption measurements of nonlinear optical liquids in the visible and near-infrared spectral region," Opt. Mater. Express **2**, 1588 (2012).

19. R. C. Kamikawachi, I. Abe, A. S. Paterno, H. J. Kalinowski, M. Muller, J. L. Pinto, and J. L. Fabris, "Determination of thermo-optic coefficient in liquids with fiber Bragg grating refractometer," Opt. Commun. **281**, 621–625 (2008).

20. O. G. Peterson, "5. Dye lasers," Methods Exp. Phys. **15**, 251–359 (1979).

21. D. B. Leviton and B. J. Frey, "Temperature-dependent absolute refractive index measurements of synthetic fused silica," Optomech. Technol. Astron. **6273**, 62732K (2008).

22. G. P. Agrawal, *Nonlinear Fiber Optics* (Elsevier Inc., 2019)

Chapter 6

Simultaneous generation of FWM and PMI

In the present chapter we will describe the simultaneous generation of PMI and FWM in MOFs. Simultaneous generation of scalar FWM and PMI in low birefringence fibers can occur under a wide range of conditions. Scalar FWM generation requires the pump wavelength to be close to the ZDW, with fiber dispersion being normal at that wavelength. When these conditions are met, by controlling the polarization of the pump beam, it is possible to generate the two non-linear effects simultaneously. Under these conditions, the scalar FWM produces spectral bands of light separated from the pump. However, for the PMI effect to produce bands sufficiently far apart from the pump such that practical applications can be derived from the PMI effect, the fiber dispersion conditions that must be met are tighter. In addition, constrains are also imposed on phase birefringence. Therefore, fine control of the fiber guiding properties is required.

In chapter 2, we have studied FWM and PMI in low-birefringence fibers. It has been shown that when pumping near the ZDW [1–3], chromatic dispersion contribution mainly determines the phase-matching condition of scalar FWM [4]. On the other hand, the phase-matching condition of PMI depend mainly on both, birefringence and chromatic dispersion. Fig. 6.1 shows the numerical calculation of phase-matching wavelengths of vector FWM in two MOFs with d_1 = 1.14 μm (fiber

1) and d_2 = 1.6 μm (fiber 2) both with d/Λ = 0.38. Figure 6.1(a) gives the chromatic dispersion of the fibers, and Fig. 6.1(b) and includes phase-matching solutions for scalar FWM and PMI solutions for slow-axis pump. Two values of fiber birefringence have been considered. It is shown that PMI and FWM processes can occur simultaneously for a wide range of pump wavelengths in the normal dispersion regime, with pumping wavelengths shorter than cutoff wavelength of PMI.

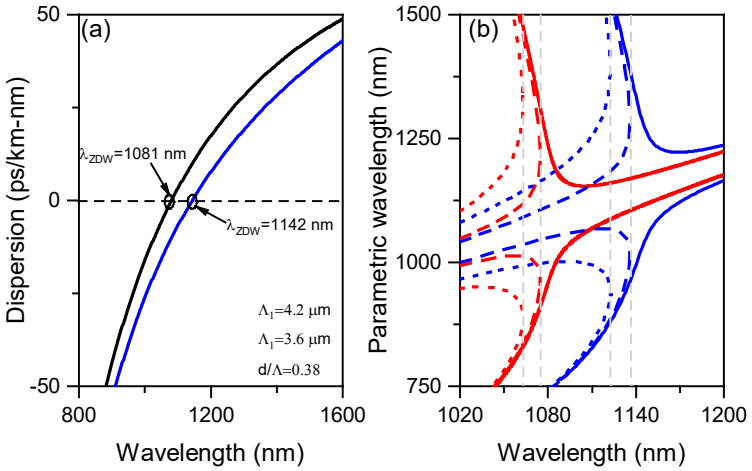

Figure 6.1. (a) Calculated chromatic dispersion of the fundamental mode for fiber 1 (black line) and fiber 2 (blue line). (b) Calculated parametric wavelengths as a function of pump wavelength; solid line shows scalar FWM wavelengths and dashed lines shows PMI wavelengths for fiber 1 (red line) and fiber 2 (blue line). PMI calculations with $\Delta n=10^{-6}$ (dashed line) and $\Delta n=10^{-5}$ (dotted line) at 1.42 kW of peak power. Dashed vertical line shows PMI cutoff wavelengths.

When the pump wavelength is far from the ZDW, PMI wavelengths are located very close to the pump while FWM bands are hundreds of nm apart from the pump wavelength. It is worth to note that when $\lambda_p << \lambda_{ZDW}$, FWM bands present a narrow gain bandwidth and the phase-matching condition is very sensitive

to the fiber properties. In realistic MOFs, often the generated bands are much broader than expected because of this effect [5].

Cutoff wavelength of slow-axis PMI is shown for the two fibers taken into account. As mentioned before, PMI cutoff occurs since the linear phase mismatch cannot compensate the phase birefringence and the nonlinear contributions when the pump wavelength is above PMI cutoff. The birefringence of the MOF directly affects the PMI cutoff wavelength. When the birefringence of the fiber is increased, the PMI cutoff wavelength occurs at shorter wavelengths and away from the ZDW. In the example of Fig. 6.1 (b), it can be seen from fiber 1 that the PMI cutoff wavelength shifts from 1074 nm to 1062 nm when the phase birefringence is increased from 1×10^{-6} to 1×10^{-5}. In the case of fiber 2, the PMI cutoff wavelength shifts from 1136 nm to 1122 nm within the considered birefringence range.

6.1 PMI and scalar FWM in liquid filled-MOFs

The experiments were performed with liquid-filled microstructured optical fibers. In this way, fine control of the refractive index of the liquid allowed achieving the required specifications of guiding properties for the simultaneous generation of both nonlinear effects. Two methods have been addressed. The first one relies on the use of ethanol-water solutions that were subsequently inserted into the fiber holes. The refractive index of the liquid was adjusted by changing the concentration. The second method is based on the thermo-optic properties of the liquid infiltrated into the MOFs. This second technique allowed a continuous and dynamic tuning of the refractive index around an initial value.

Experimental demonstration of simultaneous generation of PMI and FWM was carried out in liquid-filled MOFs that were designed and manufactured following the technique described in Chapter 3. The fibers were designed and

fabricated with the proper chromatic dispersion characteristics to achieve low dispersion value at 1064 nm wavelength when the fibers were infiltrated with ethanol-water (EtOH-H_2O) solutions.

6.1.1 Methods and experimental aspects

Solutions of EtOH-H_2O were chosen as the liquid for the fibers' infiltration because of the flexible control of the refractive index of the mixture. EtOH is completely miscible with water. The refractive index of water and ethanol at 1064 nm wavelength and room temperature are n=1.324 and 1.356, respectively. Then, by simply varying the ethanol concentration the refractive index of the solution can be adjusted (as shown in the schematic in Fig. 6.2.) in a wide range.

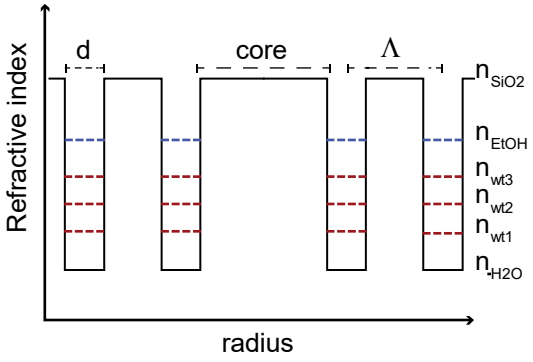

Figure 6.2. Schematic of fiber refractive index profile with fiber holes filled with EtOH-H_2O solutions.

We performed the calibration of the refractive index of EtOH-H_2O solutions used in the experiments. The experimental refractive index measurements were compared with the refractive indices of EtOH-H_2O solutions available in the literature [6–9]. Pure ethanol and deionized water (DW) were used as solute and solvent, respectively. The refractive index of each solutions was measured at room

temperature with an "ATAGO" pocket refractometer, operating at the wavelength of 589 nm.

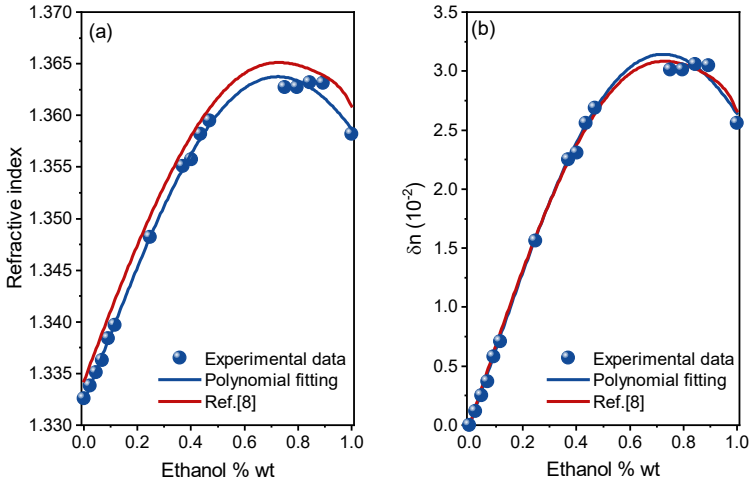

Figure 6.3. (a) Refractive index of EtOH-H_2O solutions as a function of ethanol mass fraction. (b) Refractive index increment as a function of ethanol mass fraction. Solid lines are the polynomial fit and the dots are the measured values.

Figure 6.3 (a) shows the refractive index measurement of a set of EtOH-H_2O solutions from 0 % wt to 100 % wt (weight fraction, wt). The relative error of the prepared concentrations is about 1 %, and the uncertainty of the measured refractive index is $\pm$ 3x10^{-4}. The measured values of the refractive index of the EtOH-H_2O solutions in our experiments are compared with the values reported in [8]. The small difference between both is due to the different optical wavelength of the measurements, in [8] measurements were performed at 633 nm. Good agreement is shown when we compared the refractive index increment (δn) with respect to H_2O refractive index (see Fig. 6.6(b)). The dependence of δn with the EtOH concentration shows a maximum value of ~3×10^{-2} that occurs at a concentration of 72 % wt.

The dependence of the refractive index of EtOH-H_2O solutions with optical wavelength was not characterized in our experiments and the data available in the literature is limited to few EtOH concentrations [10]. Some information on the dispersion of EtOH-H_2O through the refractive index measured at certain wavelengths can be obtained from the literature [6–8, 11–14]. The wavelength dispersion of the refractive index of the EtOH-H_2O solutions infiltrated in the MOF must be considered in the theoretical calculations of the FWM/PMI wavelengths because both effects depend on that fiber parameter. To this end, we derive the refractive index as a function of wavelength for each EtOH-H_2O solution as a solvent refractive index perturbation approximation. For each concentration, δn is used as the perturbation of the refractive index of the solvent (i.e., depending on whether the EtOH concentration is low or high). In that case, the refractive index of EtOH- H_2O as a function of wavelength can be written as:

$$n(\lambda) = n_s(\lambda) + \delta n \qquad (6.1)$$

where n_s is the refractive index of the solvent and δn is the measured refractive index increment, which is considered as wavelength independent. Sellmeier relation for the refractive index of DW and EtOH are taken from [15]. Then, the refractive index of the EtOH-H_2O solutions was estimated as follows:

(i) For solutions with low mass concentration of EtOH ($wt < 45\%$.), n_s is taken as the refractive index of DW and δn is positive.

(ii) For solutions with high mass concentrations of EtOH ($wt > 45\%$), the refractive index of EtOH is taken as n_s, therefore δn is positive.

The thermo-optical properties of the infiltrated solution were also used to obtain a fine, and in this case, we can also say that it is dynamic, adjustment of the fiber properties. This tuning technique was used with fibers filled with solutions of EtOH and H_2O with different concentrations. In the bibliography, one can find

information about the thermo-optic coefficient of this type of solutions [14, 16–20]. Thermo-optic properties of some EtOH-H_2O solutions of certain EtOH concentrations are reported, but a general result applicable to any solution is not found. Thus, we found interesting to propose a method that allows deriving the thermo-optic properties of the solutions from the experimental results.

6.1.2 Characteristics of the MOFs

The criteria followed for the design of the MOFs used in these experiments was the following: fibers with one ZDW close enough to the pump wavelength, and with normal dispersion at the pump wavelength. Actually, MOFs were designed to produce widely-spaced FWM sidebands when fiber microstructure is filled with deionized water (DW). The increase of refractive index within the holes causes the shift of the ZDW towards shorter wavelengths. Therefore, we used the addition of EtOH to the solution as a degree of freedom to achieve fine tuning of the fiber dispersion required to produce simultaneously wide spectrally-spaced FWM and PMI bands. Table 6.1 shows the structural parameters of the fibers used in these experiments. The exact cross-section profile of the fibers was measured directly from the SEM images of the fibers' cross section. Values of d and Λ are averaged values across the structure.

Table 6.1. Fiber structural parameters. The measurement error of d and Λ is about 5%.

	Structural parameters	
Fiber	**d (μm)**	**d/Λ**
MOF1	2.44	0.69
MOF2	1.63	0.63
MOF3	2.01	0.62
MOF4	1.77	0.60

6.1.3 Experimental results and discussion

Nonlinear characterization of the fibers filled with different solutions was performed. Fig. 6.4 shows two spectra obtained from MOF1; the fiber was filled with 44 wt.% EtOH-H_2O solution. The spectrum measured at the output of MOF1 exhibits four spectral bands when the fiber is pumped with 2.84 kW peak power, as shown in Fig. 6.4 (a). The pair of bands generated near the pump wavelength, located at 1008 nm and 1024 nm correspond to the anti-Stokes and Stokes wavelengths of PMI. The band generated at a longer wavelength, at 1190 nm, corresponds to the second order Stokes band of PMI. The corresponding anti-Stokes band could not be detected in the experiment, we believe because of the higher noise level of the OSA at short wavelengths. The spectral band generated near the visible region and centered at 745 nm corresponds to the *signal* band of scalar FWM. The *idler* band was not recorded since it is expected to be generated at a wavelength (estimated at 1864 nm) out of the spectral range of the spectrum analyzer (600 - 1700 nm).

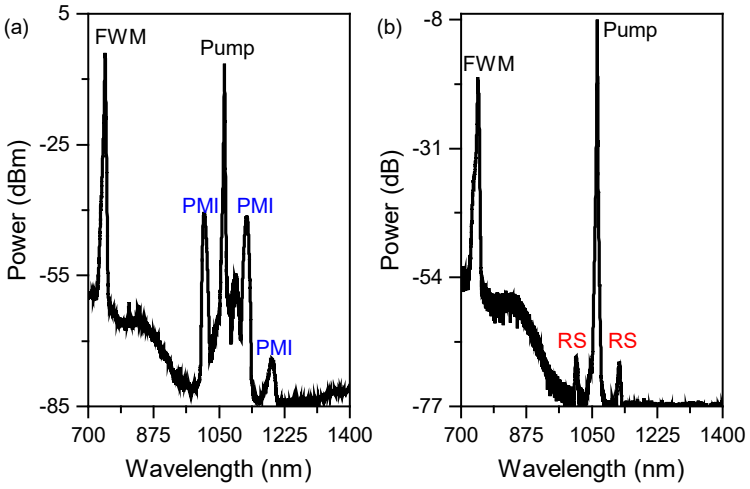

Figure 6.4. MOF1 output spectrum with: (a) slow-axis pumping and (b) fast-axis pumping.

The characteristics of the bands were studied as a function of the input polarization. By varying the pump polarization orientation, the FWM *signal* band did not show any major change, while the PMI bands' amplitude changes from a maximum value to the extinction, each 90° rotation of the polarization axis, as shown in Fig. 6.4 (b). For fast-axis pumping only Raman scattering (RS) sidebands and FWM were observed (see Fig. 6.4 (b)).

As described in Chapter 4, PMI exhibits orthogonal polarization with respect to the pump polarization, this implies that scalar FWM and PMI also exhibit orthogonal polarization to each other. The characterization of the state of polarization of the PMI sidebands and the FWM sidebands was carried out in fiber mentioned above. The experimental procedure is identical to that described in Chapter 4. Figure 6.5 shows the optical spectra generated in MOF1. The curves correspond to the spectrum obtained after the polarization analyzer, for two orientations with 90º difference. The red lines correspond to the polarizer orientation so that the amplitude of the PMI sidebands is maximum. For this orientation, spectral components with polarization oriented parallel to the fast fiber axis are transmitted by the polarizer, while the spectral components with polarization oriented to the slow axis, i.e., the pump and the FWM *signal* are attenuated by the polarizer. The opposite occurs when the polarizer is rotated by 90º (blue line), the spectral components with polarization oriented to the slow-axis are transmitted, thus the amplitude of the FWM *signal* band and the pump is maximum, while the amplitude of PMI sidebands is attenuated. In both measurements, the amplitude difference of the spectral components propagating in the slow and fast axes is about 20 dB. This transmittance difference corresponds to the typical polarization extinction ratio values achieved with the experimental setup used for the polarization characterization of optical spectra described in section 3.3.

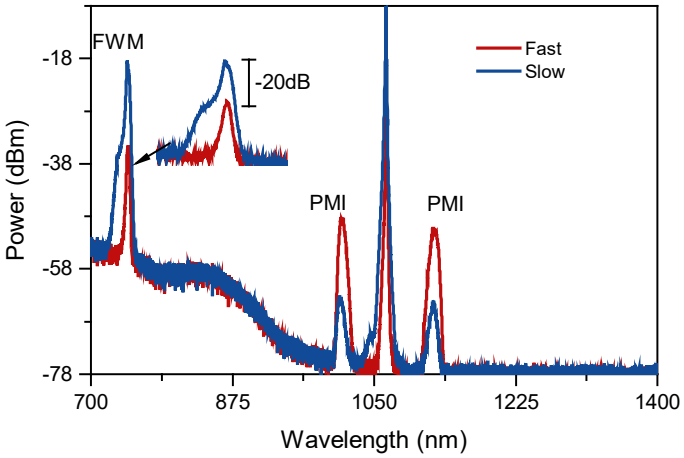

Figure 6.5. Fiber output spectra of two different polarizer orientations: (blue) polarizer orientation aligned with the slow axis, and (red) polarizer orientation aligned with the fast axis. Fiber MOF1.

Table 6.2. Dispersion, effective mode area, birefringence values at 1064 nm for MOF1 infiltrated with 44 wt.% EtOH-H2O solutions.

Fiber	D (ps/km·nm)	A_{eff} (μm^2)	Δn (10^{-6})
MOF1	-7.3	12.6	1.1

The guiding properties of MOF1, as well as the phase-matching wavelengths for scalar FWM and PMI was theoretically calculated. Calculations were performed taking into account the real cross-section of the MOF obtained from the SEM images, and the refractive index of the corresponding EtOH-H_2O solution, as well as the wavelength dispersion of the refractive indices. Table 6.2 shows the calculated values of dispersion, phase birefringence, and effective mode area of the fiber. Figure 6.6 (a) shows the dispersion characteristics, where it is shown that the ZDW was 1108 nm.

The parametric wavelengths as a function of pump wavelength for the PMI and FWM processes are shown in Fig. 6.6(b), along with the central wavelength of the bands recorded experimentally. Good agreement between theoretical calculations and experimental data is obtained.

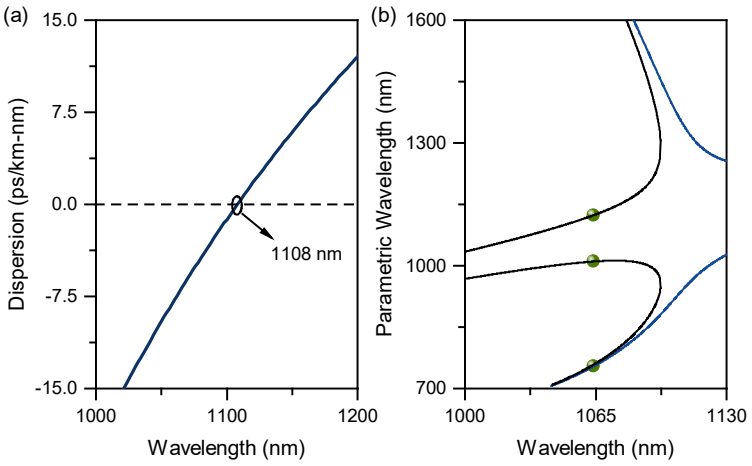

Figure 6.6. (a) Theoretical calculation of chromatic dispersion of MOF1. (b) Parametric wavelengths as a function of pump wavelength for PMI (black lines) and FWM (blue line) generated in MOF1, dots are measure values at 1064 nm.

Next, we investigated experimentally the evolution of PMI and FWM spectral sidebands generated in liquid-filled MOFs as a function of the change in the refractive index of the liquid. In the first set of experiments, a given fiber was filled sequentially with different EtOH-H_2O solutions of different weight fractions, starting from pure H_2O up to pure EtOH. The nonlinear spectral response of the fiber was recorded for each solution. Experiments were performed at room temperature. Fibers sections with lengths of 1 m were used. Throughout a series of measurements of a given fiber for the different solutions, the pump power supplied to the fiber was kept constant throughout the measurements to avoid shifting of the FWM and PMI wavelengths due to pump power variations. After fiber

characterization with a given solution, the liquid was removed from the MOF by applying gas pressure to one end of the fiber, while leaving the other end free for solution flow. We corroborated that the fibers were properly emptied by measuring again the nonlinear response of the fiber and comparing the output spectra with the spectra taken initially before fiber infiltration.

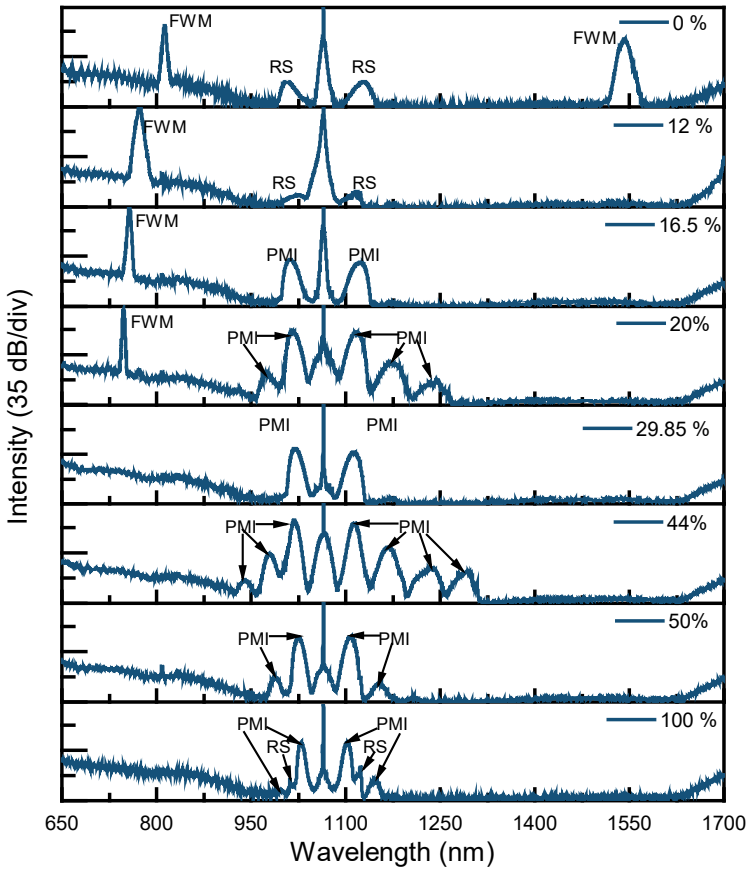

Figure 6.7. Optical spectra generated in MOF3 when fiber holes are filled with different EtOH-H_2O solutions. The EtOH mass fraction of each solution is indicated on each graph.

The optical spectra measured at the output of MOF3 when it was filled with different EtOH-H_2O solutions are plotted in Fig. 6.7. Scalar FWM was observed for

solutions with EtOH concentration up to 20 %wt. The FWM *signal* band shifted towards shorter wavelengths as the EtOH concentration of the solution was increased. It means that the frequency shift of the generated FWM photons with respect to the pump increases with concentration. The spectral shift of the FWM *signal* band was from 813 nm to 747 nm with a concentration range of EtOH-H_2O solutions from 0 %wt to 20 %wt. On the other hand, the FWM *idler* band was only detectable when the fiber was filled with pure H_2O (0 % wt EtOH concentration). The peak of the *idler* band is measured at 1542 nm for this concentration. For solutions with higher EtOH concentration, the *idler* FWM band shifted beyond 1700 nm and it was not measured experimentally.

Simultaneous generation of FWM and PMI occurs when MOF3 was filled with a concentration range of EtOH-H_2O solutions from 16.5 %wt to 20 %wt. Scalar FWM was no longer observed when the fiber was filled with EtOH concentration > 20 %wt, instead only PMI was generated. It can be observed that the anti-Stokes PMI band shifts toward longer wavelength, from 1011 nm to 1029 nm, and the Stokes band shifts toward shorter wavelengths from 1123 nm to 1103 nm (see Fig. 6.7) as the EtOH concentration was increased within the range from 16.5 %wt to 100 %wt. Therefore, PMI frequency shift decreases as the EtOH concentration was increased. Notice that, in some spectra several orders of PMI were generated (e.g., the spectrum shown in Fig. 6.7 with EtOH 44 %wt). In addition, bands generated by Raman scattering (RS) are also observed.

The experimental results obtained for fibers MOF1, MOF2 and MOF4 show a similar trend to the results obtained with fiber MOF3, although with differences in absolute values of parametric wavelengths owing to the different structural parameters of the fibers. Figure 6.8 shows the central wavelength of scalar FWM and PMI recorded experimentally for the four fibers, and for the different solutions. The spectral tuning range of scalar FWM and PMI bands achieved with each fiber

is summarized in Table 6.3. The largest range of PMI spectral shift was obtained with MOF2, the anti-Stokes band shifted from 945 nm to 1022 nm while the Stokes band shifted from 1220 nm to 1110 nm in an EtOH concentration range from 8 wt% to 100 wt%. The largest range of FWM spectral shift was obtained with MOF1, where the *signal* band shifts from 855 nm to 745 nm over a range of EtOH concentrations from 0 wt.% to 44 wt.%. The full spectral shift of the FWM *idler* band runs from 1403 nm up to 1864 nm (estimated by calculations) for this particular fiber. In most cases, it was not possible to measure the total spectral shift of the *idler* band produced in the fibers used in the experiments, so Table 6.3 shows values estimated theoretically of the spectral shift of the *idler* band.

Table 6.3. Wavelength range of FWM and PMI.

	FWM tuning range		**PMI tuning range**	
Fiber	**Signal (nm)**	**Idler (nm)**	**anti-Stokes (nm)**	**Stokes (nm)**
MOF1	855 - 745	1403 - 1616	1000 - 1029	1138 - 1102
MOF2	815 - 755	1534 - 1804 (estimated)	945 - 1022	1220 - 1110
MOF3	813 - 747	1542 – 1851 (estimated)	1011 - 1029	1123 - 1103
MOF4	785 - 750	1632 - 1833 (estimated)	960 - 1018	1194 - 1114

We investigated theoretically the evolution of the parametric wavelengths of PMI and scalar FWM in these fibers as a function of the concentration of the EtOH-H_2O solution. The comparison between experimental data and theoretical calculations of the parametric wavelengths of scalar FWM and PMI is shown in Fig. 6.8. In general terms, good agreement is obtained. The wavelength dependence of the refractive index of the solutions was taken into account in the calculations.

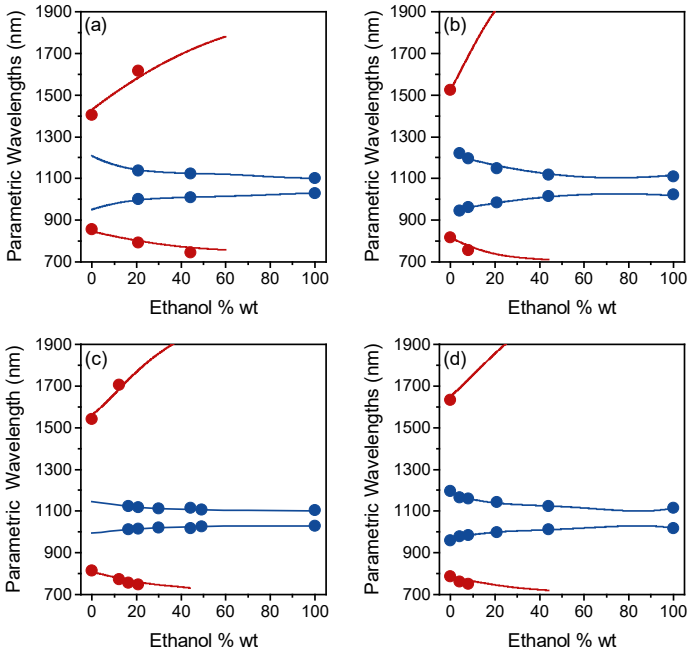

Figure 6.8. Parametric wavelengths as a function of EtOH concentration for (a) MOF1, (b) MOF2, (c) MOF3 and (d) MOF4. Dots are experimental data and solid lines are theoretical calculations. The red and blue lines are for FWM and PMI, respectively.

To give an insight about the mechanisms that produce the shift of the parametric wavelengths observed in the experiments, we investigated how the guiding parameters of the fibers change with the concentration of EtOH (that is, with the refractive index of the holes region). Figure 6.9 shows the chromatic dispersion and the phase birefringence calculations as a function of the concentration of the EtOH-H_2O solution for MOF3. The increase of EtOH concentration leads to significant changes of chromatic dispersion and phase birefringence, as shown in Fig. 6.9. The dispersion decreases with increasing EtOH concentration until an EtOH concentration value of 82 %wt, where a minimum chromatic dispersion value is reached. Over the whole range of concentration, the

change of chromatic dispersion is quite large. The maximum dispersion value is more than four times larger the dispersion value of the fiber filled with pure H_2O.

The phase birefringence of the fibers also changes substantially with the concentration. Figure 6.9(b) shows the phase birefringence variation calculated for MOF3. Changes of phase birefringence are mainly caused by changes of refractive index contrast between the core (fused silica) and microstructure that surrounds the core. It can be seen that birefringence decreases with increasing EtOH concentration of the filling solution until a minimum is reached for EtOH concentration of 76 %wt, the range of variation of birefringence is also significant, with a birefringence value at the minimum of the curve that is half the fiber birefringence with pure H_2O.

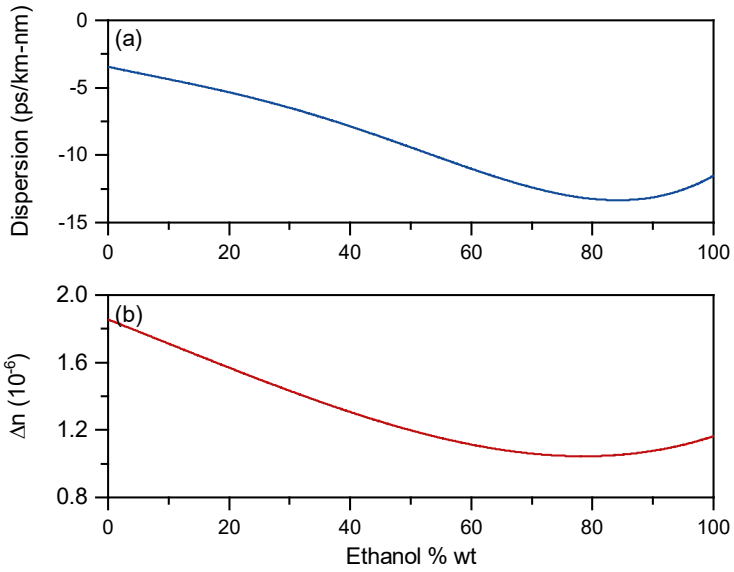

Figure 6.9. (a) Chromatic dispersion and (b) phase birefringence calculations of MOF3 as a function of EtOH mass fraction, at wavelength 1064 nm.

Changes in dispersion are known to greatly modify the frequency shift of the scalar FWM and PMI when pumping near the ZDW. In the case of FWM, the

frequency shift increases with decreasing dispersion at the pump wavelength. In the case of PMI, the opposite occurs, the frequency shift decreases with decreasing dispersion at the pump wavelength. In addition, PMI frequency shift is also affected by birefringence modifications, PMI frequency shift decreases with decreasing fiber phase birefringence. In contrast, the relative difference between the frequency shift of the FWM (slow or fast axis pumping) is nearly independent of birefringence variations for weakly birefringent fibers.

As it is shown in Fig. 6.8, theoretical calculations of parametric wavelength show that simultaneous generation of PMI and FWM can occur in fibers filled with EtOH-H_2O solutions over a wider range of concentrations than experimentally observed. For example, in most experiments no FWM was generated for EtOH-H_2O solutions higher than 21 wt%. Such disagreement with the theoretical model may be due to the degradation of the FWM efficiency when dispersion is increased (in normal dispersion regime). The origin of efficiency fall can be attributed to several factors that were not considered in the parametric wavelength calculations. When the pump wavelength is far from the ZDW, phase-matching of FWM is achieved due to GVD when β_2 is positive. Under such conditions, it was shown [21] that the gain of FWM decreases, as well as the gain bandwidth. Notice that in our experiments, the FWM *signal* band typically exhibits a bandwidth $\Delta\lambda < 2$ nm (at 3 dB) before cutoff, which can be indicative that this effect may be happening. Secondly, when the slope of the linear phase is large, FWM phase-matching is very sensitive to small fluctuations of the guiding properties along the fiber length. Finally, the generation of PMI can lead to degradation of FWM, even before the pump depletion condition since PMI occurs with higher gain for high dispersion values compared to scalar FWM, therefore, pumping photons are more likely to be harnessed by PMI than scalar FWM.

In contrast, PMI efficiency may be limited when pumping near the ZDW and the dispersion of the fiber is low at the pump wavelength. Under this condition, FWM exhibits higher gain compared to the PMI gain, therefore FWM may limit the PMI efficiency. This was observed in experiments, when MOF1 and MOF3 were filled with solutions at low EtOH concentrations, where no PMI generation was observed, instead only FWM sidebands was observed, as shown in Fig. 6.8.

6.2 Thermal tuning of FWM and PMI

Fine tuning of the scalar FWM and PMI bands simultaneously generated in MOFs filled with EtOH-H_2O solution was performed by following the tuning technique described in Chapter 5, based on the large thermo-optic properties of the liquid. Based on the results reported in the previous section, fibers filled with the appropriate EtOH-H_2O solution were chosen, in which high-amplitude FWM and PMI spectral bands were simultaneously generated. In particular, the experiments were carried out with MOF2 and MOF3, infiltrated with EtOH-H_2O solutions at concentrations of 8.1 wt.% and 16.5 wt.%, respectively. Fiber sections with a length of 1 meter were used in the experiments. At room temperature, the ZDW of these two fibers infiltrated with such solutions was calculated to be 1086 nm and 1096 nm, respectively.

The nonlinear spectral response of the fibers used in the experiments at room temperature was characterized. Figure 6.10 shows the spectrum from the two fibers. In MOF2, two orders of PMI were generated, the first order is located at 960 nm (anti-Stokes) and 1195 nm (Stokes). The FWM *signal* band is centered at 755 nm, and the *idler* band is located at 1804 nm (not shown in Fig. 6.10). Multi-order PMI generation also occurs in MOF3, the first order of PMI sidebands was measured at 1010 nm (anti-Stokes) and 1125 nm (Stokes). The spectral position of the FWM *signal* band was measured at 759 nm while the *idler* band is centered at 1782 nm.

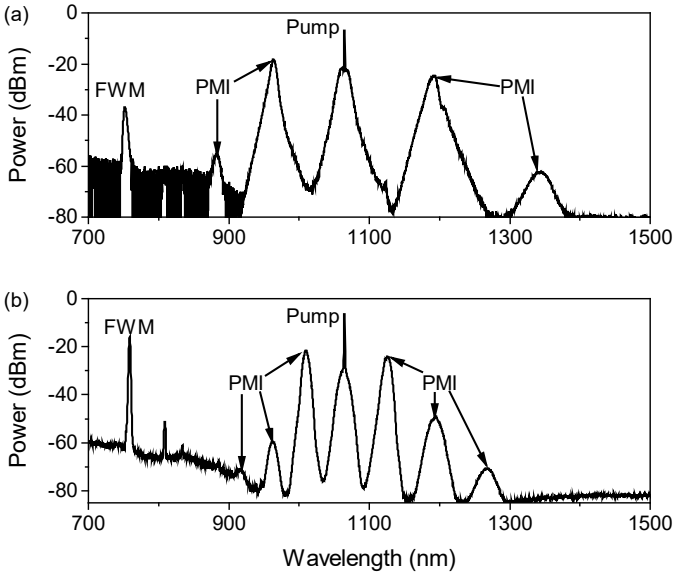

Figure 6.10. Optical spectrum for (a) MOF2 and (b) MOF3. Pump power of 2 kW and 2.3 kW, respectively.

PMI and FWM frequency shift changes produced by heating the fibers were characterized simultaneously, following the experimental procedure described in Section 5.3. Again, specially care was taken to maintain constant the pump power during a whole run of measurements. An OSA with a spectral range up to 2.2 μm was used to measure the spectral position of the FWM *idler* sideband.

The experimental results obtained with MOF2 are described in detail below. Fig. 6.11 shows the evolution of the FWM and PMI spectral bands when the temperature was increased from 23 °C (T_R) to 96 °C. The FWM sidebands shift towards the pump wavelength as the temperature was increased (see Fig. 6.11(a)-(b)), thus, FWM frequency shift decreases with increasing temperature. In particular, the *signal* band shifts to longer wavelengths, from 755 nm to 906 nm, and the *idler* band shifts to shorter wavelengths, from 1804 nm to 1279 nm, over a temperature range from T_R to 96 °C. In contrast, the PMI frequency shift increases with

increasing fiber temperature, the PMI sidebands move away from the pump wavelength as the temperature was increased, as shown in Fig. 6.11(c)-(d). Notice that the PMI exhibits a temperature threshold at 66 °C, PMI sidebands were no longer observed for higher temperatures. In particular, the anti-Stokes band of PMI shifts toward shorter wavelengths from 960 nm to 911 nm and the stokes band shifts toward longer wavelengths from 1190 nm to 1279 nm over a temperature range from T_R to 66 °C.

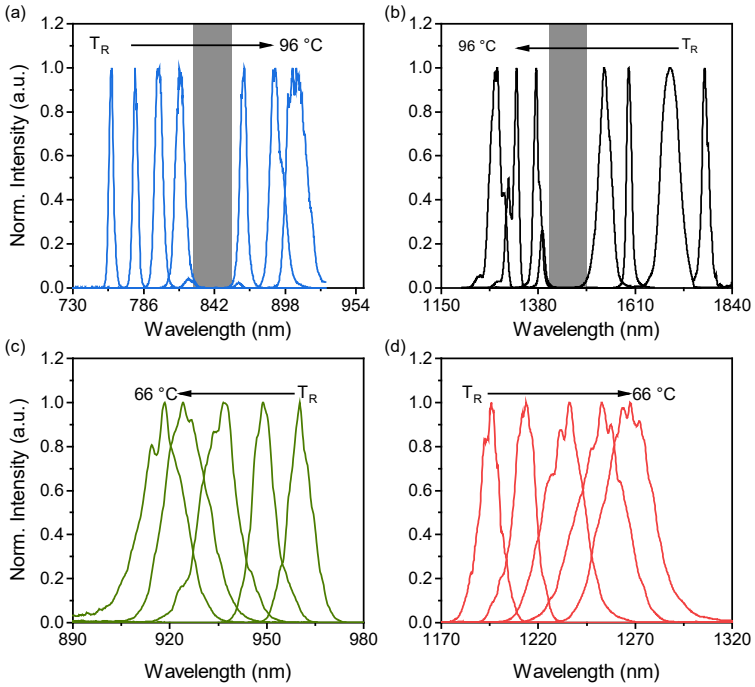

Figure 6.11. Optical spectra for different temperatures. (a) FWM *signal* band and (b) FWM *idler* band, for temperatures from T_R to 96 °C. (c) PMI anti-Stokes band and (d) PMI Stokes band, for temperatures from T_R to 66 °C.

For temperatures within a certain range, a significant effect that affect to FWM bands was observed in this particular fiber. This effect happened at temperatures between 70ºC to 85ºC. For this range of temperatures, the bands appear at

wavelengths corresponding to the shaded region of Fig. 6.11 (a)-(b) but an anomalous behavior was noticed. This effect was investigated in detail. Figure 6.12 shows the spectra of the FWM sidebands for several temperatures within that range. For temperatures above 70 °C, an additional pair of FWM sidebands is generated. For example, at 75 °C two *signal* bands with different amplitudes are produced (see Fig. 6.12(a)), the *signal* bands were measured at 815 nm (high-amplitude band) and 861 nm (low-amplitude band). The same occurs with the *idler* band, a secondary band appeared at 1390 nm for this temperature, as shown in Fig. 6.12(b). At the temperature of 80 °C, the two *signal* bands shifted towards longer wavelengths, while the relative amplitude of the two bands switches. Now the amplitude of the *signal* band of shorter wavelength is smaller while the amplitude of the band with longer wavelength is larger. For a temperature of 85 °C and above, the two bands do not longer appear, instead a single FWM *signal* band was generated. A similar behavior is shown for the FWM *idler* band.

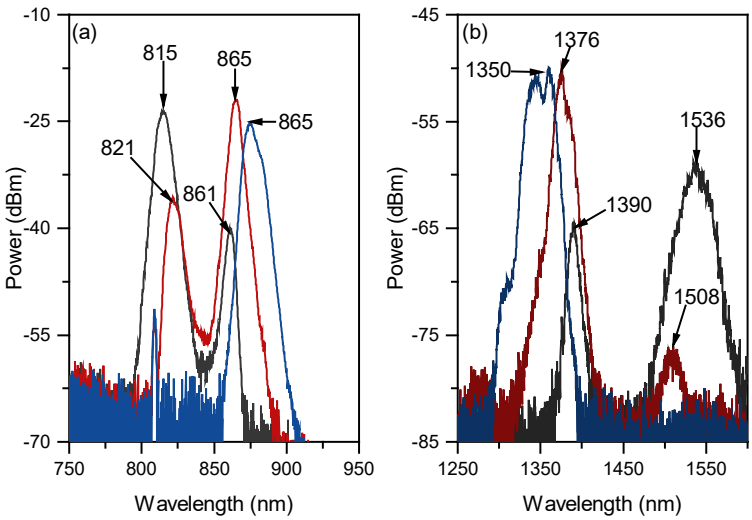

Figure 6.12. Optical spectra for 75 °C (black line), 80 °C (red line) and 85 °C (blue line). (a) *Signal* band and (b) *idler* band.

As demonstrated in Chapter 5, owing the negative TOC of the liquids infiltrated into the MOFs, the fiber dispersion decreases with temperature. Therefore, for fibers with low normal dispersion, being the case of MOF2, by increasing the temperature of the fiber, the dispersion can be tuned to relative low values. In that case, a transition on the fulfillment of the phase matching condition can be observed, and is described as follows [4]. When the fiber dispersion is low and normal at the pump wavelength, the dispersion contribution in the net linear phase is mainly attributed to the GVD parameter (β_2), so it becomes more relevant in the phase matching condition. However, when the fiber dispersion is relatively low, the β_2 parameter nearly vanishes and becomes less relevant in the phase matching condition, instead higher order dispersion terms account for the fulfillment of the FWM phase matching condition. The latter, indicates that in our experiments, for temperatures below 75 °C the outer *signal* and *idler* bands are attributed to the contribution of β_2. Conversely, for temperatures above 85 °C, the inner *signal* and *idler* bands can be attributed to the contribution of the higher order dispersion terms in the phase matching condition. In the experiments described in [22], the same trend was observed when FWM was produced in a low-normal dispersion fiber with a tunable pump laser.

The parametric wavelengths of FWM and PMI as a function of temperature for MOF2 and MOF3 are plotted in Fig. 6.13. Note that the slope of the spectral shift of FWM bands has opposite sign than that of PMI bands. This indicates that the chromatic dispersion at the pump wavelength decreases with temperature, and therefore, that the refractive index of the EtOH-H_2O solution decreases with temperature, which confirms a negative TOC value of EtOH-H_2O solutions, as expected since both solvent (H_2O) and solute (EtOH) exhibit a negative TOC.

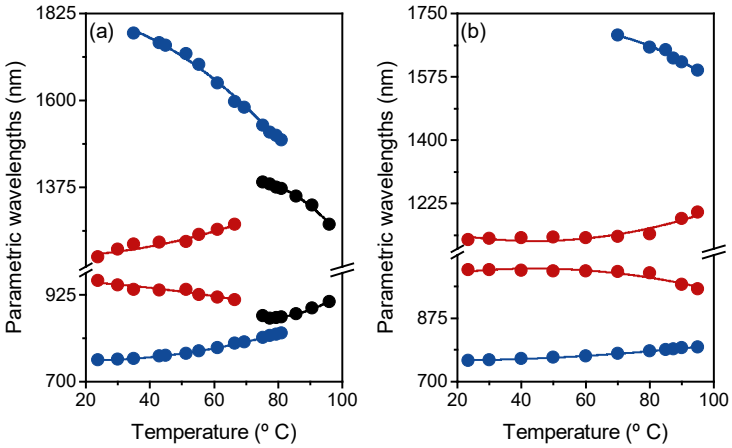

Figure 6.13. Parametric wavelengths as a function of temperature for (a) MOF2 and (b) MOF3. The spectral position of the FWM and PMI are represented by blue and red dots, respectively. The black dots show the wavelengths of the FWM when higher-order dispersion terms govern in the phase-matched condition. The lines are guides to the eye.

The thermal characterization of MOF3 is shown in Fig. 6.13(b), similar experimental results were obtained as described with MOF2, although the phase-matching condition fulfilled with HOD was not observed during the experimental characterization of MOF3. The spectral tuning range of PMI and FWM is summarized in Table 6.4. The experimental results show that the tuning range of FWM and PMI obtained with MOF2 is larger than the tuning range obtained with MOF3.

Table 6.4. Spectral tuning range of FWM and PMI sidebands.

	FWM tuning range		**PMI tuning range**	
Fiber	**Signal (nm)**	**Idler (nm)**	**anti-Stokes (nm)**	**Stokes (nm)**
MOF2	755 - 907	1774 – 1279	960 - 911	1196 - 1279
MOF3	759 - 796	1689 – 1592	1010 – 956	1125 - 1200

6.3 Applications of FWM for the characterization of the optical properties of liquids

6.2.1 Refractometry

The results included in this chapter can be exploited for the development of practical applications. The dependence of FWM/PMI wavelengths in liquid-filled MOFs with the refractive index of the liquid can be used for the development of highly sensitive refractometers for water-based solutions. From the experimental results we can conclude that FWM bands show a larger sensitivity with the refractive index than PMI bands. In addition, the FWM bands are narrower than PMI bands. Therefore, we propose to base the refractometer on the response of FWM, in particular on the FWM *signal* band.

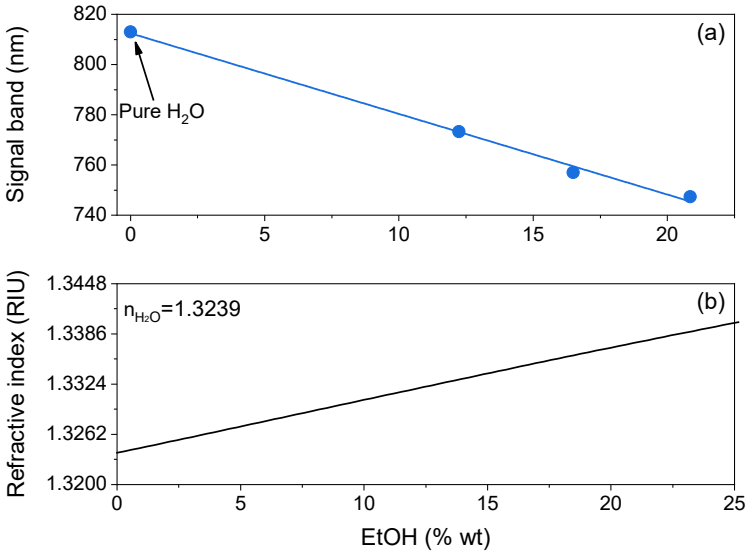

Figure 6.14. (a) Spectral response of *signal* band of FWM as a function of EtOH concentration, for MOF3. (b) Refractive index of the solution as a function of EtOH concentration.

We take as an example the results obtained with MOF3 with different solutions of EtOH-H_2O with EtOH concentration from 0 %wt. to 21 %wt. The central wavelength of the *signal* band as function of the EtOH concentration is shown in Fig. 6.14(a). It is seen that, within this range of EtOH concentrations, the *signal* band wavelength shifts linearly with the solution concentration. The refractive index of EtOH-H_2O solutions for this range of concentrations shows also a quite good degree of linearity (see Fig. 6.14(b)). The above concentration range corresponds to a change in refractive index from 1.324 to 1.337.

The linearity of both quantities simplifies the calibration response of the sensor. According to the slopes of both, the FWM *signal* band shifts at a rate of 4944 nm/RIU. On the other hand, the detection limit of the sensor, that is, the smallest refractive index change that can be detected depends on the sensitivity but also on the spectral width of the band, and on the spectral resolution of the spectrometer use to carry out the measurement. Assuming that the minimum band's wavelength shift that can be detected is equal to one tenth (0.3 nm) of the band width, the smallest change of refractive index that can be detected is $6 \cdot 10^{-5}$ RIU. This detection limit is higher than that of fiber optic refractive index sensors based on interferometry ($\sim 10^{-4}$) reported in [12, 23–25] and comparable with refractive index sensor based on FWM, surface plasmon resonances, and evanescence fields in tapered fibers ($\sim 10^{-5}$) reported in [13, 26–31] and on fiber Bragg gratings, ($\sim 10^{-5}$) as reported in [32, 33].

6.2.2 Thermo-optic characterization of liquids

In this section, we address the determination of thermo-optic properties of a liquid based on the shift of the *signal* FWM band with temperature. To illustrate such application, we use the results obtained with MOF3 infiltrated with an EtOH-H_2O

solution with EtOH concentration of 16.5 %wt. Therefore, thermo-optic characteristic of 16.5 %wt. EtOH-H_2O is obtained.

Figure 6.15 (a) summarizes the response of the FWM *signal* band with the fiber temperature, from 23°C (T_R) to 96 °C. The *signal* band shifts toward longer wavelengths (redshift) with increasing fiber temperature. It is clear that the band's shift is not linearly dependent on temperature.

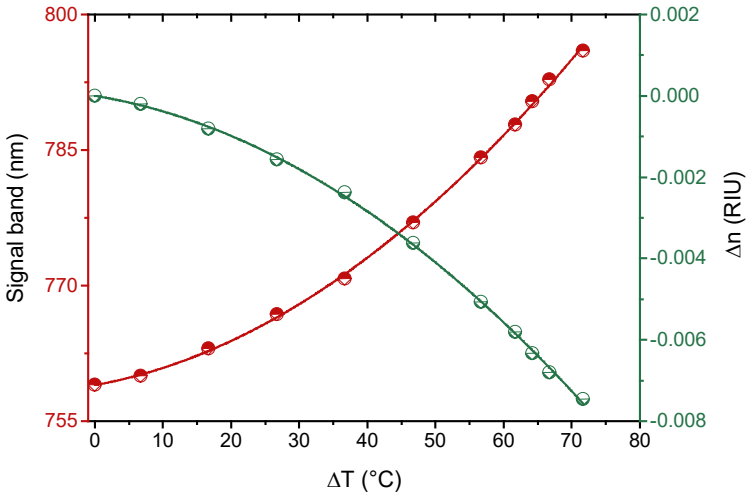

Figure 6.15. Spectral shift of *signal* band as a function of temperature increment (red dots). Refractive index in the fiber holes required to match the wavelength of the theoretical FWM *signal* to the experimental data (green dots). Solid lines are second-order polynomial fitting.

The FWM parametric wavelengths were calculated theoretically for MOF3 as a function of the refractive index of the holes. Refractive index values taken in the calculations were fitted in order the theoretical FWM *signal* wavelength to match the experimental data. Figure 6.15 includes the refractive index values that yield to the best agreement between experimental data and theoretical calculations.

Table 6.5. Refractive index fitting parameters of the EtOH-$H_2$16.5% wt. solution. *T* is the temperature in Celsius and T_R=23ºC

$$n = n_0 + a \cdot (T - T_R) + b \cdot (T - T_R)^2$$

n_0	a	b	R
1.335	-2.75×10^{-5}	-1.09×10^{-6}	0.999

It can be seen that the refractive index change that would cause the shift of the FWM *signal* band observed experimentally decreases with temperature. However, the refractive index change is not proportional to the temperature increase. A second-order polynomial function was fitted to the values of refractive index. Table 6.5 shows the fitting parameters. The thermo-optic properties of the EtOH-H_2O solution were determined by the derivative of the refractive index with temperature, resulting,

$$\frac{dn}{dT} = -\left(2.75 + 0.22 \cdot (T - T_R)\right) \times 10^{-5} \qquad (6.2)$$

In the literature, different techniques are reported to measure the thermo-optic properties of EtOH-H_2O solutions [17–20, 30, 31]. The thermo-optic properties of solutions similar to the one analyzed here previously reported in [18, 20], are in good agreement with the result shown in this work. In particular, the nonlinear dependence of refractive index with temperature of EtOH solutions observed in our experiments, which is somehow surprising since pure EtOH and pure H_2O are linearly dependent with temperature, was already described in [18–20].

References

1. R. J. Kruhlak, G. K. Wong, J. S. Chen, S. G. Murdoch, R. Leonhardt, J. D. Harvey, N. Y. Joly, and J. C. Knight, "Polarization modulation instability in photonic crystal fibers," Opt. Lett. **31**, 1379 (2006).

2. S. G. Murdoch, R. Leonhardt, and J. D. Harvey, "Polarization modulation instability in weakly birefringent fibers," Opt. Lett. **20**, 866 (1995).

3. G. Millot, E. Seve, S. Wabnitz, and M. Haelterman, "Observation of induced modulational polarization instabilities and pulse-train generation in the normal-dispersion regime of a birefringent optical fiber," J. Opt. Soc. Am. B **15**, 1266 (1998).

4. G. Agrawal, "Chapter 10 - Four-Wave Mixing," in *Optics and Photonics*, G. B. T.-N. F. O. (Fifth E. Agrawal, ed. (Academic Press, 2013), pp. 397–456.

5. M. Ajmani and P. Singh, "FWM in WDM system, effects and techniques to minimize: A review," Int. Conf. Adv. Comput. Commun. Technol. ACCT **2015**-**April**, 385–389 (2015).

6. C. Moreno-Hernandez, O. R. Quiroz, D. Monzon-Hernandez, and J. Villatoro, "Contactless Optical Fiber Interferometric Sensor to Monitor Water Content in Ethanol," IEEE Sens. J. **18**, 3211–3217 (2018).

7. F. K. Coradin, G. R. C. Possetti, R. C. Kamikawachi, M. Muller, and J. L. Fabris, "Etched fiber Bragg gratings sensors for water-ethanol mixtures: A comparative study," J. Microwaves Optoelectron. **9**, 131–143 (2010).

8. A. A. Ghoreyshi, F. A. Farhadpour, M. Soltanieh, and A. Bansal, "Transport of small polar molecules across nonporous polymeric membranes: I. Experimental procedures and data analysis," J. Memb. Sci. **211**, 193–214 (2003).

9. S. Taue, Y. Matsumoto, H. Fukano, and K. Tsuruta, "Experimental analysis of optical fiber multimode interference structure and its application to refractive index measurement," Jpn. J. Appl. Phys. **51**, (2012).

10. H. Sobral and M. Peña-Gomar, "Determination of the refractive index of glucose-ethanol-water mixtures using spectroscopic refractometry near the critical angle," Appl. Opt. **54**, 8453 (2015).

11. T. A. Scott, "Refractive index of ethanol-water mixtures and density and refractive index of ethanol-water-ethyl ether mixtures," J. Phys. Chem. **50**, 406–412 (1946).

12. Y. L. Yeh and Y. P. Lin, "High-precision measurement system based on laser interferometer for determining alcohol concentration of liquid solution," Opt. Commun. **281**, 744–749 (2008).

13. S. K. Srivastava, R. Verma, and B. D. Gupta, "Surface plasmon resonance based fiber optic

sensor for the detection of low water content in ethanol," Sensors Actuators, B Chem. **153**, 194–198 (2011).

14. R. J. Jiménez Riobóo, M. Philipp, M. A. Ramos, and J. K. Krüger, "Concentration and temperature dependence of the refractive index of ethanol-water mixtures: Influence of intermolecular interactions," Eur. Phys. J. E **30**, 19–26 (2009).

15. S. Kedenburg, M. Vieweg, T. Gissibl, and H. Giessen, "Linear refractive index and absorption measurements of nonlinear optical liquids in the visible and near-infrared spectral region," Opt. Mater. Express **2**, 1588 (2012).

16. G. Ghosh, "Handbook of Thermo-Optic Coefficients of Optical Materials with Applications," Chem. & **5**, 368 (1998).

17. C.-L. Lee, H.-Y. Ho, J.-H. Gu, T.-Y. Yeh, and C.-H. Tseng, "Dual hollow core fiber-based Fabry–Perot interferometer for measuring the thermo-optic coefficients of liquids," Opt. Lett. **40**, 459 (2015).

18. M. S. Ferreira, S. Novais, and J. L. Pinto, "Optical fiber tip sensor for determining the thermo-optic coefficient of ethanol-water mixtures," Opt. InfoBase Conf. Pap. **Part F124**-, 1–4 (2018).

19. R. C. Kamikawachi, I. Abe, A. S. Paterno, H. J. Kalinowski, M. Muller, J. L. Pinto, and J. L. Fabris, "Determination of thermo-optic coefficient in liquids with fiber Bragg grating refractometer," Opt. Commun. **281**, 621–625 (2008).

20. S. Novais, M. S. Ferreira, and J. L. Pinto, "Determination of thermo-optic coefficient of ethanol-water mixtures with optical fiber tip sensor," Opt. Fiber Technol. **45**, 276–279 (2018).

21. S. Song, C. T. Allen, K. R. Demarest, and R. Hui, "Intensity-dependent phase-matching effects on four-wave mixing in optical fibers," J. Light. Technol. **17**, 2285–2290 (1999).

22. L. Zhang, T. H. Tuan, H. Kawamura, T. Suzuki, and Y. Ohishi, "Optical parametric oscillator based on degenerate four-wave mixing in suspended core tellurite microstructured optical fiber," Opt. Express **23**, 26299 (2015).

23. L. Cai, Y. Zhao, and X. gang Li, "A fiber ring cavity laser sensor for refractive index and temperature measurement with core-offset modal interferometer as tunable filter," Sensors Actuators, B Chem. **242**, 673–678 (2017).

24. J. N. Wang and J. L. Tang, "Photonic crystal fiber Mach-Zehnder interferometer for refractive index sensing," Sensors **12**, 2983–2995 (2012).

25. S. Taue, Y. Matsumoto, H. Fukano, and K. Tsuruta, "Experimental analysis of optical fiber multimode interference structure and its application to refractive index measurement," Jpn. J. Appl. Phys. **51**, (2012).

26. P. Wang, G. Brambilla, M. Ding, Y. Semenova, Q. Wu, and G. Farrell, "High-sensitivity, evanescent field refractometric sensor based on a tapered, multimode fiber interference," Opt. Lett. **36**, 2233 (2011).

27. W. Bin Ji, S. C. Tjin, B. Lin, and C. L. Ng, "Highly sensitive refractive index sensor based on adiabatically tapered microfiber long period gratings," Sensors (Switzerland) **13**, 14055–14063 (2013).

28. H. Hu, X. Song, Q. Han, P. Chang, J. Zhang, K. Liu, Y. Du, H. Wang, and T. Liu, "High Sensitivity Fiber Optic SPR Refractive Index Sensor Based on Multimode-No-Core-Multimode Structure," IEEE Sens. J. **20**, 2967–2975 (2020).

29. M. H. Frosz, A. Stefani, and O. Bang, "Highly sensitive and simple method for refractive index sensing of liquids in microstructured optical fibers using four-wave mixing," Opt. Express **19**, 10471 (2011).

30. Y. Geng, L. Wang, X. Tan, J. Wang, Y. Du, and X. Li, "A highly sensitive four-wave mixing-based microstructured fiber refractive index sensor for microfluid sensing applications," Appl. Phys. Express **12**, 0–4 (2019).

31. Y. Geng, L. Wang, Y. Xu, A. G. Kumar, X. Tan, and X. Li, "Wavelength multiplexing of four-wave mixing based fiber temperature sensor with oil-filled photonic crystal fiber," Opt. Express **26**, 27907 (2018).

32. T. Wang, K. Liu, J. Jiang, M. Xue, P. Chang, and T. Liu, "Temperature-insensitive refractive index sensor based on tilted moiré FBG with high resolution," Opt. Express **25**, 14900 (2017).

33. W. Liang, Y. Huang, Y. Xu, R. K. Lee, and A. Yariv, "Highly sensitive fiber Bragg grating refractive index sensors," Appl. Phys. Lett. **86**, 1–3 (2005).

Chapter 7
Conclusions

In this thesis, we have focused on the study of the optical nonlinear effect of vector FWM in optical fibers, and on the development of feasible mechanisms for broadband tuning of FWM sidebands generated (mostly) in nonlinear MOFs. The aim of this work was to produce the knowledge, and a set of techniques to support the development of versatile multiband optical fiber light sources based on this nonlinear effect. This study has been organized in two main stages. In the first part, we have presented a detailed study, both theoretical and experimental of the nonlinear effects of PMI and FWM that can be produced in optical fibers. This study has allowed us to identify the fiber parameters that determine the main features of PMI and FWM effects. Engineering of such fiber parameters has enabled the control of the spectral location of the sidebands produced through these nonlinear effects. The second part was devoted to the development of simple methods to tune the PMI and FWM sidebands by acting on the fiber properties, in particular on chromatic dispersion and birefringence. Control of these fiber parameters was achieved through dynamic methods triggered by the elasto-optic and thermo-optic effects.

In Chapter 2, we have provided the theoretical description of the nonlinear effect of FWM in optical fibers. We have derived the equations for coupled amplitudes, phase-matching, and gain that describe the FWM effect for isotropic and weakly birefringent fibers taking into account the vector nature of light. This

study allowed us investigating the contribution of the different fiber parameters. This theoretical framework provided a detailed description of FWM and PMI in the collection of MOFs that were used for this thesis. Therefore, we were able to compare the experimental results with the theoretical simulations with relatively good agreement.

The mode solver for complex 2D structures detailed in Chapter 3 allowed us to design MOFs with properties suitable for the experiments designed in this thesis. By following the *stack-and-draw* technique, we were able to fabricate the designed nonlinear MOFs according to each particular application or experiment. The general experimental setup used throughout this thesis has allowed us to efficiently excite and characterize the effects of FWM and PMI.

Regarding the experimental part of this thesis, in Chapter 4, we have studied in detail PMI produced in MOFs with different chromatic dispersion characteristics under quasi-CW pump at 1064 nm. In particular, we have characterized the PMI produced by slow-axis pumping in a broad family of MOFs, including air-filled, ethanol-filled, and D_2O-filled MOFs. The investigated fibers were designed to present different dispersion profiles covering fibers with 1-ZDW, 2-ZDW and ANDi type fibers. In the case of ANDi fibers, we have shown, for the first time, that the largest frequency shift of PMI sidebands occurs when the pump wavelength matches the MDW. The largest value of PMI frequency shift measured in this type of fibers was $\Omega = 1538\ cm^{-1}$ in a fiber with $MDW = 1058\ nm$. We would like to remark that scalar case of FWM/MI is forbidden in ANDi fibers since phase-matching cannot be accomplished for that type of fiber. Instead, only PMI can be generated, which was also corroborated with our experiments.

Furthermore, we have demonstrated that large PMI frequency shift can be attained in fibers with 1- or 2-ZDW when the fiber dispersion is low. This condition can be accomplished, for instance, when the excitation wavelength is close to the

ZDW. In our experiments, we were unable to excite PMI produced in fibers with 2-ZDW when the dispersion of the fiber at the pump wavelength is anomalous or in the second normal dispersion region, beyond the second ZDW. For this, lasers emitting at longer wavelengths with sufficient pump power will be needed. To our knowledge, PMI produced in fibers with 2-ZDW has not been reported and may be of interest for soliton dynamics in optical fibers.

The set of experimental results included in Chapter 4 allowed us pointing out the relevance of the fiber birefringence for the fulfillment of the phase-matching condition for PMI. This was concluded after comparing the results obtained with fibers with similar dispersion values at the excitation wavelength, but different birefringence. A larger birefringence results in a larger PMI frequency shift.

In the second experimental part of this thesis, the ability to control the spectral location of the PMI and FWM sidebands was addressed. In Chapter 5, we have shown different methods that allowed tuning the PMI sidebands produced in MOFs and in standard optical fibers over a wide frequency range. We developed simple methods to control the birefringence and dispersion of the fiber, and we exploited such feature to manage the spectral position of the PMI sidebands. First, the birefringence of an optical fiber was controlled by the elasto-optic effect, by pure fiber bending, and by tensioning-and-coiling the fiber on cylindrical molds. These experiments were performed with standard step-index optical fibers that exhibit extremely low residual birefringence when the fibers are kept straight. By pure bending, a PMI frequency shift range from 111 cm^{-1} to 779 cm^{-1} was achieved by varying the birefringence of the fiber from 4.6×10^{-7} to 3.9×10^{-5}. The results obtained with the tensioning-and-coiling technique were poorer. The frequency tuning range of the PMI sidebands achieved in our experiments ranged from 621 cm^{-1} to 726 cm^{-1} for a strain range from 3.8×10^{-3} to 5.0×10^{-3}. Although this technique allows the possibility to induce large birefringence variations in the fiber, it is mostly limited to

the use of large bending radii that allow coiling and tensioning the fibers without reaching the breaking point. Our results pointed out that the elastic properties of the fiber polymer coating produced a damping effect that reduces significantly the birefringence induced by tensioning-and-coiling the fiber. Taking advantage of the direct relationship between PMI frequency shift and birefringence in a fiber with large value of normal dispersion at the pump wavelength, we were able to estimate the actual strain applied into the tensioned-coiled fibers. We want to point out that PMI effect in optical fibers can be exploited for the characterization of the fiber properties. Based on PMI, fiber parameters such as the nonlinear coefficient, the birefringence, or the chromatic dispersion can be determined. In particular, we have demonstrated that PMI generated bands in fibers pumped at wavelength at which the dispersion of the fiber is large and normal, can exhibit narrow gain bandwidth (~0.5 nm), thus, accurate measurements can be obtained based on PMI.

The second part of Chapter 5 is devoted to the tuning of PMI sidebands by controlling the fiber birefringence and dispersion through thermal effects. In this regard, we have been able to tune high amplitude PMI sidebands over a wide frequency range by varying the fiber temperature. We have shown that thermal control of such fiber parameters is particularly efficient in MOFs filled with liquids with suitable optical properties. In particular, in our experiments, ethanol and heavy water were used as filling liquids. Due to the large thermo-optic coefficient of such substances, moderate temperature changes can lead to large changes of both, fiber chromatic dispersion and birefringence. The best result obtained with an ethanol-filled MOF showed the tuning of PMI frequency shift from 1274 cm^{-1} to 2189 cm^{-1} over a temperature range of 20 °C to 60 °C. The largest tuning range obtained with a heavy water-filled MOF run from 1084 cm^{-1} to 2786 cm^{-1} over a temperature range of 20 °C to 90 °C. The latter was the largest tuning range of PMI bands achieved in our experiments.

Additionally, some other aspects were pointed out by this set of experiments. For instance, it is shown that the sensitivity of PMI wavelengths to changes of fiber properties is particularly significant when the pump wavelength is close to the ZDW and so the dispersion of the fiber at the pump wavelength is low. On the other hand, the ability for fine tuning the fiber properties provided by its thermal response allowed us to investigate, and experimentally demonstrate the existence of the cutoff wavelength for PMI.

The tuning range of PMI sidebands achieved with this technique almost covered the vibrational frequencies (from 1000 cm^{-1} to 3700 cm^{-1}) of most representative functional groups for bioimaging used in advanced Raman microscopy. Furthermore, we would like to emphasize that PMI sidebands produced in liquid-filled MOFs were able to excite Raman scattering photons by themselves, indicating that the intensity of the PMI bands can be remarkably high. Therefore, we can conclude that PMI can be a suitable physical mechanism for the development of high performance polarized narrow-band light sources with low background noise.

Chapter 6 compiles our studies regarding the dual generation of FWM and PMI in MOFs and the feasibility of simultaneous tuning of the sidebands produced by both nonlinear effects. The fiber specifications for the simultaneous generation of both nonlinear effects required fine adjustment of the guiding properties, which was achieved using MOFs filled with ethanol-water solutions. Characterization of the polarization of the resulting light spectra at the output of the MOFs allowed us to identify the PMI and FWM spectral sidebands.

We were able to control simultaneously the spectral position of the sidebands produced by such nonlinear effects by means of two methods. The first is based on filling the holes of the MOF with ethanol-water solutions of different concentrations. The refractive index of the solutions was dependent on the EtOH

concentration, thus, birefringence and chromatic dispersion, and therefore the spectral location of PMI and FWM sidebands generated, was varied as a function of the ethanol (EtOH) concentration of the solution infiltrated into the MOF. The second method is based on the thermo-optic properties of the liquid infiltrated into the MOF similar to the technique employed in Chapter 5.

Regarding the results obtained by means of the first method, we were able to control the FWM sidebands over a wide range of frequencies. We have experimentally shown that the frequency shift of FWM increases with EtOH concentration, while it decreases for PMI, as predicted theoretically. Frequency shift of FWM ranging from 2302 cm^{-1} to 4028 cm^{-1} was demonstrated, for solutions of EtOH concentration from 0 %wt to 44 %wt. PMI sidebands were produced with frequency shift spanning from 391 cm^{-1} to 1188 cm^{-1}, for solutions with EtOH concentration ranging from 8 %wt to 100 %wt. Certainly, the frequency shift of FWM and PMI sidebands was managed by controlling the refractive index of the liquid infiltrated into the holes of a MOF. However, this method is not dynamic in the sense that tuning the location of the PMI/FWM bands requires filling and emptying the MOFs.

The second method allowed simultaneous broadband tuning of PMI and FWM sidebands in a dynamic way. The refractive index of a given solution infiltrated into de fiber was continuously tuned around an initial value set by the ethanol-water concentration by taking advantage of the thermo-optic effect. Using this technique, we were able to produce high amplitude, widely spectrally spaced PMI and FWM sidebands in MOFs, and to continuously and dynamically tune them by changing the fiber temperature. The largest frequency shift tuning range were, for FWM from 3851 cm^{-1} to 1631 cm^{-1} over a temperature range of 23 °C to 96 °C, and for PMI from 1023 cm^{-1} to 1583 cm^{-1} over a temperature range of 23 °C to 66 °C. We have shown that the PMI frequency shift increases with fiber temperature, while the

FWM frequency shift shows the opposite trend with increasing fiber temperature, which was expected owing to the negative temperature coefficient of the solution. We can emphasize that the polarization properties of PMI and FWM can lead to various combinations of tunable photonic light sources simply by filtering the desired wavelengths with suitable optical devices, such as polarizers or bandpass filters. In addition, for applications where polarization effects are negligible, a narrow-band light source covering nearly the near-infrared spectrum can be based on the combination of the FWM and PMI sidebands.

Finally, in Chapter 6 we include two practical applications based on the response of the FWM *signal* band to changes of refractive index and/or temperature. In liquid-filled MOFs, the dependence of the FWM wavelengths on the refractive index of the filling liquid can be used for the development of highly sensitive refractometers for water-based solutions. We have shown that, compared to PMI bands, FWM bands show a larger sensitivity to refractive index or temperature. In addition, with proper fiber dispersion design, FWM sidebands can be narrower than PMI bands, which normally leads to better detection limits. In a particular implementation, we measured the wavelength shift of the *signal* band with the change of the refractive index of the liquid when it was varied from 1.324 to 1.337. A linear response of both quantities (i.e., refractive index and wavelength shift) was observed with the EtOH concentration. High sensitivity (4944 nm/RIU) was obtained with the sensor calibration response.

The second application is related to the characterization of the thermo-optic properties of liquids. The method exploits the thermal response of the FWM *signal* band produced in a MOF filled with the liquid under test. To show the viability of the proposal, an ethanol-water solution was investigated. The method was able to show (and quantify) the nonlinear dependence of the refractive index of such solutions with temperature. This technique can be extended to characterize the

thermo-optic response of many other liquids, provided that the refractive index of the liquid be lower than the refractive index of silica.

Throughout this thesis, several ideas for different experiments and applications based on PMI/FWM have emerged as future work. For example, with the technique used to tune the PMI sidebands through mechanical deformation. We have shown that the frequency shift of PMI induced by birefringence changes allows the feasibility of measuring the deformation or bending of an optical fiber. In addition, parameters of a fiber, such as birefringence or nonlinear parameter, can also be measured based on the PMI frequency shift response. In the same direction, we have previously pointed out the possibility of developing fiber sensors based on the response of FWM to variations in the refractive index of a liquid infiltrated into the holes of a MOF and the possibility of characterizing the thermal response of a wide variety of water-based solutions. Finally, we would like to emphasize that the FWM/PMI tuning techniques and tuning ranges shown in this work are well suited for the development of light sources for advanced microscopy.

Publications

Articles in journals

- A. Loredo-Trejo, Y. López-Diéguez, L. Velázquez-Ibarra, A. Díez, E. Silvestre, J. M. Estudillo-Ayala, and M. V. Andrés, "Polarization Modulation Instability in All-Normal Dispersion Microstructured Optical Fibers with Quasi-Continuous Pump," IEEE Photonics J. **11**, (2019).

- A. Loredo-Trejo, A. Díez, E. Silvestre, and M. V. Andrés, "Broadband tuning of polarization modulation instability in microstructured optical fibers," Opt. Lett. **45**, 4891 (2020).

- A. Loredo-Trejo, A. Díez, E. Silvestre, and M. V. Andrés, "Polarization modulation instability in dispersion-engineered photonic crystal fibers," Crystals **11**, 365 (2021).

- A. Loredo-Trejo, A. Díez, E. Silvestre, and M. V. Andrés, " Broad and simultaneous tuning of four-wave mixing and polarization modulation instability in microstructured optical fibers.," *In preparation.*

Communications to conferences

Oral Contributions

- Loredo-Trejo, Y. López-Dieguez, A. Díez and M. V. Andrés, "Analysis of polarization modulation instability in all-normal dispersion photonic crystal fibers", XII Reunión Nacional de Óptica (RNO 2018), pp. 137, Castellón, 2018.
- Y. López-Dieguez, L. Velázquez-Ibarra, A. Loredo-Trejo, A. Díez and M. V. Andrés, "Experimental observation of polarization modulation Instability in all-normal dispersion photonic crystal", XII Reunión Nacional de Óptica (RNO 2018), pp. 138, Castellón, 2018.
- A. Loredo-Trejo, Y. López-Diéguez, L. Velázquez-Ibarra, A. Díez, E. Silvestre, M. V. Andrés, "Polarization modulation instability in all-normal dispersion microstructured optical fibers with sub-ns pumping", International conference of transparent optical network (ICTON 2019), We. E6.5, Anger, 2019, (Invited).
- A. Loredo-Trejo, Y. López-Diéguez, L. Velázquez-Ibarra, A. Díez, E. Silvestre, M. V. Andrés, "Experimental observation of polarization modulation instability in all-normal dispersion photonic crystal fibers", X Reunión Iberoamericana de Óptica (RIAO 2019), pp. 110-111, Cancún, 2019.
- A. Loredo-Trejo, A. Díez, E. Silvestre, M. V. Andrés, "Broadband tuning of polarization modulation instability in microstructured optical fiber through thermal heating", OSA Advanced Photonics Congress, NpM2D.4, Washington, 2020.

- A. Loredo-Trejo, A. Díez, E. Silvestre, M. V. Andrés, "Widely Tunable Polarization Modulation Instability in D_2O-Filled Microstructured Optical Fiber", Conference on Lasers and Electro-Optics Europe & European Quantum Electronics Conference (CLEO/Europe-EQEC), cd_7_5, Munich, 2021.
- A. Loredo-Trejo, A. Díez, E. Silvestre, M. V. Andrés, "Simultaneous Generation and Tuning of Four-Wave Mixing and Polarization Modulation Instability in Microstructured Optical Fiber", OPTICA, Advanced Photonics Congress, paper accepted, Netherlands, July 2022.

Poster Contributions

- A. Diez, A. Loredo-Trejo, Y. López-Diéguez, L. Velázquez, Miguel V. Andrés, "Theoretical and experimental study of polarization modulation instability in all-normal dispersion photonic crystal fibers", OSA Latin America Optic & photonics conference (LAOP 2018), Tu4A.3, Lima, 2018.
- A. Loredo-Trejo, Y. López-Diéguez, L. Velázquez-Ibarra, A. Díez, E. Silvestre, M. V. Andrés, "Polarization modulation instability in all-normal dispersion microstructured optical fibers with quasi-continuous 1064 nm pump", Conference on Lasers and Electro-Optics Europe & European Quantum Electronics Conference (CLEO/Europe-EQEC 2019), 1-1, Munich, 2019.
- A. Loredo-Trejo, Y. López-Diéguez, L. Velázquez-Ibarra, A. Díez, E. Silvestre, M. V. Andrés, "Polarization Modulation Instability in Weakly Birefringent Photonic Crystal Fibers with All-Normal Dispersion", 11ª Reunión Española de Optoelectrónica (OPTOEL'19), SP1.ONL01, Zaragoza, 2019.

- A. Loredo-Trejo, A. Díez, E. Silvestre, M. V. Andrés, "Widely Tunable Polarization Modulation Instability in D 2 O-Filled Microstructured Optical Fiber wit sub-ns pumping", XII Reunión Española de Optoelectrónica (OPTOEL'21), 76, Spain, 2021.
- A. Loredo-Trejo, A. Díez, E. Silvestre, M. V. Andrés, "Simultaneous generation of four-wave mixing and polarization modulation instability in microstructured optical fibers", XIII Spanish National Meeting on Optics (RNO 2021), 1, Spain, 2021.